UNIVERSITY OF OKLAHOMA

GRADUATE COLLEGE

SEISMIC CHARACTERIZATION OF INTRA-BASEMENT DEFORMATION AND ITS INFLUENCE ON THE OVERLYING SEDIMENTARY STRATA: IMPLICATIONS FOR TECTONIC EVOLUTION AND INDUCED SEISMICITY IN NORTHERN OKLAHOMA

A THESIS

SUBMITTED TO THE GRADUATE FACULTY

in partial fulfillment of the requirements for the

Degree of

MASTER OF SCIENCE

By

Max Firkins

Norman, Oklahoma

2021

SEISMIC CHARACTERIZATION OF INTRA-BASEMENT DEFORMATION AND ITS INFLUENCE ON THE OVERLYING SEDIMENTARY STRATA: IMPLICATIONS FOR TECTONIC EVOLUTION AND INDUCED SEISMICITY IN NORTHERN OKLAHOMA

A THESIS APPROVED FOR THE

SCHOOL OF GEOSCIENCES

BY THE COMMITTEE CONSISTING OF

Dr. Brett M. Carpenter, Chair

Dr. Xiaowei Chen

Dr. Heather Bedle

Abstract

Patterns of recent seismogenic fault reactivation in the granitic basement of north-central Oklahoma necessitates an understanding of the structural characteristics of the inherited basement-rooted faults. We analyze the top-Arbuckle, top-basement, and intra-basement structures in 9 post-stack time-migrated 3D seismic reflection datasets in north-central Oklahoma using structural seismic attributes. Across all surveys, sub-horizontal intra-basement reflectors (igneous sills) are observed, which commonly terminate at the basement-sediment interface. Overall, our results reveal 146 fault traces at the top of the Precambrian basement with dominant trends along WNW-ESE, NE-SW, and N-S. Many of these faults were previously unmapped, supporting the assertion that there is a considerable cumulative seismic risk from unidentified faults. First examined are a subset of eight 3D seismic surveys in which 115 of the basement faults were interpreted. Proximal to the Nemaha Fault Zone (NFZ), faults dominantly strike N-S, are fewer (<10), have the lowest areal density, lowest areal intensity, and exhibit the most significant maximum vertical separation. However, with distance from the NFZ, faults exhibit NE-SW trends, areal fault density increases, areal fault intensity increases, and maximum vertical separation decreases. Of these 115 faults, ~49% are contained within the basement, ~28% terminate in the Arbuckle Group, and ~23% transect units above the Arbuckle Group. These observations suggest that proximal to the NFZ, deformation is accommodated along a few but longer fault segments, and with distance away from the NFZ, deformation is distributed across more relatively shorter fault segments. The existence of through-going faults suggests the potential for spatially pervasive fluid movement along faults. In the Harper Creek 3D seismic volume, a sequence of 56 relocated earthquakes is collocated with the survey. These events delineate the actual structure of an intra-basement fault zone. This provides a means of guidance and validation on attribute-assisted basement fault interpretation.

When included in the interpretation of basement faults, it shows two critical steps beyond curvature interpretation at the top basement. The first is to couple to curvature interpretation with an aberrancy attribute visualization. When included, aberrancy improves the quantity and placement of interpreted fault traces. Second, it is essential to analyze the units directly above the basement. In the sedimentary units, the faults tend to express more clear signs of too subtle structures to identify at the top of the basement. Results have direct implications for wastewater injection and seismicity in north-central Oklahoma and southern Kansas. Additionally, they provide insight into the characteristics of basement-rooted structures around the NFZ region and suggest how to characterize basement structures where seismic data are available.

ACKNOWLEDGEMENTS

I would like to thank Dr. Brett M. Carpenter, Dr. Heather Bedle, and Dr. Xiaowei Chen for agreeing to be a part of my committee and providing comments on how this thesis might be improved. I want to thank my committee chair, Dr. Brett M. Carpenter, for providing me my first research opportunity within his group, giving mentorship along the way, and shepherding me through my first publication. Another mentor and collaborator during my time at OU was Dr. Folarin Kolawole, another student in Dr. C's research group. Fola was one of the most passionate and intelligent people that I have had the opportunity to interact with in the geosciences, and I owe him a lot of thanks. To the other members of my research group, thank you for listening to and helping me improve all my presentations. Finally, I would like to thank my parents for their unending help and support throughout my higher education. This truly would not have been possible without them.

All the work that is shown in this thesis would not be possible without several gracious data contributions. I would first like to thank the Osage Nation of Oklahoma and Spyglass Energy LLC for providing the eight seismic surveys, which are shown in the second chapter of this thesis. I also appreciate their allowing the data and associated work performed to be published. Thanks to Chesapeake Energy for their providing the Harper Creek 3D seismic data.

TABLE OF CONTENTS

LIST OF FIGURES

LIST OF TABLES

CHAPTER 1 - INTRODUCTION

Intra-plate regions are often tectonically quiescent or at the very least unlikely to host frequent, substantial seismic events. The reason for this is a combination of rock's elasticity and the significant distance from active plate boundaries—however, there are regions within plates that may host tectonically driven seismic events. Oklahoma is near the center of the North American Craton (Figure 1a). The stresses present, though considered far-field, are sufficient to produce earthquakes. Documentation of these events suggests approximately 21 events per year over magnitude three from 1967 to 2001 (Ellsworth, 2013). Beginning in 2009, the frequency of seismic events in Oklahoma and southern Kansas grew dramatically. This marked increase has brought with it considerable potential hazards to the infrastructure and populations within the midcontinent. Prior to this period, the most recent event of significant hazard was a magnitude 5.5 earthquake near El Reno, Oklahoma, in 1952. After this, few events of significance were recorded until the increase in 2009. From this point, large events were a relatively common occurrence, with 8 of the ten most significant events in the state occurring from 2011 to 2016, all above magnitude 4.5 with significant associated ground motion (OGS, 2020). As the rates of seismicity and hazard grew, so did the interest in studying these events, both to ascertain the causes of the rampant increase in seismicity and mitigate the rising seismic hazard within the midcontinent. The primary focus of most studies regarding the increase of seismicity within the midcontinent was that of the cause, more specifically, whether the increase could be considered anthropogenic or induced. Conclusions from works focused on the region show that the prolific seismic activity has been induced by human activity, the primary cause being the injection of drilling associated fluids (wastewater) into the Arbuckle Group (e.g., Kroll et al., 2017; Yeck et al., 2017; Kolawole et al., 2019). While this connection has answered the primary question of why seismicity has exploded

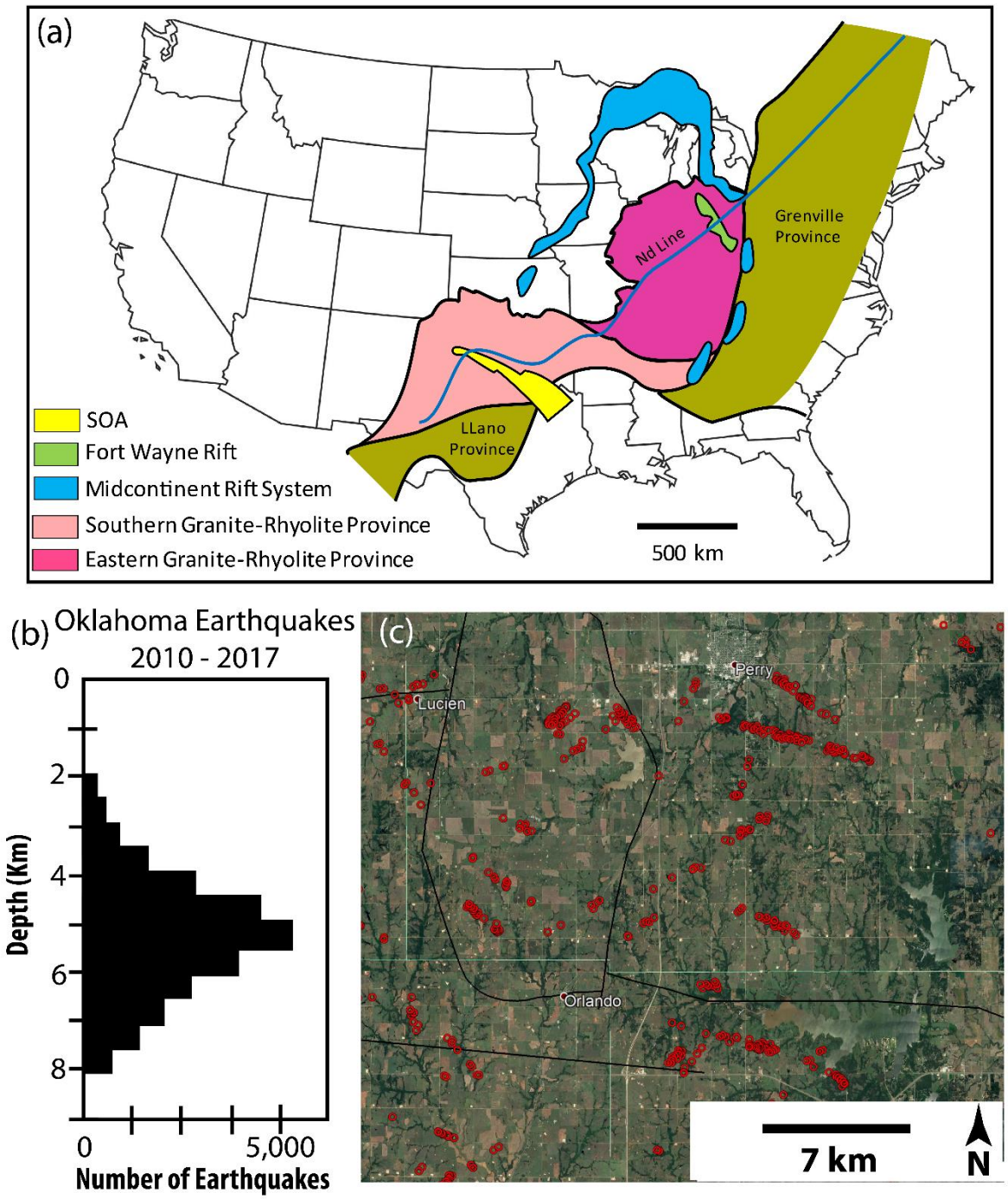

Figure 1: Spatial patterns and depth distribution of seismicity (a) Map showing the extents of the Southern and Eastern Granite-Rhyolite Provinces, location of the Midcontinent Rift System, and the position of the Southern Oklahoma Aulacogen (Modified after Bickford et al. 1981). (b) Histogram of depth (relative to MSL) vs. Number of Earthquakes in Oklahoma from 2010 through 2017 (Modified after Kolawole et al., 2019). (c) Satellite image of a region in north-central Oklahoma with relocated earthquakes from 2010 – 2017 as red circles (Chen, 2016) and faults as black lines (Marsh and Holland, 2016).

within Oklahoma and Kansas and led to thus far effective mitigation efforts, there remain pertinent

questions to be answered.

While there has been considerable effort dedicated to understanding the mechanisms causing the elevated seismicity with the region (e.g., Chang et al., 2016; Zhai et al., 2019; Keranen et al., 2014; Ellsworth et al., 2015), less has been devoted to understanding the terrain hosting the events. Seismic events within Oklahoma occur predominantly from 4 to 7 km below mean sea level. Depth to the top of the basement in the primary regions of seismicity (Anadarko Shelf and Cherokee Platform) are between 2 and 7 km. Therefore, the basement is the primary host of most events that have been recorded over the past decade (Figure 1b). It is crucial that the structural history and character of the crystalline basement are well understood. The increase in seismicity has revealed the relative lack of understanding of the basement. The observation illustrates that a significant number of seismic sequences align to highlight fault traces that have not been previously identified (Figure 1c). The problem that limits this characterization's ability to take place is the near-complete burial of the basement within the midcontinent. Within Oklahoma, there are only two known and explored basement outcrops, which are both of limited spatial extent. Thus, remote sensing methods must be employed to characterize the basement domain of the midcontinent further. In the following chapters, nine 3D seismic surveys will be interpreted, focusing on the basement, the structures therein, and their influence on the deep sediments into which wastewater has historically been injected.

GEOLOGIC SETTING

THE PRECAMBRIAN IGNEOUS BASEMENT OF NORTH-CENTRAL OKLAHOMA

In the area of interest for this study, the granite has been shown to vary compositionally and texturally. Based on prior works, there are two main domains that comprise most of the land

in Oklahoma and large portions of the central United States (e.g., Bickford et al., 1981; Anderson, 1983; Thomas et al., 1984; Lidak, 1996). These are the Southern and Eastern Granite-Rhyolite Provinces. The Southern Province trends northeast-southwest and extends from north-central Mexico into southern Missouri and Tennessee. The Eastern Province trends north-south from southern Missouri into central Michigan and Ohio (Figure 1a).

The provinces formed in the Mesoproterozoic Era of the Precambrian Eon, from 1.50 to 1.34 Ga (Bickford et al., 2015). They intruded the preexisting Yavapai and Mazatzal accretionary terranes of the North American Continent (Van Schmus et al., 1993). The exact origin of the provinces is still under debate. Some argue that there was a continental margin present during formation (e.g., Bickford et al., 1981; Thomas et al., 1984). Contrarily, others suggest no margin present with a pure extensional setting as the plutons' impetus (e.g., Anderson, 1983; Sears et al., 2005). In recent years, another possibility was proposed. This possibility is a long-lived (~1.5 Ga) subduction zone along the Laurentian Margin, which was responsible for many of the basement domains of North America (e.g., Rivers and Corrigan, 2000). Regardless, there appears to be a consensus that, in general, the development of the provinces is related to large-scale continental extension/rifting (Slagstad et al., 2009).

In terms of age, the rocks have generally been shown to grow increasingly younger, moving to the west. The two groups have been divided by age, with 1.40 Ga set as the dividing time (Van Schmus et al., 1993). The observation is that, in general, the rocks of the Eastern province are dominated by older (1.50 – 1.40 Ga) rocks. In contrast, rhyolites and granites of the Southern province fall within both periods (Van Schmus et al.,1993). Compositionally, the broader mass of rock is an A-type rapakivi textured granite (Emslie, 1980). This textural classification of the igneous bodies is generally associated with anorogenic settings sourced from a depleted mantle.

Additionally, it has been shown that the plutonic event had bimodal nature with mafic material emplaced along with the felsic bodies (Frost et al., 1999; Lidak, 1996).

The SGRP is composed of smaller igneous domains within Oklahoma (Denison, 1966; Denison, 1981). In the area studied, three domains comprise the basement. These are the Washington Volcanic Group, Central Oklahoma Group, and the Osage Microgranite. The Washington volcanic group underlies the northwestern portion of Osage County and the eastern half of Kay County. It is comprised of predominantly felsic pyroclastic flows and tuffs (Denison 1981). The Central Oklahoma Group lies beneath the majority of Osage county and many of the counties in central Oklahoma. It is a large, circular plutonic body that intruded the crust (Denison, 1981). Finally, the Osage Microgranite lies in Osage County's south-central portion (entirely within the Central Oklahoma Group). The origin of the Osage Microgranite is not well understood. However, it is distinct in texture and composition from the other units. It is more porphyritic and contains less silica than the other granite bodies (Denison, 1981).

Tectonic History of the Region and Present-Day Basement Structure

There is relatively little known about the overall structural history of the crystalline basement of Oklahoma (and the entire SGRP/EGRP). It has been shown that the basement surface is highly undulating. This undulation is interpreted as eroded Precambrian structures, which suggests high degrees of Precambrian deformation (Ireland, 1955). A recent study showed that the basement in northern Oklahoma is heavily fractured and altered even at significant depths from the basement-sediment interface. There is also evidence of multiple active stages of deformation and fluid-rock interactions. This suggests the basement is damaged to a much higher degree than thought in the past (Hamilton et al., 2021)

Within the area of interest, there are a few major Precambrian structures that have been identified. These are the Midcontinent Rift (Stein et al.,2014), Nemaha Fault Zone, Labette fault, and Osage Dome (Denison, 1981). The largest of these are the Midcontinent Rift and the Nemaha Fault Zone. The Midcontinent Rift will be discussed in the following section. The Nemaha Fault zone is a prominent feature in the mid-continent of the United States. The structure stretches for approximately 650 km and generally strikes northeast-southwest. The fault zone cuts through Nebraska, Kansas, and Oklahoma (McBee 2003). Its origin is still debated as there is significant evidence of normal, strike-slip, and reverse faulting. There are multiple hypotheses as to the fault zone's origins. One hypothesis is the NFZ being the result of pure wrench faulting (McBee, 2003), and another is the NFZ forming due to thrust faulting via subsequent compressional events (Gay, 2003).

The phanerozoic structure of Oklahoma's basement is dominated by three major tectonic events, one extensional and two orogenic events, all in the south. Temporally, the Southern Oklahoma Aulacogen (SOA) formed first in the Middle to Late Cambrian during the breakup of Rodinia (Moores, 1991) and the formation of the proto-Atlantic (Burke and Dewey, 1973). The feature trends northwest-southeast extending from northeastern Texas across southern Oklahoma and into north Texas. It then segments (rift jumps) and continues across northeastern New Mexico and into the border of central Colorado and Utah (Keller and Stephenson 2007). Following the failure of the rift arm, the rift continued to subside, creating accommodation for sediment deposition thermally (Perry, 1989). In late Mississippian time, the collision of Laurentia and Gondwana began (Hatcher, 2010). The collision of these continents is termed the Alleghenian Orogeny, which created the Appalachian, Ouachita, and Marathon fold-thrust belts, which cut across much of the United States. This orogenic event was long-lived and caused the reactivation

of numerous structures. The most prominent of which are those of the SOA. These faults uplifted the Wichita and Amarillo regions and created the Anadarko Basin. During this same period, the Ouachita fold-thrust belt was forming, and the Arkoma basin was developing. It is considered a foreland basin caused by continental collision (Elmore et al., 1990).

A general structure for the basement has been mapped (Crain and Chang, 2018). West of the Nemaha, the basement dips southward (towards the Wichita Uplift). Between the Nemaha fault zone and the Seminole Arch, the basement dips to the southwest (deepening into the Anadarko basin). In the easternmost portion of the state (east of the Seminole Arch), the top of the basement dips to the southeast (into the Arkoma Basin). Basement depths vary drastically within the state from a few hundred meters below sea level in the northeast and southcentral areas to 10 km below sea level in the Anadarko and Arkoma basins. In the area of interest for this study, the basement dips to the west. Depth values are 610 meters below sea level in the eastern portion of Osage county. In the southwestern corner of Kay County (near the NFZ), depth values dive to more than 1525 meters below sea level (Crain and Chang, 2018).

Basement involved Phanerozoic deformation in Oklahoma is attributed to three major tectonic events: one extensional and two orogenic, all in the south (Figure 2c). Temporally, the Southern Oklahoma Aulacogen (SOA) formed earliest during the Middle to Late Cambrian breakup of Rodinia (Moores, 1991) and the formation of the proto-Atlantic Ocean (Burke and Dewey, 1973). The SOA trends WNW- ESE and extends aerially across northeastern Texas, southern Oklahoma, and into the north Texas Panhandle (Figure 2a). It then segments and continues across northeastern New Mexico and into the border of central Colorado and Utah (Keller and Stephenson, 2007). Thermal subsidence followed the failure of the SOA rift arm, creating accommodation for early phanerozoic sediment deposition (Perry, 1989).

In late Mississippian time, the collision of Laurentia and Gondwana began (Hatcher, 2010). The collision of these continents, known as the Alleghenian Orogeny, created the Appalachian, Ouachita, and Marathon fold-thrust belts affecting much of the eastern and southeastern United States. This orogenic event was long-lived and is responsible for the reactivation of numerous structures, including portions of the SOA (e.g., Kluth, 1986). This reactivation occurred along rift-initiated faults, uplifting the Wichita and Amarillo regions and creating the Anadarko Basin (Keller and Stephenson, 2007). During this same period, the Ouachita fold-thrust belt and the Arkoma foreland basin developed through continental collision (e.g., Elmore et al., 1990).

SEDIMENTARY COVER

In the area of interest of north-central Oklahoma, the crystalline basement is covered by a relatively thick layer of sedimentary units (Figure 2c). Our study focuses only on the lowermost section of the stratigraphy, primarily the Arbuckle Group. The Arbuckle Group is a sequence of predominantly limestone and dolomite, with minor shale and sandstone members (e.g., Johnson, 2008). This sedimentary succession is observed to be directly deposited on the unconformable basement surface. However, in some areas, the Arbuckle Group is separated from the basement by the Cambrian-age Reagan Formation, which was deposited in local depo-centers (Elebiju et al., 2011). The Reagan Formation is either absent in the main study area (north-central Oklahoma) or very thin (Carroll et al., 1999).

CHAPTER 2 - ATTRIBUTE-ASSISTED CHARACTERIZATION OF BASEMENT FAULTING AND THE ASSOCIATED SEDIMENTARY SEQUENCE DEFORMATION IN NORTH-CENTRAL OKLAHOMA

The material within this chapter has been published in a peer-reviewed journal. A full reference can be found in the References Cited section under Firkins et al., 2020.

INTRODUCTION

The US mid-continent region has experienced an increase in seismicity, starting in 2009 and spiking in 2016, with many of these events concentrated in Oklahoma (Figure 2a) (e.g., Jacobs, 2016). The bulk of these earthquakes has occurred in the crystalline basement on previously unmapped faults (e.g., Kolawole et al., 2019). Across this region, the Precambrian basement is mostly buried; thus, the detailed structure and characteristics of the basement, which make it susceptible to seismogenic reactivation, remain poorly understood. Fracture systems mapped in the field on limited basement exposures in southern Oklahoma have been correlated with trends of observed seismicity across the region (Kolawole et al., 2019; Qin et al., 2019). However, there remains the need to characterize basement structures in the north-central Oklahoma region where seismicity is most frequent. Presently, the Ordovician-age carbonate Arbuckle Group is of interest in Oklahoma, as it represents the disposal unit for the increased volumes of produced wastewater from hydrocarbon exploration activities (e.g., Kroll et al., 2017; Yeck et al., 2017; Kolawole et al., 2019). Injection into this unit has been linked to the increased levels of seismicity within the state. It is assumed that the pervasive presence of faults, which connect the basement and sedimentary cover, would increase the likelihood of fluid movement between the layers into which fluid is being injected and the basement (e.g., Mohammadi et al., 2017). To date, the relative proportions of the basement-rooting faults that cut into and through the Arbuckle unit and shallower units are

not known. While the cause of the recent seismicity is likely related to a combination of poroelastic loading and pore-pressure diffusion (e.g., Chang and Segall, 2016; Zhai et al., 2019), it is envisioned that the transmission of produced water into the basement is likely to alter the mineralogy and potentially, the stress state in the crystalline basement (e.g., Qin et al., 2019). This could lead to delayed and long-lived seismicity within the region (Pollyea et al., 2019).

In this study, we analyze seismic data from two counties in north-central Oklahoma (Figure 2a-b) to identify structures that are present within the crystalline basement, the characteristics of their propagation into the sedimentary cover, and their relationship with patterns of seismicity in the region. Our analyses show the salient, first-order structural characteristics of the intra-basement and basement-rooted structures in north-central Oklahoma and elucidate the implications for fluid injection-related seismicity in the region.

DATA AND METHODS

3D SEISMIC REFLECTION DATA

To assess the structure of the deep basement, we utilized eight 3D seismic reflection survey datasets. These surveys are in Osage and Kay counties, covering an area of ~700 $km^{2,}$ and are sampled at 2 ms and post-stack time migrated (Figure 2b, courtesy of Osage Nation and Spyglass LLC). The data was supplied in its interpreted and presented form as single stacks (incidence angle ranges unknown). The data were acquired and processed with the goal of imaging the sedimentary cover for hydrocarbon exploration. Therefore, imaging in the basement is relatively poor (average of 23 m in the sedimentary cover vs. 30 m in the basement, see Appendix A for details).

For brevity, of the eight surveys, we show maps and cross-sections from three representative volumes (interpretation of all eight surveys is provided in Appendix A), which

include the Bois d'Arc, Wild Creek, and Big Heart surveys (Figure 2b). The three volumes are spatially distributed eastward from the Nemaha Uplift and Fault Zone (NFZ), a structure that is of interest to our findings in this study. The Bois d'Arc survey is right at the western edge of the NFZ, the Wild Creek survey is approximately 40 km east, and the Big Heart survey is approximately 80 km east of the NFZ (Figure 2b). In the absence of well data, we constrain the identification of the top-basement and top-Arbuckle reflectors via a previous study that analyzed three of the same seismic volumes and tied the seismic volumes to well data (Elebiju et al., 2011). As the goal was to study the structure near the top-basement and intra-basement, we chose the z-crossing of the basement and top of the Arbuckle Group (Figure 3 g-i). A z-crossing is the point at which the instantaneous seismic amplitude has a value of zero when transitioning from a peak (local maximum) to a trough (local minimum).

For enhancement of the desired features on the top of the basement, three seismic attributes were selected. These attributes are principal positive curvature, principal negative curvature, and energy ratio similarity. The intra-basement reflectors had only energy ratio similarity applied. All the attributes utilized were first computed volumetrically. Then the instantaneous values were extracted onto the interpreted horizon.

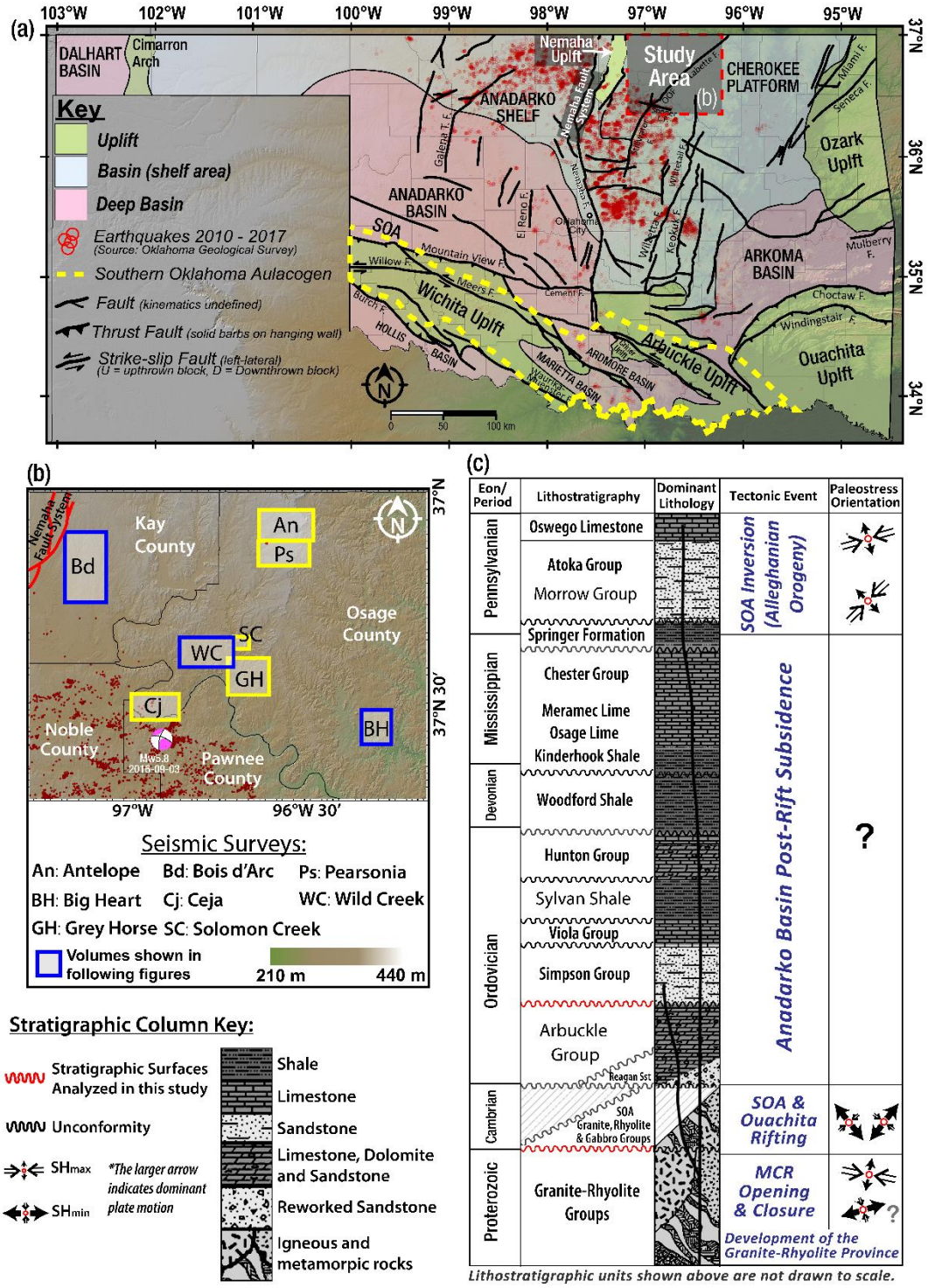

Figure 2: The geologic and neoseismic setting of the study area. (a) Tectonic map of Oklahoma showing the geologic provinces (modified after Northcutt and Campbell, 1995; Kolawole et al., 2020). Red dashed square = location of the study area. (b) DEM hillshade map of the study area in north-central Oklahoma, showing the location of the eight 3D seismic reflection surveys used in this study. (c) Simplified stratigraphic column of the Anadarko Basin (after Kolawole et al., 2020). The stratigraphic tops in red represent the surfaces of interest in this study.

Energy ratio similarity is a type of coherence attribute which highlights reflector discontinuity between seismic traces. This attribute has become widely used to identify and map geologic discontinuities of various types (Bahorich and Farmer, 1995). In this work, we select it for its ability to illuminate reflector offset created by fault displacement. In general, the method is based on variations in inline, crossline, and seismic amplitude within a grid of traces (Bahorich and Farmer, 1995). Specifically, energy ratio similarity represents the ratio of the coherent and total energy within a given analysis window, where the total energy is the sum of energy of each trace used to create the covariance matrix, and the coherent energy is the sum of the energy of the principal component-filtered trace (Chopra and Marfurt, 2007). We computed the energy ratio similarity attribute using the AASPI software package. The algorithm uses a seismic amplitude volume and derived inline and crossline dip volumes. We choose to use a fixed rectangular analysis window with a window half-height of 10 ms. The spatial size of this window varies across the different data sets according to the inline and crossline spacing for a given survey (values are between 16.5 and 33.5 m for all volumes).

The two principal curvature attributes were computed to accentuate structures in the data, as the purpose of this study was to analyze large-scale features in the basement of Oklahoma. This was done via AASPI using its dip-guided volumetric curvature algorithm. The inputs which go into this computation are an inline and crossline dip volume. From this, the software computes optimized default parameters for the given volume (provided in Appendix A). We chose a long wavelength (which preferentially accentuates larger features) for the calculation of curvature. In this computation, a filter is generated by defining points in terms of four wavenumbers $\lambda 1$, $\lambda 2$, $\lambda 3$, and $\lambda 4$. These wavenumbers are then weighted as 1, 0.666, 0.333, and 0, respectively ($\lambda 4$ for all eight volumes lie between 186 and 311 meters). The implementation of both curvatures is meant

to highlight any curve which occurs in the seismic data between traces, the expression of which can represent a multitude of geologic features. Positive curvature highlights areas that have convex upward structures (i.e., fault tip flexures, channel edges). Negative curvature reveals locations of convex downward features (i.e., channels, karsts) (Mai et al., 2014).

Following the interpretation, generation, and attribute extraction of key seismic surfaces, faults were interpreted. This interpretation was completed by observing lineaments of positive curvature, negative curvature, and/or energy ratio similarity on generated horizon surfaces. Ideally, the fault character would be a low similarity lineament flanked on one side by a positive curvature lineament and the other by a negative curvature lineament. This signature would represent the fault's offset of traces (low similarity), the upthrown block (positive curvature), and the downthrown block (negative curvature) (Mai et al., 2014). However, it is possible for faults to be expressed by only one of these features. So, these signatures were identified in map view and verified in profile view. Arbitrary seismic profiles were created for each fault analyzed. The trend of the arbitrary section was set to be generally perpendicular to that of the fault. In the cases where faults possess considerable deviation in trace strike, multiple profile orientations were generated. While the imaging was relatively poor in the basement, we attempted to observe consistent offset of small reflector packages in the basement or linear/planar zones of consistent disruption. In many cases, the geometry of faults within the basement could not be fully and confidently outlined. However, the expression of the attributes at the top-basement strongly suggests the presence of a fault (Figure 3).

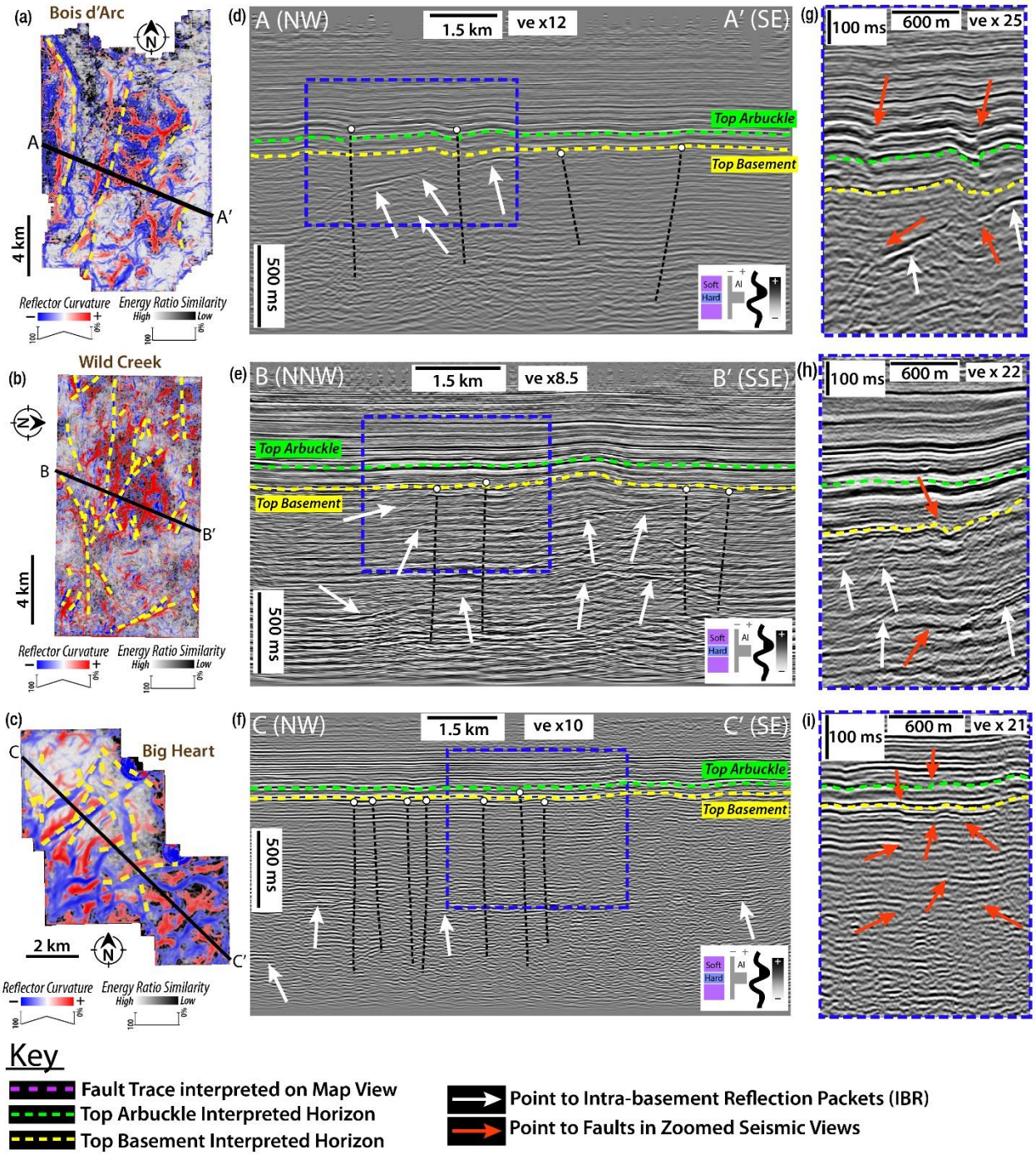

Figure 3: The intra-basement and through-going structures in the study area. For each survey, we show: (a - c) co-rendered energy ratio similarity and curvature (most-positive and most-negative) attributes extracted onto the top-basement surface, and (d – f) 2D seismic cross-section (vertical slice) overlaid with reflector and structural interpretations. White circles on the fault traces represent the shallowest visible tip of the interpreted fault. (g – i) Zoomed views of the seismic cross-sections displayed in panels d – f. The extent of these views is shown in panels d – f outlined by the blue dashed lines. On these zoomed views, some of the faults which are interpreted on panels d – f is shown without the interpreted vertical trace. The red arrows point to the disruption which was used to validate the presence of the faults.

After fault presence was established for all attribute enhanced lineaments, their degree of upward continuation was examined. For this analysis, the goal was to determine the vertical extent of each fault segment. To accomplish this, the identified fault traces at the top of the basement were displayed in 3D space using the arbitrary cross-sections again. Each arbitrary cross-section was displayed and brought to one end of the fault. The cross-section was then scrolled along the length of the fault. At each step, the cross-section was examined, focusing first on the top-basement reflector to find the location of the previously identified basement penetrating fault. Then, the seismic units above the basement fault location were examined, looking for the continuation of the

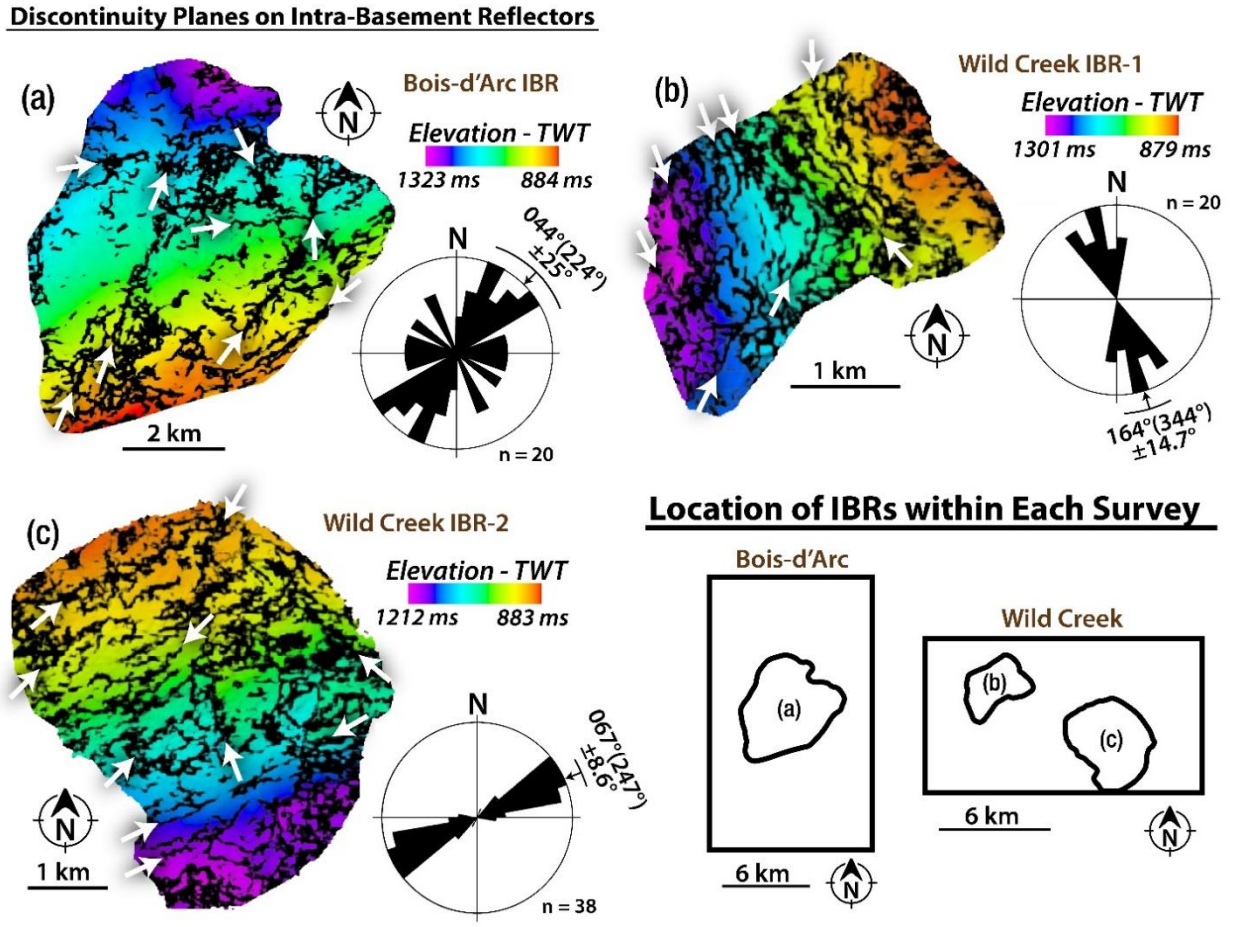

Figure 4: Trends of potential fault traces at depth in the basement. Co-rendered time-depth and energy ratio similarity attributes on surface maps of the largest intra-basement reflectors (IBR) mapped in the (a) Bois d'Arc and (b - c) Wild Creek surveys. The white arrows point at lineaments of low energy ratio similarity (i.e., discontinuity lineaments). Rose diagrams show the frequency-azimuth distribution of the lineaments. The location of the intra-basement surfaces within their given survey are shown in the diagram in the lower right.

fault up section (reflector offset). This was completed first within the Arbuckle Group interval and then above the Arbuckle Group interval. This data was then recorded as two groups: the faults that showed displacement of seismic reflectors at the top-basement horizon and within the Arbuckle Group and the faults that showed displacement above the top of the Arbuckle Group reflector. In effect, this analysis created three discrete groups of faults: (1) faults that show displacement only within the basement, (2) faults that have displacement in the basement and into the Arbuckle Group, and (3) faults that cut through the basement, through the Arbuckle Group, and into the sedimentary lithologies above the Arbuckle Group.

Quantitative Fault Analysis

To assess the spatial variability of the analyzed faults, two calculations were performed using the collected fault trends and lengths. The first is the fault areal density. Fault areal density was calculated by dividing the number of faults in each 3D volume by the area of that survey. This results in a single value for each survey in the units of km^{-2}. The second calculation performed with the collected fault data was to determine fault areal intensity. This was performed by first summing the length of all faults within a given survey. The value was then divided by the area of the survey, resulting in a single value per survey in the units of km^{-1}.

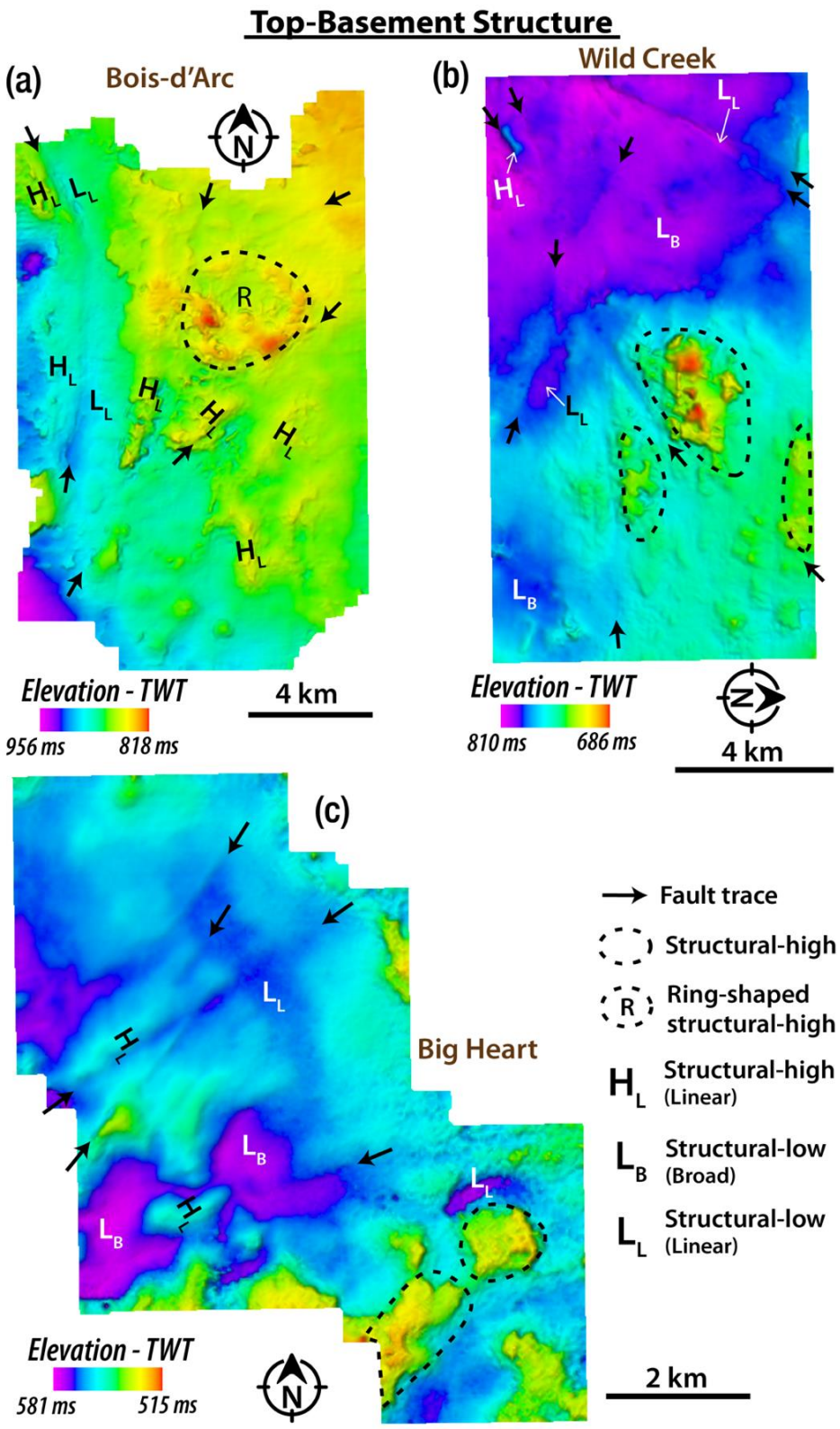

Figure 5: Representative top-basement structure. (a) Bois d'Arc (b) Wild Creek (c) Big Heart. The surfaces show examples of the common top-basement structural features observed in all the surveys.

Finally, the vertical separation for all faults was measured. Vertical separation is a measure of across fault offset. It is akin to vertical throw, though not as strictly defined. The measurement of vertical separation was done using the previously described fault-perpendicular arbitrary cross-sections. Each cross-section was displayed at one end of the fault trace, and the fault's position at the top of the basement was located. The section was then sequentially scrolled at spatial steps of approximately 330 m. The offset was measured at the top of the basement. This was compared to the up-thrown and down-thrown elevations of the deformed basement surface. As the data is in the time domain, these values were recorded in TWT milliseconds, meaning the offset values would be velocity-dependent.

RESULTS

BASEMENT DEFORMATION: INTRA-BASEMENT REFLECTION PACKETS (IBR)

Present in the basement is distinct packets of coherent, laterally continuous, relatively higher amplitude reflectors (intra-basement reflectors, IBR; Figure 3d-i), which commonly show shallow dipping geometries, cross-cutting relationships, and often bifurcate into multiple segments. Although we observe these features in all the eight seismic surveys, they vary in aerial extent and magnitude of segmentation. The mapped IBRs show varying dip directions, which include north (e.g., Figure 4a), west (e.g., Figure 4b), and south (e.g., Figure 4c). The lineaments of low energy ratio similarity attribute along the mapped IBR surfaces delineate discontinuity planes that exhibit mean trends along NE-SW to ENE-WSW (e.g., Figure 4a and 3c) and NNW-SSE (e.g., Figure 4b).

TOP-BASEMENT STRUCTURE

The basement is seismically identified using two main criteria. First, the crystalline basement has a distinctive seismic character from the sedimentary cover. It presents a low amplitude, discontinuous, chaotic, highly variable reflectivity (Figure 3d-f), which is likely controlled by the lack of bedding and comparatively high homogeneity in igneous rocks (few high impedance contrasts). Second, the top-basement reflector itself is characterized by a relatively high negative amplitude and is generally continuous throughout the seismic volume (Figure 3). By contrast, the intra-basement reflectors in the seismic volumes are typically discontinuous, high-amplitude, and typically a strong trough-peak or trough-peak-trough reflector packet (Figure 3). Like the Top-Basement reflector, the most continuous of the intra-basement reflectors were selected. These reflectors were then picked to their most complete spatial extents.

As mentioned previously, three representative volumes have been selected for display in this study; the Bois d'Arc, Wild Creek, and Big Heart (Figure 2b; Figure 3; Figure 5). When examining the picked surfaces in two-way travel time (Figure 5), structures begin to emerge. Figure 5a shows a surface that dips to the southwest and has a scattering of localized highs near the center of the survey. Figure 5b shows a surface that dips to the southwest and shows a few lineaments that generally trend NE-SW. Similarly, the surface in Figure 5c shows a surface that dips toward the southwest and shows lineaments trending NE-SW. All dips observed generally agree with the regional dips put forth by Crain and Chang (2018) (see Appendix A).

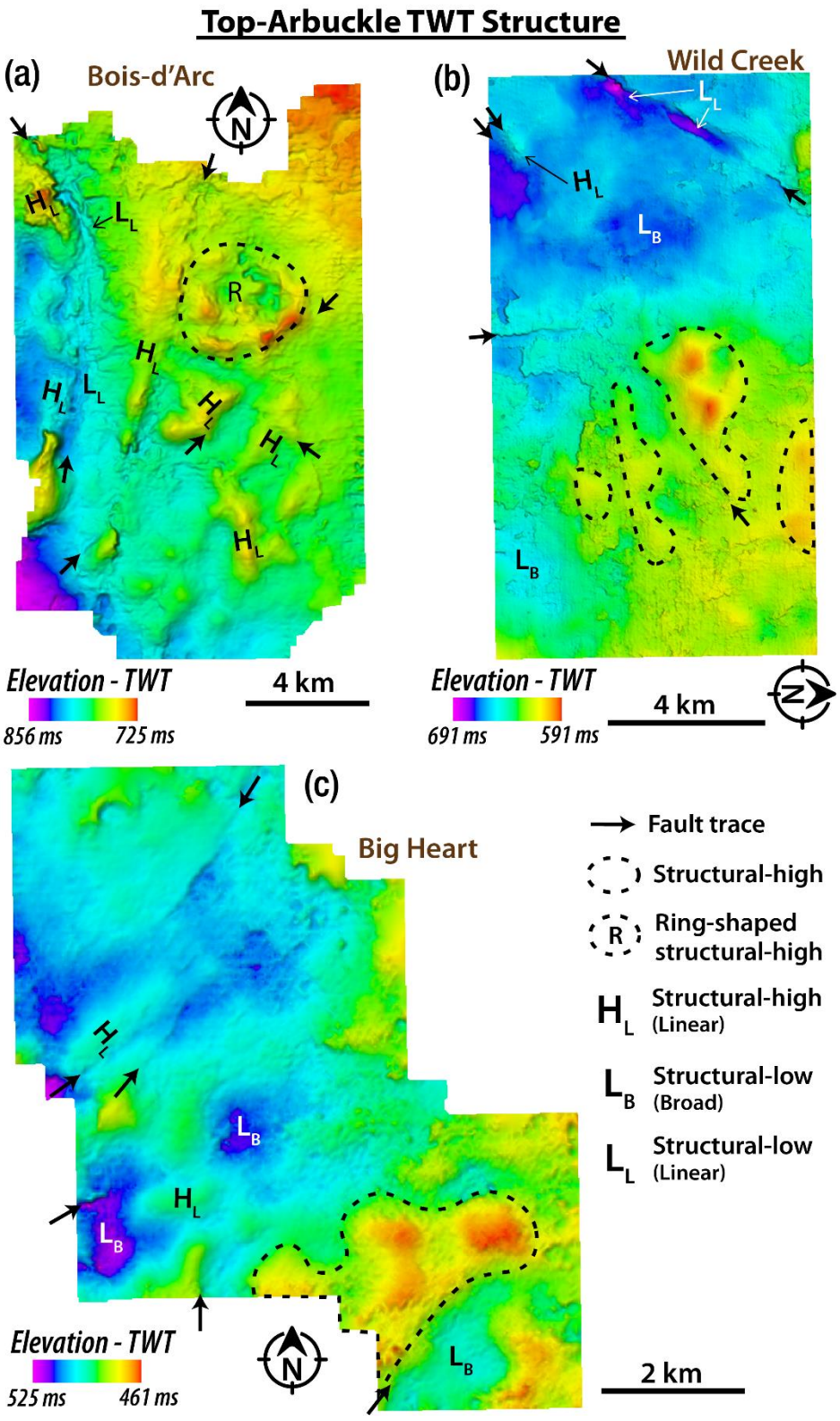

Figure 6: Representative top-Arbuckle structure. (a) Bois d'Arc (b) Wild Creek (c) Big Heart. The surfaces show examples of the common top-basement structural features observed in all the surveys.

There are six key features that can be observed on each TWT basement surface. These features include visible fault traces, structural-highs, ring-shaped structural-highs, linear structural-highs, linear structural-lows, and broad structural-lows (Figure 5). The Bois d'Arc surface is dominated by a large (4 km diameter) ring-shaped structural high (66 ms or ~200 m) surrounded by multiple linear structural highs. Near the western edge of the survey, there is a broad structural low to the west with multiple closely spaced structural highs in the east, and numerous linear highs and linear lows are interspersed (Figure 5b). The top-basement surface from the Big Heart survey reveals comparable structures, with two closely spaced structural highs in the SE corner and two similarly spaced broad structural lows just to the NW. Also present are numerous visible fault traces which trend NE-SW predominantly (Figure 5c).

When attributes are extracted, the orientation of the lineaments at the top of the basement becomes clearer. In general, most lineaments correspond to high values of negative curvature (Figure 3a-c). In many cases, these trends are accompanied by a corresponding positive curvature lineament, and for even fewer, a low energy ratio similarity zone can be observed between the two (Figure 3). Also seen at the top of the basement are large regions of high positive curvature (Figure 3a-c). These are typically circular and elliptical in shape (in map view) and are commonly bounded by low curvature regions (Figure 3a-c). Looking at the interpreted top-basement horizons with extracted attributes from the three representative volumes, there is a change in the dominant trend of the lineaments (Figure 3a-c). These trends rotate from approximately N-S in the west (Figure 3a) to progressively NE-SW and WNW-ESE in the east (Figure 3b; Figure 3c). In seismic cross-section, the interpreted basement faults appear as discontinuities of the top-basement reflector packet or areas of dimmed or disrupted amplitude that cut down into the basement. Disruption in the basement is often poorly imaged and characterized by consistent low amplitude zones.

However, many faults can be seen intersecting intra-basement reflectors. Typically, the observed faults dip vertically to sub-vertically in TWT.

Top-Arbuckle Structure

The Arbuckle Group's seismic expression is defined by a high amplitude peak-trough packet, which is generally continuous. Internally reflectors are generally low amplitude, parallel, and discontinuous. Similar features to those observed at the top-basement surface are seen on the top-Arbuckle TWT surface. In the Bois d'Arc surface, there is a large ring-shaped structural high in the north-central region. Surrounding this are numerous linear structural-high and fault traces. In the western part of the survey, there is a pair of directly adjacent linear-low and linear-high (Figure 6a). In the Wild Creek survey, there are four large structural highs in the east and a broad structural high in the west. Also observed in the west are a linear structural-low and linear structural-high (Figure 6b). The top-Arbuckle surface for the Big Heart survey reveals a large structural high in the SW corner, which is flanked by a broad structural low to the south. Near the east-central region, there is a cluster of features. There are multiple visible fault traces which separate a linear structural-high and linear structural-low. Also observed in this area are two broad structural lows.

Spatial Distribution of Vertical Separation (Vsep)

The maximum vertical separation point was determined from the compiled data for each of the 115 faults in the study. This data was grouped by survey, and the largest maximum vertical separation observed at the top-basement horizon in the volume was selected. This was then plotted in terms of maximum vertical separation versus eastward distance from the western edge of the Bois d'Arc survey (Figure 7d). Values of vertical separation range between 20 and 50 ms or 60

and 150 m (given a constant basement velocity of 6000 m/s; Kibikas et al., 2020). When plotted spatially, the maximum vertical separation for each survey shows a negative correlation with eastward distance (Figure 7d). In other words, the largest vertical offset is found in the westernmost survey, the Bois d'Arc (Figure 7), and tends to decrease eastward. There is a slight discrepancy with the values for the easternmost surveys. The faults found in the Grey Horse survey possess slightly lower values than expected by the line of best fit. While the Antelope and Pearsonia vertical offset values are higher than would be predicted. However, these still follow the trend as their quantities are predominantly less than the separation values found in the surveys to the west (Figure 7c).

Proportions of Propagated Basement Deformation into the Post-Arbuckle Sequences

To assess the structural connectivity of the basement and sedimentary cover via through-going faults, the basement-rooted structures were examined to assess their level of upward continuation. Several of the 115 identified faults are observed to be directly cutting the sedimentary cover, with additional evidence of basement highs and fault-related deformation having deformed the overlying sedimentary strata (Figure 3). Specifically, 32 basement-rooting faults clearly cut into the Arbuckle Group directly overlying the basement. Of these 32, there are 26 faults that extend above the Arbuckle Group. Therefore, ~28% of the faults identified terminate within the Arbuckle, and ~23% continue upward into post-Arbuckle sedimentary units. Spatially, the proportion of faults that cut into the sedimentary cover decrease eastward with distance (Figure 7d). The number of faults which terminate in the post-Arbuckle units is highest in the west and smaller in the east. Near the center of the data region, there are no faults that are observed which extend above the Arbuckle Group (Figure 7d).

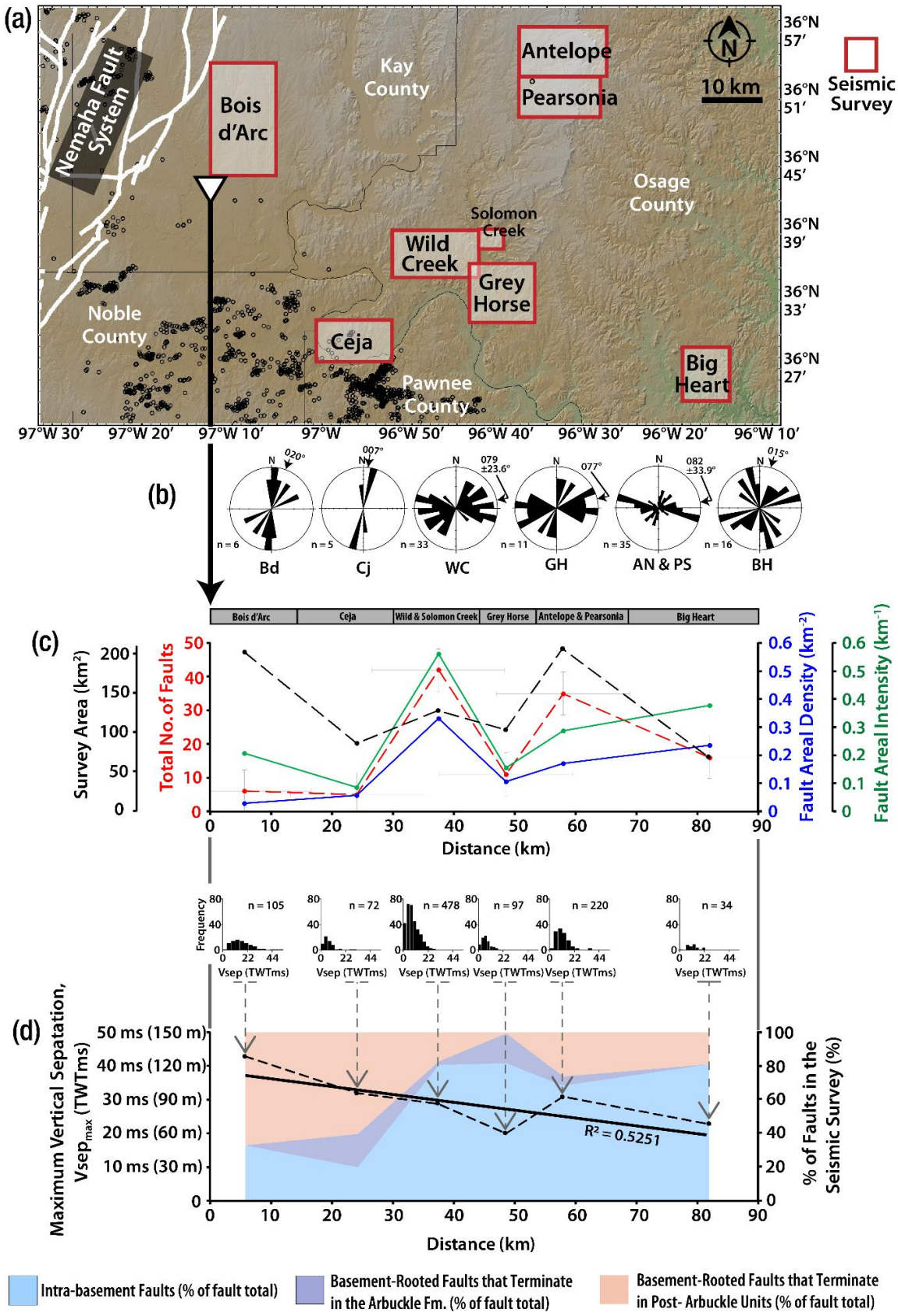
(a)
Nemaha Fault System
Bois d'Arc
Kay County
Antelope
Pearsonia
N
10 km
Seismic Survey
Osage County
Solomon Creek
Wild Creek
Grey Horse
Noble County
Ceja
Pawnee County
Big Heart
36°N 57′
36°N 51′
36°N 45′
36°N 39′
36°N 33′
36°N 27′
97°W 30′
97°W 20′
97°W 10′
97°W
96°W 50′
96°W 40′
96°W 30′
96°W 20′
96°W 10′
(b)
020°
007°
079 ±23.6°
077°
082 ±33.9°
015°
n = 6
n = 5
n = 33
n = 11
n = 35
n = 16
Bd
Cj
WC
GH
AN & PS
BH
Bois d'Arc
Ceja
Wild & Solomon Creek
Grey Horse
Antelope & Pearsonia
Big Heart
(c)
Survey Area (km²)
Total No. of Faults
Fault Areal Density (km⁻²)
Fault Areal Intensity (km⁻¹)
Distance (km)
Frequency
n = 105
n = 72
n = 478
n = 97
n = 220
n = 34
Vsep (TWTms)
(d)
Maximum Vertical Separation, Vsep$_{max}$ (TWTms)
50 ms (150 m)
40 ms (120 m)
30 ms (90 m)
20 ms (60 m)
10 ms (30 m)
R² = 0.5251
% of Faults in the Seismic Survey (%)
Distance (km)
Intra-basement Faults (% of fault total)
Basement-Rooted Faults that Terminate in the Arbuckle Fm. (% of fault total)
Basement-Rooted Faults that Terminate in Post- Arbuckle Units (% of fault total)

Figure 7: Spatial distribution of deformation intensity with respect to the location of the Nemaha Fault Zone. (a) Map of the study area showing the locations of the seismic surveys used in this study. Black circles = 2010-2017 earthquakes (source: Oklahoma Geological Survey Catalog). (b) Rose diagrams showing the frequency-azimuth distribution of the mapped faults in each survey (AN = Antelope, Bd = Bois d'Arc, Cj= Ceja, BH = Big Heart, GH = Grey Horse, PS = Pearsonia, WC = Wild Creek). (c) West to east spatial distribution of total number of mapped faults in each survey, size of the interpreted surveys, fault areal density and intensity. (d) West to east spatial distribution of fault-related vertical separation (Vsep) measured at the top-basement interpreted horizon. The histogram represents the overall statistics of the measurements, and the main plot shows the trend of the maximum Vsep measured in each seismic volume. Distance estimations of vertical separation are based on a constant basement velocity of 6000 m/s as reported by Kibikas et al., (2020).

DISCUSSION

BASEMENT DEFORMATION IN NORTH-CENTRAL OKLAHOMA

BASEMENT-BOUNDED IGNEOUS INTRUSIONS

The pervasive, intra-basement reflectors observed in the study area have been previously interpreted to be either basement fault damage zones (Liner, 2015) or igneous sheet intrusions (Elebiju et al., 2011, Kolawole et al., 2020). The fault damage zone interpretation lacked supporting independent data and is primarily amplitude-based. The intra-basement reflectors show a trough-peak-trough, also observed in the datasets analyzed in this study (e.g., Figure 3a-b). Using the American convention for polarity, this wave train would represent a boundary across which impedance decreases (i.e., negative RC boundary). However, without proper knowledge of the phase characteristics with depth, strong side lobe effects, etc., in the seismic data, such an interpretation of the IBRs may be erroneous. The IBRs observed in this study are like those observed elsewhere in the granitic basement of the central US Mid-Continent and are interpreted to be composed of mafic materials associated with the Precambrian Mid-Continent Rift (Hinze et al., 1997). The structure and distribution of the IBRs, which include shallow dips, segmentation,

limited spatial extents, and common cross-cutting geometries, are consistent with IBRs observed in some other geologic settings (e.g., Cartwright and Hansen, 2006, Magee et al., 2016).

To better understand the composition of the IBRs, we consider observations in the basement-penetration well data within the study area (~ 1.2 km basement-penetration Wah-Zha-Zhi well, Osage County, Chopra et al., 2018) and SW of the study area (120 m basement-penetration KF2 well, Kingfisher County, Kolawole et al., 2020). The Osage County basement cuttings showed granite, rhyolite, and gabbro chips, and more compellingly, the Kingfisher County basement cuttings and wireline logs show alternation of granite and gabbro/diabase rocks. Analysis of the seismic reflection signature and forward modeling of the well log data of the Kingfisher County basement units suggest that the IBRs are, in fact, mafic igneous sill intrusions in the basement of Oklahoma (Kolawole et al., 2020).

Furthermore, the pervasive discontinuity lineaments that cut the IBR surfaces (Figure 4) provide additional insight into the nature of the basement deformation. The trends show low energy ratio similarity signatures and commonly offset the IBR packets by a small amount. These characteristics were also observed in the Kingfisher Co. basement and have been interpreted as intra-basement faults, among which some may have been reactivated and propagated up into the sedimentary cover sometime after the emplacement of the sills (Kolawole et al., 2020).

Basement Faulting and Deformation of the Basement Surface

A study by Guo and George (1999) analyzed faulting across the midcontinent (e.g., Oklahoma, Kansas, Nebraska, and Iowa). The authors found that there are three predominant fault trends across the midcontinent. These are NE-SW, WNW-ESE, and a minor trend N-S, which is controlled by the NFZ. This previous observation supports our observations of a minor trend following 005° and two major trends along 056° and 283° (Figure 8). The study conducted by Guo

and George (1999) also found similar dominant faults and fracture trends which appear in overlying sediments and at the surface. Based on this observation, the authors concluded that there had been multiple stages of reactivation, which have facilitated propagation to the surface. We do not observe any evidence of faults propagating to the surface. Schwab et al. (2017) examined a seismic survey in south-central Kansas and found similar features to those shown here (basement highs, fault traces at the top basement surface). They interpreted a single 3D seismic reflection

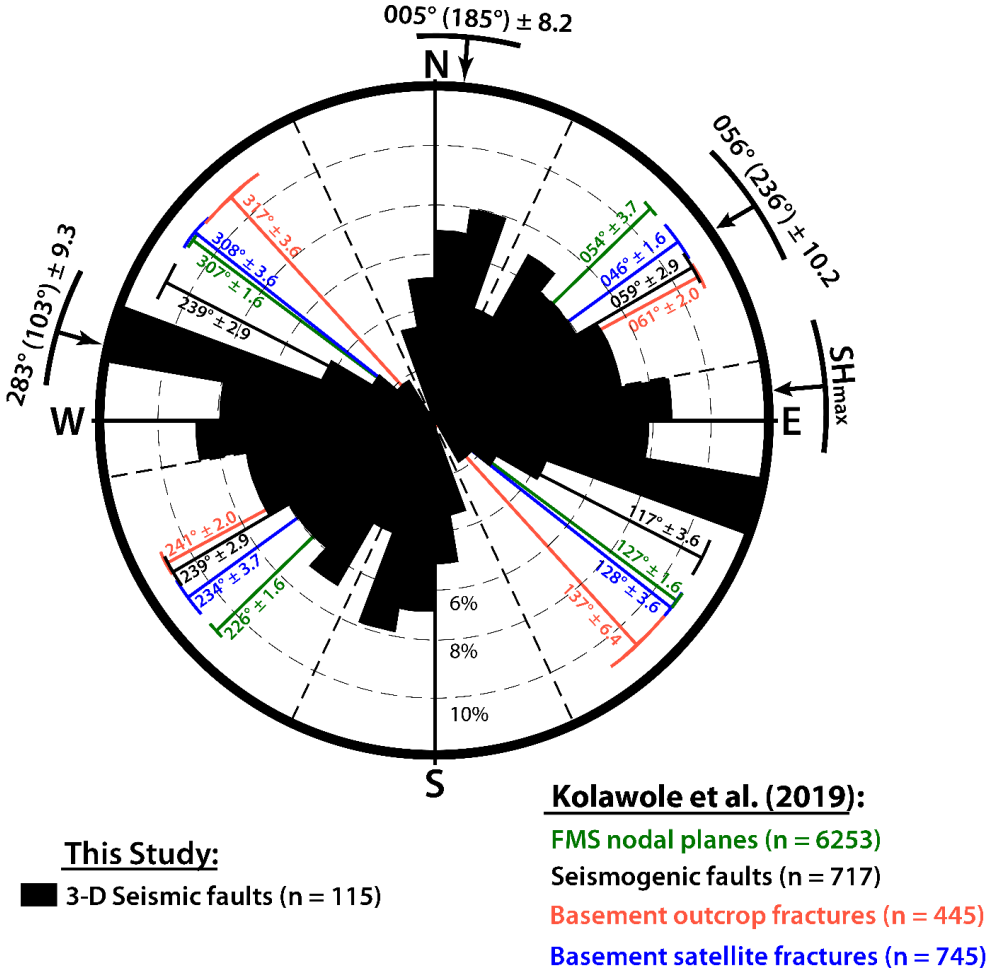

Figure 8: Comparison of 3D seismic fault trends with the regional basement fabric. Rose diagram of fault strikes mapped from the top-basement surface of the eight seismic datasets overlaid on a rose diagram of mean trends of basement faults mapped from various independent methods (trends modified after Kolawole et al., 2019). Structural trends are described as 'mean trend (= mean trend + 180°) ±. Grey dotted lines = dividing lines for the 3D seismic fault prominent trends; S_{Hmax} = present-day regional maximum horizontal compressional stress direction (from Alt and Zoback, 2016; Qin et al., 2019). The plots show that the regional NE-SW and NW-SE dominant trends align considerably well with the NE and WNW-to-NW mean trends in the 3D seismic faults.

volume to find deep faults and assess the seismic hazard. In total, they found 12 steeply dipping faults, of which three cut down into the basement. Their trends of N and N-NE are consistent with our observations in north-central Oklahoma.

Further research conducted by Kolawole et al. (2019) examined multiple data types (field and satellite interpretations, FMS nodal planes, seismogenic faults) to identify preexisting faults and fractures in Oklahoma's Precambrian basement. The authors combined multiple methods of fault and fracture identification to define the nature of the existing basement structure clearly and definitively. These include faults identified by relocated earthquake data, fractures identified in outcrop, fractures identified from satellite images, and nodal planes from focal mechanism solutions. The results from their analysis show predominant trends of faults and fractures in the NE-SW and WNW-ESE directions. These resultant trends match two of those presented in this work, with the WNW-ESE trend being the worse of the two fits. In the results of Kolawole et al. (2019), the most westward trend is 297°, while in this work, the mean azimuthal direction for this general WNW-ESE trend is 283° ±9.3. (Figure 8). This discrepancy is relatively minor and still supports the assertion that a predominant trend of faults and fractures exists in the Precambrian basement. The other trend (NE-SW) shows excellent agreement with the prior work (Figure 8). The mean trend of 056° falls directly within the grouping of those shown in Kolawole et al. (2019).

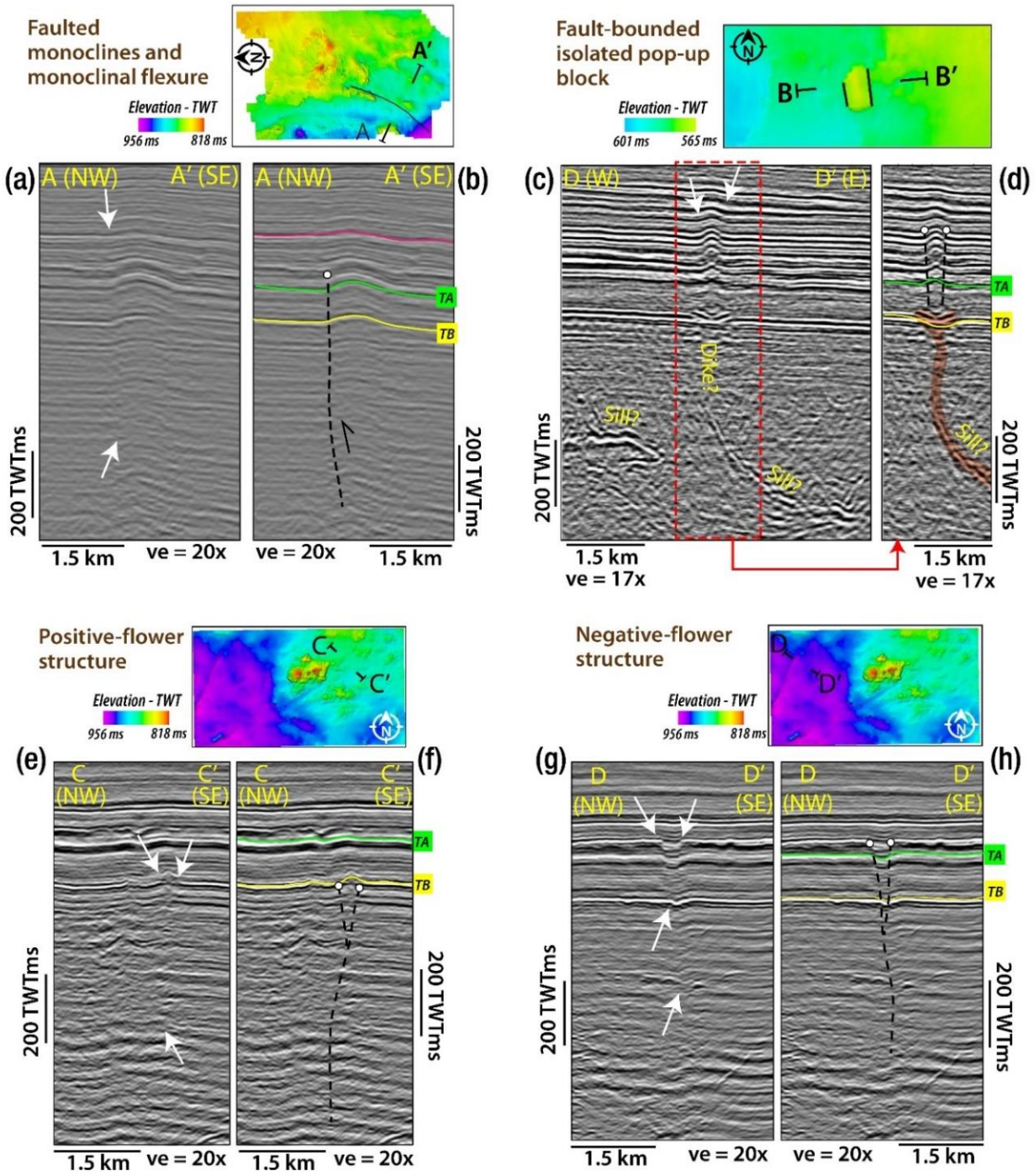

Figure 9: Structural styles of basement-rooted fault in the study area. (a-b) Faulted monocline and monoclinal flexure (representative example from Bois d'Arc survey). (c-d) Fault-bounded isolated pop-up block (representative example from Grey Horse survey). (e-f) Positive-flower structure (representative example from the Wild Creek survey) (g-h) Negative-flower structure (representative example from the Wild Creek survey). For each cross-section, the location of the line is shown in map view below.

There have been two other geophysical studies that focused on basement structure in Osage County, Oklahoma. Elebiju et al. (2011) considered both seismic and aeromagnetic data for fault interpretation and found that in the region, faults had a clearly dominant NE-SW trend for subsurface structures. Our results, however, do not show the same dominance of the NE-SW trend. Instead, the NE-SW and WNW-ESE trends appear somewhat similar in frequency to one another, with the WNW-ESE trend being slightly more dominant (Figure 8). A possible explanation for this lies in both seismic coverage and resolution. In terms of coverage, the surveys are limited spatially. As previously mentioned, the resolution of these seismic volumes is quite poor at depth (approximately 30 m). The faults interpreted in the study are generally relatively large in spatial extent, with the smallest being approximately 0.5 km long. Therefore, if there are many small WNW-ESE striking faults, it is unlikely that they would be captured in our interpretation. We do, however, see an instance of fault intersection like that in Mai et al. (2014) within the Big Heart survey (Figure 3c). On the top of the basement, numerous NE-SW striking faults appear to be disrupted by a pair of WNW-ESE faults (Figure 3c). This is supported by the observations made in Mai et al. (2014). Here they see a common occurrence of close to east-west faults within the same region of investigation.

Based on prior work which defined the geometry of the Midcontinent Rift in Oklahoma (Stein et al., 2014), it appears as though this section constitutes a rift jump segment (as defined by Nelson, 1992). Our study area is located directly to the east of the interpreted Midcontinent Rift in Oklahoma. The proximity to the rift makes it likely that the deformation described in this paper is in some way related to the opening of the rift. This is most clearly shown in the rotation of the fault trends with distance from the NFZ. Based on the observed faulting patterns, two plausible hypotheses exist. The faulting pattern could suggest distinct periods of rift perpendicular and rift

oblique opening. It could also be the case that the NE-SW and WNW-ESE trends are faults associated with the more dominant (longer) N-S striking faults. Due to the supposed time of opening (Figure 2c), we believe the latter is more plausible.

A more recent study (Kolawole et al., 2020) studied a similar area through comparable methods and found results that coincide with those provided in this work. The authors used a newer 3D seismic data set to discern the structure of the basement in Kingfisher County, Oklahoma. They showed that there are clear, steeply dipping, basement-rooted faults that cut upward into the sedimentary cover. Though the study is limited to a single survey, they also observe trends like those reported here. Three large basement-rooted faults are observed within the 3D seismic volume. The faults which are observed either cut upward and through a portion of the sedimentary cover or generate monoclinal flexure. This is comparable to the results shown in this paper, with a portion of the faults showing offset in the sedimentary cover and the remainder creating folds in the units above the basement.

The quantification of maximum vertical offset for the interpreted faults reveals a compelling trend. The fewest faults were observed and mapped in the survey most proximal to the Nemaha Fault System (Bois d'Arc Survey), and the trends show an eastward increase in fault density and intensity, with an associated decrease in maximum vertical separation. This suggests that proximal to the Nemaha Uplift and fault system, most of the deformation is accommodated along with few fault segments. However, in the far-field from the Nemaha domain, deformation may be accommodated by distributed and relatively shorter fault segments (diffused strain).

Deformation of Sedimentary Sequences, Structural Styles, and Spatial Distribution of Inherited Strain

There are clear structural similarities between the structure of the top-basement and top-Arbuckle TWT surfaces extracted from all 3D surveys. Showed in the case of the Bois d'Arc survey, a large, ring-shaped structural high is clearly visible to the north. Similarly, linear basement structural highs appear on the overlying Arbuckle surface. These observations and similar seen in other surveys show a link between the basement structures and the overlying structures in the Arbuckle Group.

The proportion of basement-rooted faults that do not penetrate the cover increases eastward away from the NFZ. Additionally, the relative proportion of faults that penetrate formations shallower than the Arbuckle Group decrease away from the NFZ (Figure 7d). Faults that terminate within the Arbuckle Group occur mostly at an intermediate distance. We conclude that during the Alleghenian Orogeny, which affected the region, basement-rooted faults were primarily reactivated near the NFZ. This is perhaps why we observe more reactivated faults, of which none tipped out within the Arbuckle Group.

In the sedimentary cover, the structural link to the basement is manifested in a multitude of ways, which are expressed mainly in four simple structures: monoclinal flexure, pop-up features, negative flower structures, and positive flower structures. The most common of these is the monoclinal flexure of the sedimentary cover (Figure 9a-b). The two possibilities for the formation of these features are passive and active deformation. In the active case, the preexisting basement fault propagates into the sedimentary cover following deposition (possibly sub-seismically). In the passive case, the folding mechanism occurs as the unit is deposited through differential compaction. The second commonly observed feature is an isolated pop-up feature found in the Gray Horse survey (Figure 9b). In this case, there is a small, elliptical feature with a high amplitude to wavelength ratio, which is observed in the sedimentary cover. The feature

propagates high into the sedimentary cover and overlies a saucer-shaped feature at the top of the basement (Figure 9c-d). While the geometry of the feature is somewhat confounding due to its symmetry and amplitude. It coincides with the location of a basement sill which appears to turn sharply upward. A possibility for the cause of this feature is forced folding above a top basement intrusion. The final two examples are interpreted positive and negative flower structures from the Wild Creek survey. The positive structure shows two steeply dipping faults that appear to converge in the deep basement (Figure 9 e-f). Similarly, the negative flower structure has a steeply dipping basement fault that appears to branch near the top of the basement (Figure 9g-h). These structures both suggest the presence of strike-slip motion along their respective faults. While the exact timing cannot be determined, few features cut above the Arbuckle Group. This suggests that this regime was present in the early Phanerozoic, or the stress field which generated these features was not sufficient to propagate faults significantly up section within this study area. The second of these is more likely due to previously established Alleghenian Orogeny, which occurred during the Carboniferous, inverted the SOA, and created the Nemaha uplift.

Implications for Seismicity in Northern Oklahoma

Oklahoma sits near the center of an amalgamated continental craton at a considerable distance from any active plate boundary and thus experiences only far-field stresses. However, these stresses are still sufficient to produce natural tectonically driven earthquakes within the state. These have been recorded for decades showing an average of 21 events greater than magnitude 3 per year (Ellsworth, 2013). There is also the potential for larger magnitude natural seismicity, as evidenced by the recent (Holocene) paleo-seismic record of the Meers fault (Crone and Luza, 1990) and the 1952 Mb = 5.5 El Reno earthquake (Luza and Lawson, 1983). However, these events occur with relatively low frequency. Starting in late 2009, Oklahoma experienced a phenomenal

increase in the number of earthquakes (Ellsworth et al., 2013). This growth continued for years, eventually placing Oklahoma at the same level as California and Alaska for the most seismically active US states. Additionally, the occurrence of large magnitude earthquakes increased, with 8 of the largest ten ever recorded occurring between 2011 – 2016 (OGS, 2020). Though the precise mechanism for increased seismicity is under debate, previous studies have shown a direct correlation between the large volumes of subsurface wastewater injection and the spike in seismicity (e.g., Keranen et al., 2014; Ellsworth et al., 2015). In conjunction with this, it has been shown that many of the earthquake sequences during this period have occurred on previously unmapped faults (Walsh and Zoback, 2016; Kolawole et al., 2019). A prominent example is the 2016 Mw-5.8 Pawnee, Oklahoma event, which ruptured an unknown fault between the Stillwater and Labette faults (Barbour et al.,2017). While produced water is dominantly disposed of in the Arbuckle Group, the earthquakes are clearly not occurring in this interval. Instead, these events occur at depths between 2 and 8 km below sea level with a mean of approximately 6.5 km (Schoenball and Ellsworth, 2017), placing the events entirely within the Precambrian basement in the majority of north-central Oklahoma.

Through attribute enhancement of seismic data, this study identified 115 faults expressed at the top and downward cutting into the basement. While some of these faults appear in the Oklahoma fault catalog (most notably the Labette fault and a large NFZ segment near Peckham, OK) the vast majority had not been previously identified. The primary implication of these conclusions is on earthquake hazards within the state, as induced seismicity is occurring on unknown faults. The known SHmax orientation in Oklahoma is 085˚ ± 005˚ (Alt and Zoback, 2017), which results in a range of optimal orientations for fault failure of 40˚ – 60˚ and 130˚ – 150˚ in the current stress regime (Holland 2013). Using these orientations, the data shown in Figure 8

was examined. All faults within these two twenty-degree arcs were summed. The result was that 16.5 % of the 115 faults compiled in the study fall within the optimal range for failure. While this is true in a general sense, it does not consider some intricacies such as local stress rotation, fault history (the stage in recurrence). However, it must be noted that the main area of study (Osage County) has not experienced seismic activity comparable to the level of the surrounding counties.

Another facet of the fault interpretation was to analyze the number of faults that cut above the basement and above the Arbuckle Group. We found that ~28% of the 115 faults cut into the Arbuckle Group, and ~23% cut into the sedimentary formations above it. It is possible that a purely poroelastic response could trigger seismicity with injection in any sedimentary unit (Segall and Lu, 2015). However, there is the potential for a directed effect due to proximity to a basement rooted fault (Segall and Lu, 2015). There is also the potential for a direct influence of injected wastewater on basement faults via fluid pathways (i.e., faults and fractures). Direct fluid conduction could increase pore pressure around a fault or, in the long term, alter fault core chemistry and thus fault strength and slip potential. We identify the faults that show that deformation is not confined to the basement and suggest that fluid pathways could link the relatively shallow sedimentary units to the basement. Additionally, the spatial distribution shows more throughgoing faults proximal to the NFZ than at distal areas (Figure 7d). Thus, a higher seismic hazard is related to sedimentary fluid injection in areas proximal to the NFZ.

CONCLUSIONS

Our analyses revealed 115 basement-rooted faults that show dominant trends of WNW-ESE, NE-SW, and N-S. The prominent WNW and NE trends of the faults coincide markedly with the trends of the recent seismicity lineaments in the region. In addition to basement faulting, we also observed the presence of several intra-basement reflection packets, interpreted as Precambrian

mafic sills, which represent an additional component of basement deformation in north-central Oklahoma. The intra-basement reflectors can be observed in all the eight analyzed seismic datasets. However, they are more pervasive in some and less in others. Proximal to the Nemaha Fault Zone, the N-S fault trend appears to dominate but transitions into NE-SW and WNW-ESE further east.

Results on the first-order spatial distribution of vertical separation suggest that proximal to the NFZ, deformation is dominantly accommodated along a few elongate fault segments, and farther away, the deformation is distributed across shorter fault segments. Additionally, the shallow reaches of the fault segments suggest the potential for spatially pervasive fluid conduction. Furthermore, 16.5% of the mapped faults fall within the range of optimally oriented faults within Oklahoma, given the present-day stress field, SHmax = 085°. Of the 115 faults which were identified, ~28% cut into the Arbuckle Group, and ~23% continue upward into post-Arbuckle sedimentary units. We suggest that the presence of these through-going faults makes it possible for the conduction of fluids between the sedimentary cover and the Precambrian basement. Thus, our findings in this study provide insight into the influence of the long-lived Nemaha structure on the deformation of the basement of north-central Oklahoma.

CHAPTER 3 - 3D SEISMIC STRUCTURAL INTERPRETATION OF THE CRYSTALLINE BASEMENT WITH THE AID OF A COLLOCATED EARTHQUAKE SEQUENCE

INTRODUCTION

The increased level of seismicity within the midcontinent since 2009 has shown that there is a significant seismic hazard within a region though relatively inactive. It has been shown that in this region of induced seismicity, earthquake sequences commonly occur along previously unidentified faults and within the crystalline basement (Kolawole et al., 2019). These points have emphasized the lack of understanding of the basement within the region. It is therefore imperative that the nature of the basement structure in the area be more thoroughly characterized.

The problems with ascertaining the character of the basement within this region are numerous. On the first order, there is minimal exposure of the basement terrane to the surface. The sedimentary obscurement of the basement reduces the extent to which field-based investigation might be employed. Thus, remote sensing methods must be utilized to show characteristics of the subsurface indirectly via a given physical phenomenon. While there are several remote sensing types, the most applicable for structural interpretation are gravimetry, magnetometry, and seismic reflection. The first two of these, while helpful, rapidly lose resolution with depth, reducing the features which might be identified at the basement level. Seismic reflection data is, however, easily scalable and retains resolution better with increasing depth. The secondary issues with identifying basement-rooted faults in Oklahoma are their relatively small across fault vertical offset and lack of coherent reflectors within the basement interval. These issues make the interpretation of basement faults via conventional seismic interpretation (e.g., amplitude and coherence volumes) ineffective. Thus, new methods and attribute combinations must be constructed and applied.

Area (km^2)	IL x CL (m)	Record Length (s)	Sample Rate (ms)	Effective Bandwidth (Hz)
44	33.5 x 33.5	2.8	2	25 – 75

Table 1: Survey parameters for the Harper Creek 3D Seismic.

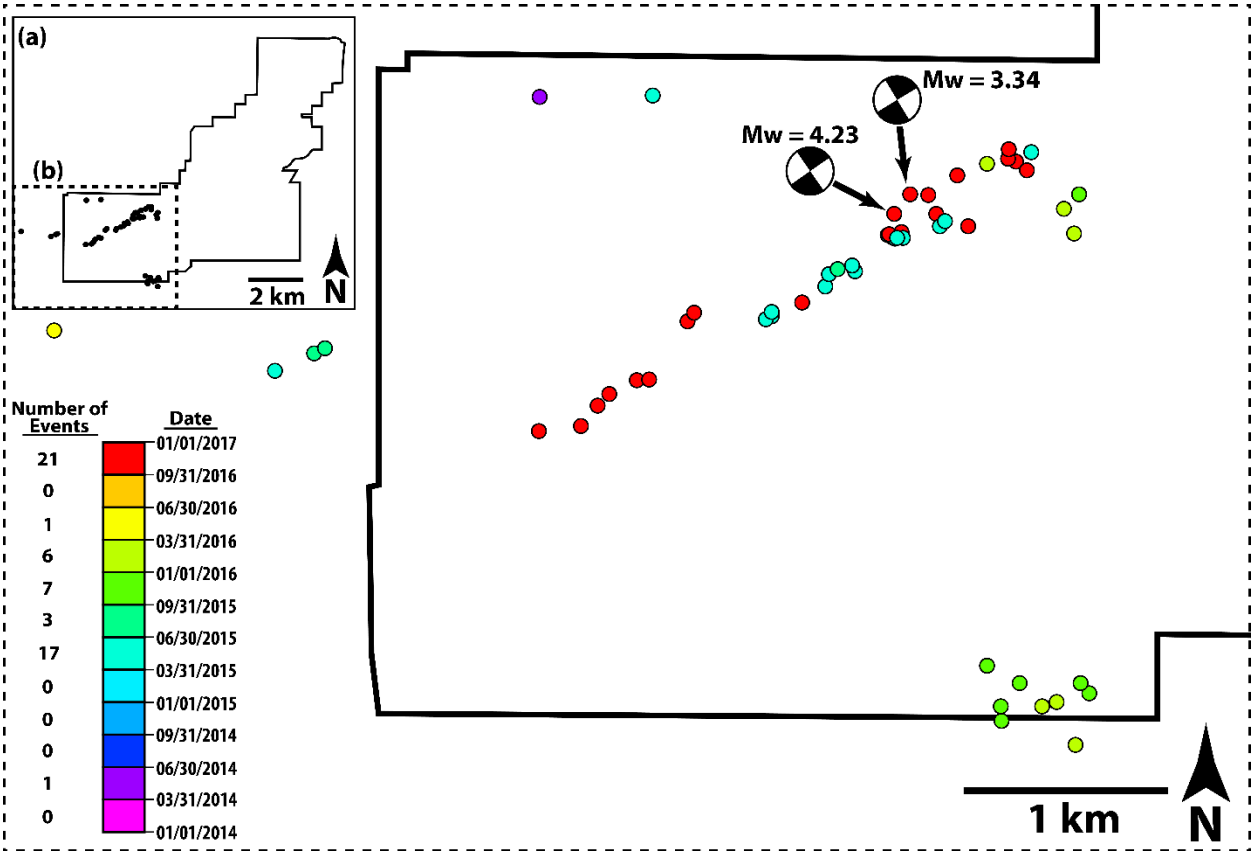

Figure 10: Harper Creek Earthquake Sequence (a) A wide and complete view of the Harper Creek 3D seismic survey and the earthquake sequence which is located within its boundaries. The HC seismic data is outlined by the solid black line and the earthquakes are represented by solid black circles. The dashed rectangle shows the spatial extents of the larger schematic. (b) Zoomed view of the southwestern corner of the HC 3D seismic survey. Earthquakes are represented by colored circles and the seismic boundary is represented by the solid black line. Two moment-tensors are shown as black and white quadrant filled circles.

In this study, a 3D seismic volume located in Pawnee County, Oklahoma, is interpreted using a suite of structural attributes. This interpretation aims to illuminate basement-rooted faults and their influence and expression on the overlying sedimentary units. In addition, a desired

coupled with this analysis is the inclusion of an earthquake sequence of which most events lie within the boundaries of the 3D seismic survey.

DATA AND METHODS

3D SEISMIC DATA: THE HARPER CREEK VOLUME

The 3D seismic volume which is analyzed in this section was provided courtesy of Chesapeake Energy Corporation. The volume extends approximately 8.8 km from the northernmost to the southernmost points and 10 km from the westernmost to the easternmost points. With inline spacing of 33.5 m (oriented E-W) and crossline (oriented N-S) spacing of 33.5 m (Table 1), these distances correspond to 265 inlines with live traces and 306 crosslines with live traces. Overall, the survey covers 44 km^2, the exact geometry of which is shown in Figure 10a. The data has a sample rate of 2 ms and a record length of 2.8 s (Table 1). It was provided as a series of full offset, post-stack time migrated volumes.

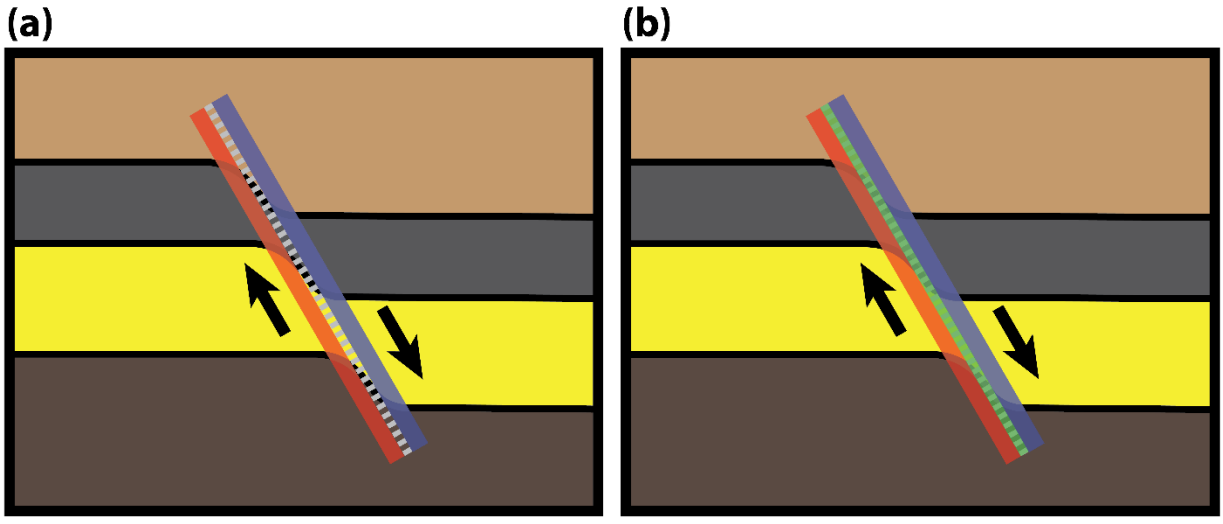

Figure 11: Fault Expression of Curvature and Aberrancy (a) 4-layer geologic model with a single normal fault represented by the gray dashed line. The blue region to the right represents an area of negative curvature while the red region represents positive curvature. (b) An identical schematic to that of (a), however, the fault trace is shaded green to represent the aberrancy signature.

INTERPRETATION PROCEDURES

Interpretation of the Harper Creek 3D seismic survey began with the identification of the primary horizons of investigation. These were determined to be those near the top of the Arbuckle Group, near the top of the basement, and a deep, pervasive intra-basement reflector. As the sole interest in the study was determining the structural character of these three interfaces, several phase positions were interpreted. The phase position which was chosen to represent the near top of each interval was the reflector which yielded the most continuous and high confidence seismic horizon. For the top-Arbuckle, this was a z-crossing (position where the amplitude is zero between a peak and trough). While for the top-basement, the selected phase was a high amplitude trough.

The primary goal of the study was to identify large faults at the top of and within the basement. Several seismic methods were explored to enhance those features which might indicate fault presence. The main tool employed to accomplish this and interpret faults at the basement-sediment interface were seismic attributes. Prior studies have attempted similar methodologies in the same geographic region with positive results. The first of these showed the value of curvature in subtle fault illumination (Mai et al., 2014). In the years following this, this work was expanded by co-rendering the principal curvatures and a coherence attribute (Kolawole et al., 2020; Firkins et al., 2020). It was then shown that while curvature illuminates a significant number of faults at the top basement, adding aberrancy can increase the number of interpretable fault traces and improve fault trace placement (Patel et al., 2021). While a suite of attributes was tested to determine their efficacy in enhancing structural features and suggesting best practices for fault interpretation, five were chosen. These are energy-ratio similarity, most-positive curvature, most-negative curvature, aberrancy total azimuth, and total aberrancy magnitude. These were separated into two groups which were then co-rendered on a shared surface. The first group was energy ratio

similarity, most-positive curvature, and most-negative curvature (Figure 14a-c). The second attribute grouping was aberrancy total azimuth and aberrancy total magnitude.

The reason for selecting the first series of attributes was the efficcy of the combination which was shown in Chapter 2 and previously published studies (Mai et al., 2014; Kolawole et al. 2020; Firkins et al. 2020). Energy ratio similarity is a proven means for discontinuity identification in seimsic data and provides a base for the co-rendering of the two principal curvatures. The principal curvatures were calculated to show regions of high flexure which form lineaments.These linear curvature anomalies at the top basement represent deformation fields associated with faulting. The second set of attributes was selected due to their enhancement of the fault zone and its extents. Total aberrancy azimuth shows the direction of change in curvature. Regions which form linear zones of consistent azimuth suggest fault prescence and may aid in fault interpretation where the flexural differential is small. Total aberrancy magnitude shows how quickly curvature changes spatially. By changing the opacity of this attribute, the most anomalous values can be isolated which are expected to represent the core of fault zones which are the most appropriate location for fault trace placement.

The first attribute we consider, energy ratio similarity, is a form of coherence, which has been applied for several decades, primarily for discontinuity identification (Bahorich and Farmer, 1995). Here, the attribute is selected to reveal displacement in the interpreted horizons associated with potential faults. The means by which this method works is in the analysis of the time-series data to determine where changes between and along traces occur. In particular, the energy ratio similarity attribute is a comparison of the ratio of coherent and total energy between adjacent analysis windows.

The curvature attributes were computed in AASPI using its dip-guided volumetric curvature algorithm. Inputs for this calculation are inline and crossline dip volumes (also computed in AASPI). While other forms were tested, long-wavelength curvature is selected for final computation as the desire was to identify large-scale structures. Most-positive curvature shows regions of convex upward flexure, while most-negative curvature shows regions of convex downward flexure. Aberrancy is the third derivative of structure or the first derivative of curvature and can be described by both azimuth and magnitude (Qi and Marfurt, 2018). While the resulting co-rendered curvature-similarity map is sufficient to interpret most of the fault traces present at the top-basement surface, there is some ambiguity in the position and extents of the curvature lineaments (Figure 11a). To reduce ambiguity and place the fault trace nearest the center of the fault, aberrancy can be utilized. The reason that this improves the accuracy of lineament interpretation is that aberrancy shows the change in curvature in space. As it is expected that the highest rate of change in flexure due to deformation associated with a fault is present near the center, the highest values of aberrancy should occur near the fault center (Figure 11b).

Co-rendering of the attributes was performed by first creating a number of surfaces equal to the number of attributes to be co-rendered for a given map. Each surface was then taken and the nearest value to the surface was extracted and stored as a surface attribute. Once this was completed, the color bar for each surface attribute was adjusted such that the anomalous values for each attribute could be observed. These surfaces were then all displayed in a single window such that the surface attributes were overlain. For the first series of attributes, energy ratio similarity was first displayed, followed by most positive curvature, and then most negative curvature. The

second series of attributes started wiith total aberrancy azimuth and overlain by total aberrancy magnitude.

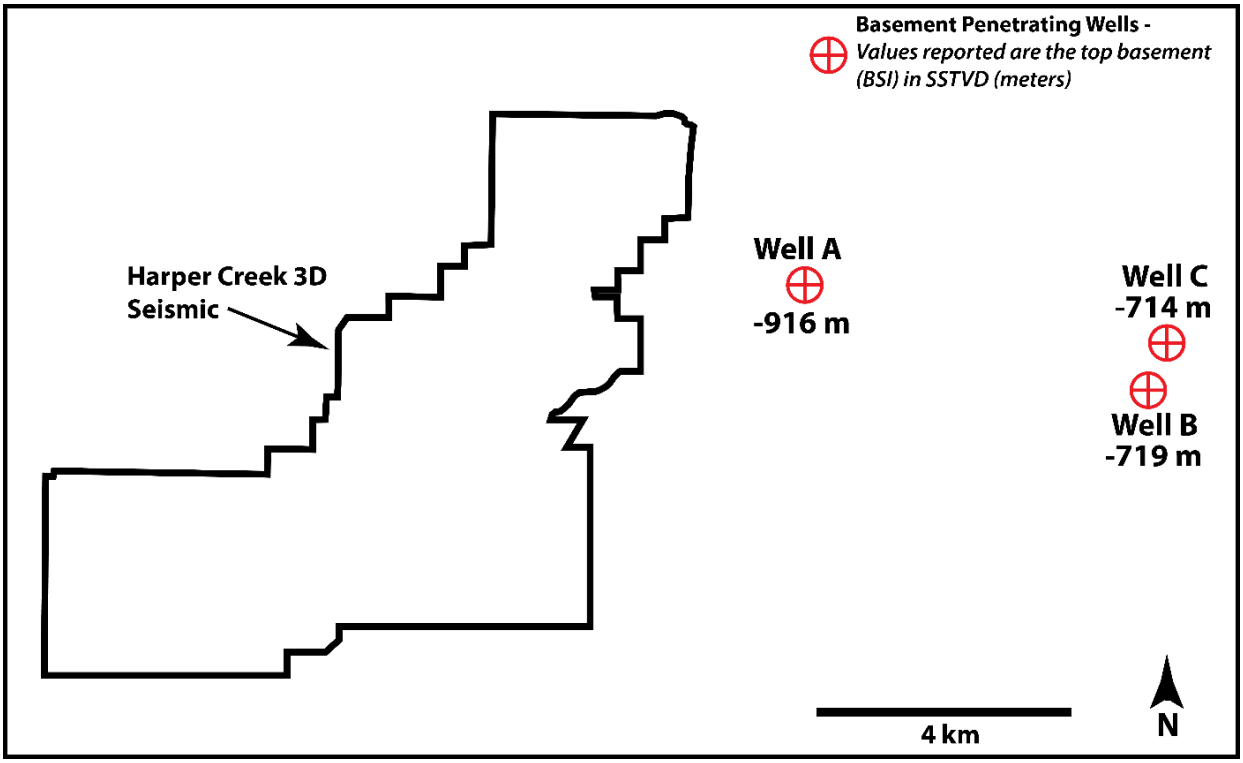

Figure 12: Basement Penetrating Wells. The position of three wells which encountered the top of the crystalline basement relative to the Harper Creek 3D Seismic Data.

In addition to the 3D seismic survey, a sequence of 56 relocated earthquake hypocenters were analyzed to provide insight into the potential character of structures within the basement, wherein seismic data may yield little information. These events are from both the OGS and USGS catalogs and vary from magnitudes 1 to 4. These events were combined from two relocation data sets. Both used a two-step method in order to relocate the earthquakes. The first step was to determine the absolute position of the events using a selected velocity model. The second step in the relocation process is to perform a relative relocation of event clusters. For both studies, the double-difference method was chosen. The method is based on the residual between differences in the observed and calculated travel times for an event pair. Underlying the method is the idea that ray paths will be similar when the hypocenter distance between the events is significantly less

than the distance to the station at which both events were recorded (Waldhauser and Ellsworth, 2000). Schoenball and Zoback (2017) choose a 1D model which is used by the OGS for their locations. However, Chen (2016) uses a tomographically derived 3D velocity model created for Oklahoma. These relocated events have decent absolute depth error with 48 % of events below 1 km error and 76% below 1.5 km absolute error.

DEPTH TO TWT ESTIMATION

The two primary forms of data that are being analyzed within this chapter are a 3D seismic volume and a sequence of 56 seismic events. The first of these shows the structure of the subsurface mechanical reflectivity as represented by two-way travel time. The earthquake data is the subsurface position of energy eminence from a seismic event represented vertically in depth. To analyze the relationship between these data, which are represented by different vertical domains, there must be a transformation of at least one data form into a new domain. As there is a relative lack of available sonic and density logs which penetrate to a sufficient depth for depth conversion of the 3D volume, it was decided to convert the seismic events to the time domain. This process was relatively straightforward as all events occurred well within the basement, which is expected to be relatively homogeneous in terms of seismic velocity. An estimation of the in-situ acoustic velocity of the basement was made by Kibikas et al., 2020. It was found that at confining pressures of 50 – 60 MPa, the granitic basement velocity was 6,000 m/s.

The initial step of conversion from earthquake hypocenters in depth to time was to determine an appropriate reference depth for the top basement surface. Using three basement penetrating wells near the survey, the basement surface was found to be approximately 1 km below mean sea level (Figure 12). This was assumed to be the depth of the basement surface across the

survey and used as the reference datum for the seismic event domain transform. Using this datum, the reported depths of all seismic events were shifted to be referenced to 1 km below sea level (subtracting 1 km from the depth below sea level). Then, an approximate TWT was selected to represent a constant depth datum for the top of the basement. This value was chosen to be 0.7 s. A one-way time was then calculated for each event by dividing the depth referenced to 1 km by the

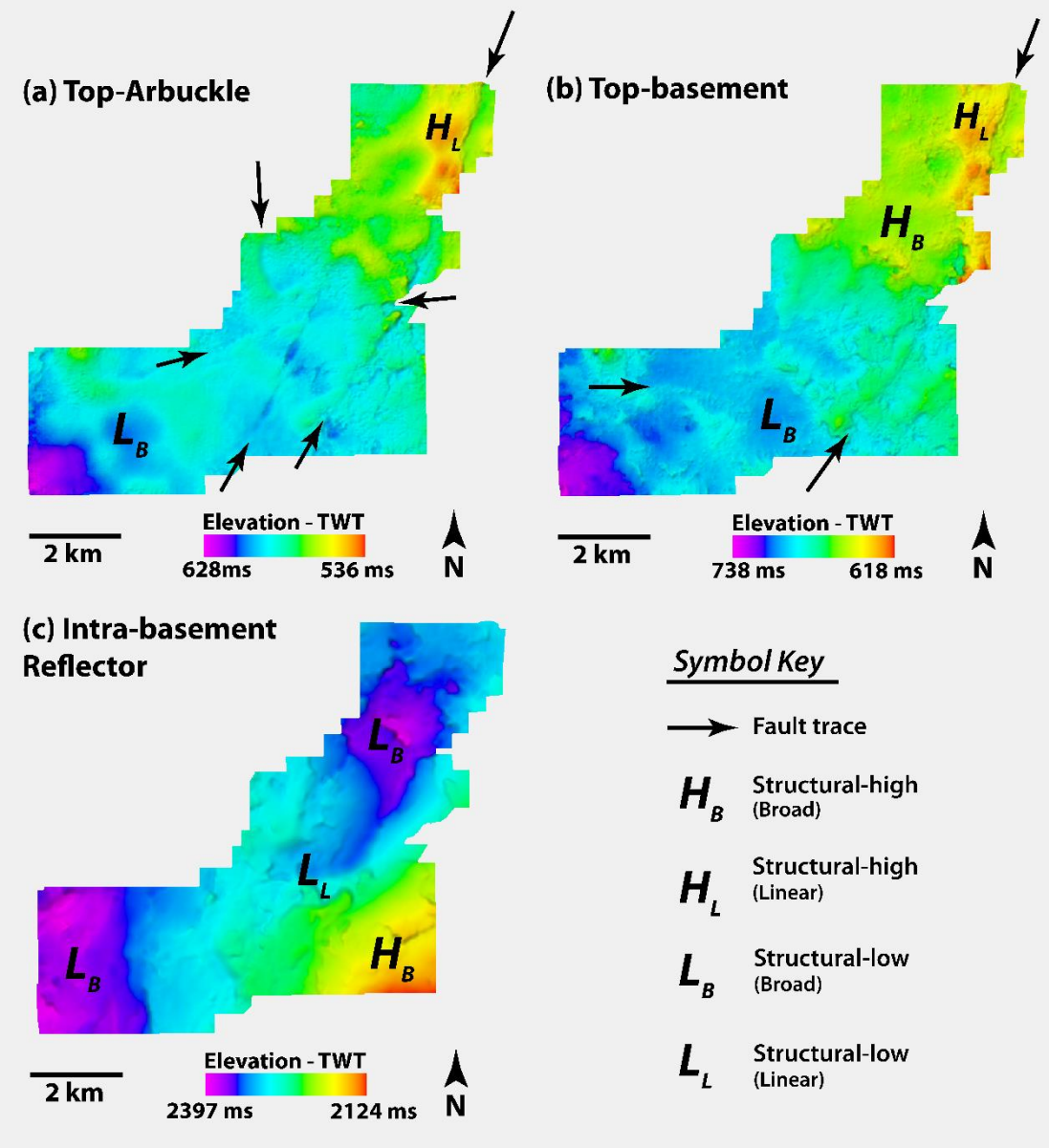

Figure 13: TWT Surfaces. (a-c) TWT structure maps of the three surfaces of interest in the Harper creek 3D Seismic.

basement velocity of 6 km/s. This time was then multiplied by 2, yielding a TWT, and then the sum with 0.7 s was found to create an approximate depth in TWT relative to mean sea level.

RESULTS

The three TWT structure maps which were generated in the study are shown in Figure 13. The Top-Arbuckle surface shows a generally homoclinal dip towards the southwest, with small TWT values in the northeast that increase (indicate deepening) to the southwest. On the surface, there are a few features of primary interest. These are a linear structural high, which is most prevalent in the northeast corner and continues, though decreased in relief, to the southern edge of the survey along with a 023° trend (Figure 13a). In the southwestern corner of the surface, there is a broad structural low near the southwest corner which is two by 1.5 km in dimension. The other features observed on the surface are four distinctive traces that show rapid changes in elevation

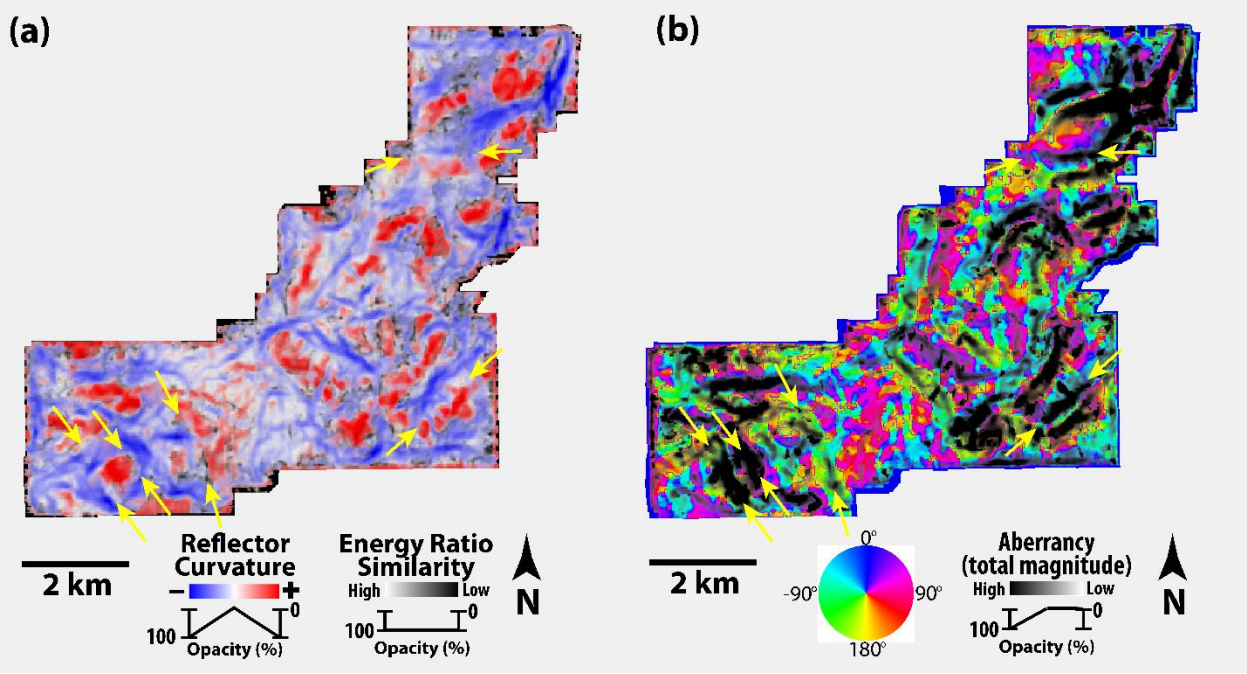

Figure 14: Attribute Maps. (a) The top-basement surface with co-rendered energy ratio-similarity, most-positive, and most-negative curvature. (b) Co-rendered total aberrancy azimuth and total aberrancy magnitude.

over limited spatial distance. These vary in azimuth from north-south to near east-west orientations (Figure 13a).

Near the top of the basement, there are similar features to that observed at the top-Arbuckle and the same near homoclinal dip towards the southwest. The first of these is a similar linear structural high, which starts in the northwest corner of the surface and continues at an 023° trend to the southern extent of the survey (Figure 13b). In the north-central portion of the surface, there is a broad structural high west of the linear high. In the south, there is a broad, circular structural low, which is approximately 2 km in diameter. Similar to the top-Arbuckle surface, there is a long linear trace that trends along with the linear high (Figure 13b). There is also a curvilinear trace apparent at the top-basement in the western section of the survey. The trace shows rapid TWT elevation changes within limited spatial extents. It begins trending near west-east and transitions to just south of the east toward the east. The final surface is that of the deep intra-basement reflector. Contrary to the two other surfaces, there is a more complex surface dip, with an extreme structural high in the southeast that decreases towards two broad lows in the west and north (Figure 13c).

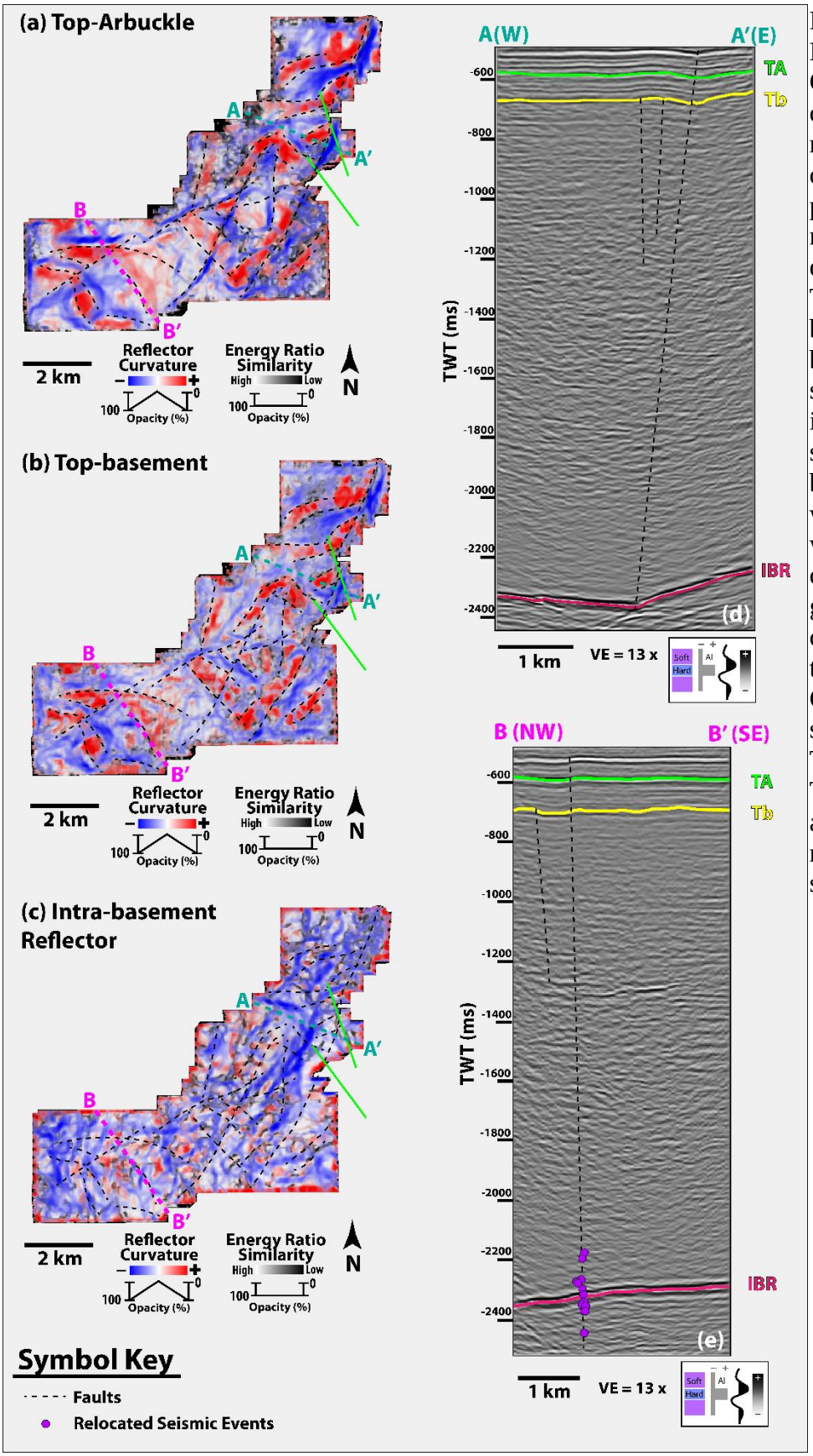

Figure 15: Attribute Maps and Seismic Cross-sections. (a-c) co-rendered energy ratio similarity and curvature (most-positive and most-negative) attributes extracted onto the Top-Arbuckle, Top-basement, and Intra-basement reflector surfaces. The faults interpreted in this study are represented by dashed black lines, while those present within the OGS catalog are drawn in green. (d-e) Seismic cross-sections through the Harper Creek data. Both show the interpreted Top-Arbuckle (TA), Top-Basement (TB), and Intra-basement reflector (IBR) surfaces.

While the TWT surfaces reveal the large-scale structure of the three interfaces, there is a limited expression of more subtle features. To enhance these, the attribute extraction outlined in the methods section was applied to the top basement surface. The resulting co-rendered surfaces show the presence of a number of features that are not revealed in the TWT structure. The principle curvature and energy ratio similarity co-render shows significantly more linear features than present on the structure maps alone (Figure 15a). These are most typically expressed as either a region of high positive, high negative, low energy ratio similarity, or any combination therein. Most commonly, the features are identified by linear positive-negative curvature couplets (Figure 15a). The features are also easily identified with a combination of total aberrancy azimuth and magnitude. These attributes show a significant number of linear anomalies which trend in varied directions for different lengths (Figure 15b). The interpretation of all faults present at the top of the basement reveals a total of 31 fault traces (Figure 15, 17; details in Appendix B). Five of these faults are considerably longer than the remaining twenty-six. Four of these five trends between NNE and ENE and one trends near east-west (Figure 15b). All are between 3 and 9 km in length and qualitatively show the most significant vertical displacement at the top of the basement and in the sedimentary units above (Figure 15d-e). The remaining interpreted faults vary in their azimuth with approximate trends of northeast-southwest, northwest-southeast, and east-west. Lengths of this group of faults are less than the five previously mentioned, with values ranging from 0.8 to 2.4 km (Figure 14b). The fault azimuth distribution shows the majority of faults identified at the top basement fall between 020° – 070° and 280° – 340° (Figure 17). Of the 31 total faults which were identified at the top of the basement, six fall into the moderate sliplikelihood category, and nine are at angles that have a high likelihood of slip in the present stress regime (Figure 17). Sliplikelihood was determined from work performed by Holland (2013), wherein the author

determined the most likely azimuths for seismic activity to be from 40° to 60° and 130° to 150°. Comparing the fault interpretation at the basement sediment interface with the top-Arbuckle and intra-basement reflector surfaces show some similarities. Looking at the two surfaces, the curvature expression is nearly identical between the top-Arbuckle and top-Basement (Figure 15a-b). All faults which were interpreted at the top-Basement are also interpretable at the top-Arbuckle. The intra-basement reflector surface does not show the level of similarity to the top-basement

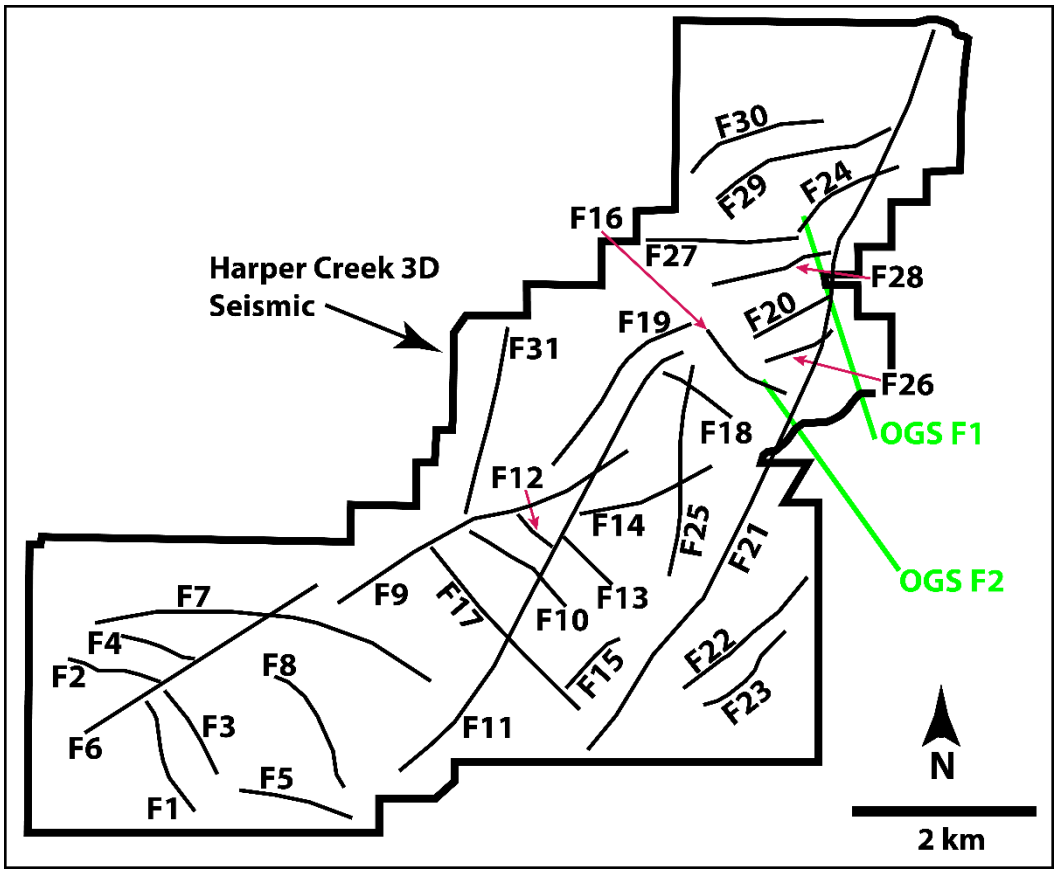

Figure 16: Harper Creek Fault Basemap. Basemap of the interpreted faults at the top-basement with number labels. Faults which are present within the OGS catalog are shown in light green.

structure. There is one lineament that clearly appears on both surfaces. This is the longest identified fault which trends at 023° for nearly 9 km (Figure 16). There are two faults whose connectivity is not discernable witht the attributes as presented. These are Faults 6 and 9 both of which strike approximately 060° and as presently interpreted nearly overlap at the northeastern terminus of

Fault 6 (Figure 16, 17). It was chosen to keep these faults separate as both in the attribute extractions and in amplitude cross-section there is no deformation indicative of faulting present.

In cross-section, the faults which were interpreted via map view appear as either vertical displacement or rapid and severe change in the dip of the top-basement horizon (Figure 13d-e). These commonly have associated zones of disrupted amplitude which extend into the basement at

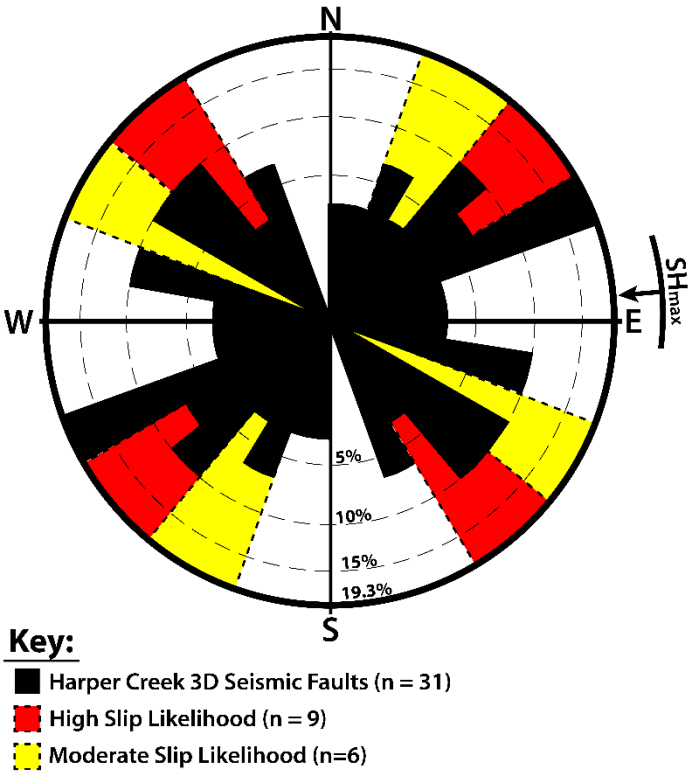

Figure 17: Harper Creek Fault Azimuthal Frequency. Rose diagram which shows the azimuth frequency distribution of the 31 faults interpreted at the top of the basement. There are four unique azimuthal ranges colored by likelihood of slip as indicated by Holland, 2013. SHmax = present-day regional maximum horizontal compressional stress direction (from Alt and Zoback, 2016; Qin et al., 2019).

high angles (vertical to sub-vertical). However, not all faults are clearly interpretable from the top-basement interface and through the entirety of the basement (Figure 15d-e). The long, northeast-southwest striking fault on the western side of the survey appears coincident with the primary sequence of earthquakes, which lies within the boundaries of the survey. Looking in cross-section,

there is the displacement of the top-basement surface directly above the sequence's position at depth, with small amplitude disruptions between the two (Figure 15e).

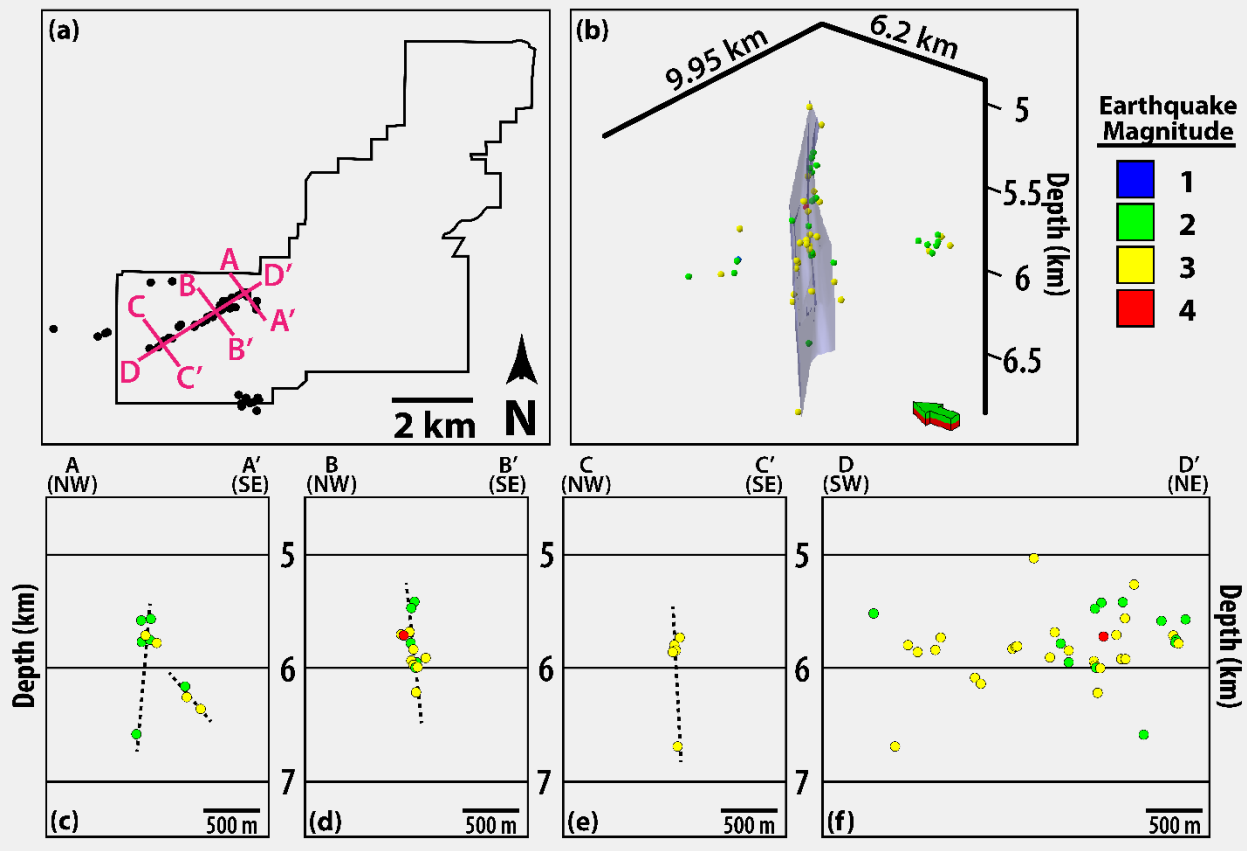

Figure 18: Earthquake Sequence in Depth. (a) Basemap showing the location of the Harper Creek 3D seismic data and the earthquake sequence being examined. Cross-section locations shown in (c-f) are recorded. (b) 3D view of the 56 relocated earthquakes analyzed in the study colored by magnitude. The display is at true scale and an interpreted fault plane is shown in transparent blue. (c-f) Depth cross-sections of the seismic events colored by magnitude and displayed at true scale. Dashed black lines are fault plane interpretations.

The earthquake sequence of interest, which lies within the Harper Creek data, predominantly falls along a single trace when visualized in map view with two smaller trends to the northwest and southeast (Figure 18a). When expanded to view in 3 dimensions, the primary sequence forms a near-vertical plane which extends from approximately 5 to 7 kilometers depth and along strike for 4 kilometers (Figure 18b). It is along this plane that all three magnitude four events occurred as well as the majority of magnitude three earthquakes. In cross-section, the

structure of the fault zone can be examined in more detail. Towards the northeastern edge of the sequence, there is a clustering of events near 6 km depth with a single event at approximately 6.75 km. To the southeast of these events is another cluster of earthquakes that delineate a separate, small fault plane dipping near 45° (Figure 18c). The events at this end of the earthquake sequence are all magnitude 2 or 3. Stepping to the southwest by approximately 1 km, there is a considerable increase in the vertical distribution of earthquakes, showing a clear, linear, near-vertical trace that extends from approximately 5.5 to 6.25 km (Figure 18d). Also present at this point along the sequence are all three magnitude four events. Two of these occur at 5.75 km and the third at approximately 6.25 km (Figure 18d). Moving towards the end of the sequence, a similar geometry

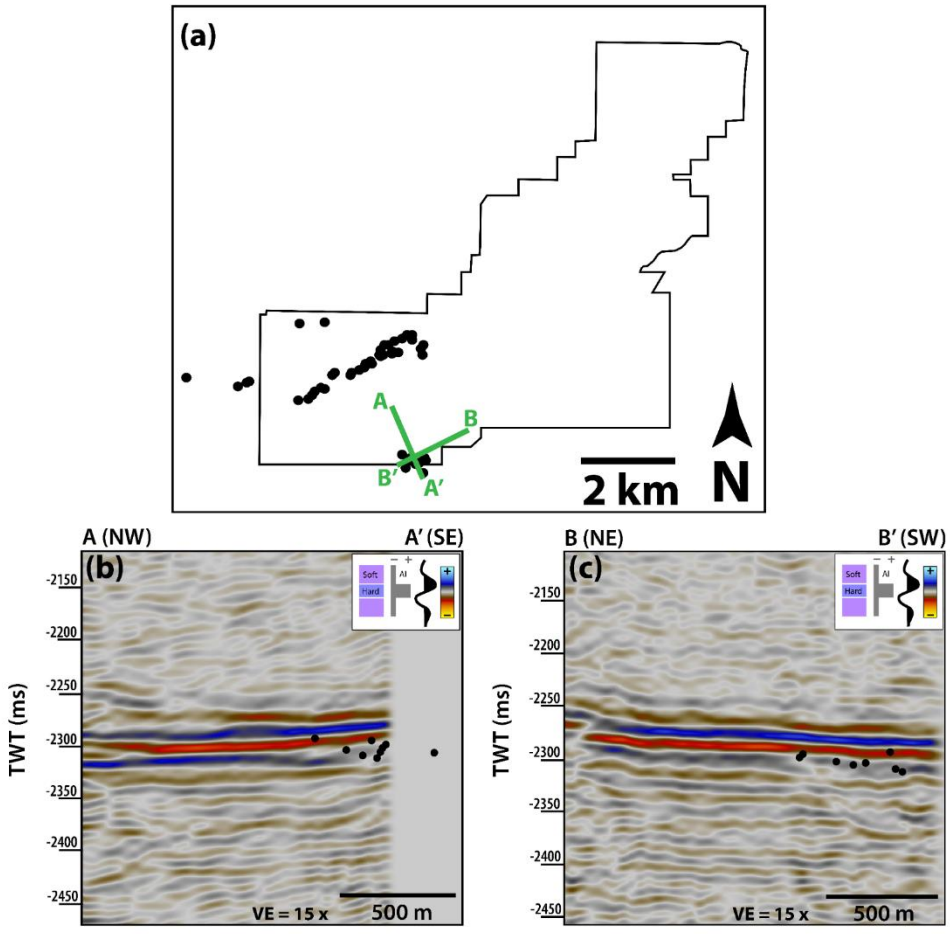

Figure 19: Horizontal Seismic Events. (a) Basemap of the Harper Creek 3D Data with the earthquake sequence and location of the below cross-sections displayed. (b-c) Seismic cross-sections through the Harper Creek 3D seismic. Black circles show the location of the earthquakes.

is observed to cross-section A-A'. A cluster of magnitude three earthquakes are present at 5.75 to 6 km, and a single event is observed at 6.75 km. This suggests a near-vertical fault zone is present with a slight dip towards the southeast (Figure 18e). A strike parallel cross-section of the earthquake sequence in depth shows that the distribution of events is confined to a narrow zone in the subsurface. The majority of main sequence events fall between 5.5 and 6.25 kilometers in-depth (Figure 18f). While the events are relatively evenly distributed within this rectangular area, more earthquakes are observed in the first 1 km of the sequence from the north than in the remainder of the fault zone. In addition to this, the three main events of the sequence occur within 0.5 km of one another vertically and are no more than 200 m apart laterally (Figure 18f).

As mentioned in the method section, the earthquakes which were provided in depth were converted to the time domain to facilitate integrated interpretation of the data. The result of this transform revealed that the primary sequence of events is centered on the deep intra-basement reflector observed between 2.1 and 2.4 seconds (Figure 15e). Comparing the events in depth and time, the intra-basement reflector is between 5 and 7 km depth (4 to 6 km below the top basement). While the primary sequence of earthquakes shows a rupture sequence perpendicular to the intra-basement reflector, the smaller sequence to the southeast displays a distinctive character. When viewed in a seismic cross-section, the events suggest a near-horizontal zone of slip which aligns closely with the intra-basement reflector (Figure 19b-c). These events appear to be located near the base of the intra-basement reflector.

DISCUSSION

BASEMENT FAULTS AND SEDIMENTARY STRATA

The deep intra-basement reflector observed within the Harper Creek Data show similarity with those described previously within the region (Elebiju et al., 2011; Kolawole et al., 2020; Firkins et al., 2020). These have been concluded to be mafic sills and sheets that intruded the granitic basement at some point prior to the deposition of the Reagan Sandstone and Arbuckle Group in the early Ordovician. The lack of discontinuities observed on the intra-basement reflector surface suggests that while the faults observed at the top-basement may be present, they have not experienced identical deformation.

The high degree of similarity between the structure at the top-basement and top-Arbuckle surfaces suggests a significant influence of the top-basement structure on the Arbuckle Group during its deposition. Structural highs and lows appear in similar locations across the two surfaces. These are generally of higher amplitude at the top basement and decrease moving upward stratigraphically, with limited thickness changes in the overlying units. This suggests the structure observed at the top basement was present prior to the Arbuckle Group and remained inactive throughout its deposition. There is also a more significant offset of reflectors across faults near the top-Arbuckle (Figure 15d-e). This suggests that while faults may be present within the basement and above. Looking at specific structures, there is an indication that the faults which are observed at the top-Arbuckle are relatively immature and likely postdate those within the basement. This evidence is a combination of en-echelon geometry and faults centralized slip observed on the faults (Figure 13a). The segmentation of these faults, which appear cohesive at the top basement, suggests this is a younger portion of the fault at this level. Likely, these smaller segmented faults

formed after the deformation, which contributed to the Precambrian basement faults. The preexisting weakness that was exploited resulted in a series of short, limited offset, en-echelon fault segments, which trend along with inferred basement faults.

There have been a number of recent papers have sought to ascertain the nature of basement faults within Oklahoma and the potential associated seismic hazard. While the methods vary, their results are similar to those found here. Kolawole et al. 2020 and Patel et al. 2021 used slightly varied methods of basement fault interpretation, but achieve similar general conclusions. They show that a number of basement-rooted faults can be identified via attribute guided interpretation. While the faults shown in this work are lesser in number, they show similar characteristics to those observed in the survey shown above. The faults trend in a number of orientations including approximate trends of north-south, northeast-southwest and northwest-southeast. The faults show offset at the top basement which continues often continues into the overlying sedimentary sequences. While in a distinctive region of the state, the structures and their distributions are similar to those observed in the above work. Faults, though more diffuse, still suggest dominant trends between northeast to east-northeast and northwest to west-northwest. In Qin et al. (2019) a large number of relocated earthquakes and high-quality focal mechanism solutions were analyzed. These were used to interpreted presently seismogenic faults and generate an improved stress map for Oklahoma. The authors found that the seismogenic faults are typically of high dip, with the large majority dipping steeper than 70° with a small proportion dipping sub-horizontally (less than 35°). Additionally the faults which are east of the Nemaha Fault Zone group along east-northeast and east-southeast. The results shown here similarly suggest that the primary fault which are hosted the primary seismic events of the analyzed sequence is steeply dipping and trending ENE.

These works have two primary distinctions from that which is shown here. The first and foremost is the quality of the data which is examined. The surveys which were analyzed in Kolawole et al. (2020) and Patel et al. (2021) were both of relatively recent vintage and purported to be of high quality. In this study, the data was both acquired and processed in the 1980s. There have been significant improvements in processing methods and algorithms over the decades, which have improved the overall quality of final seismic data images. The second distinction is in the setting of the studies. These are both located in the STACK region of Oklahoma, which is in the west-central area of the state, west of the Nemaha Fault Zone. In work presented above, the setting is approximately 100 km to the east. While there are apparent similarities in the overall structures observed, there are distinctions. The distance between the study areas is expressed as a is in the character of the basement zone visible in the seismic surveys. In both works mentioned above, there are a larger number of visible and interpretable intra-basement reflectors. These features aid in constraint of the fault trace locations and interpretation confidence both at the basement-sediment interface and into the basement.

Best Practices in Basement Fault Interpretation

Recent works have expanded the ability for subtle fault detection using seismic attributes. These show that even with diffuse deformation or offset below resolution, faults and fracture zones might be identified. The first analyzed a survey in a similar geographic setting. The authors found that while curvature can illuminate a large number of basement-rooted faults, aberrancy improves subtle interpretation (Patel et al., 2021). This is due to aberrancy showing the zone in which curvature is changing most rapidly, which is assumed the most likely location for fault position. In the above work, a similar result is shown. Curvature lineaments, particularly where there is a change from positive to negative curvature, allow for relatively straightforward fault interpretation.

However, there is some uncertainty in trace placement and continuity. Aberrancy reduces this by highlighting the zone of most significant flexure and improving interpretation confidence. Another work attempted to ascertain a more comprehensive workflow for subtle fault and fracture zone interpretation. They show the importance of multi-attribute analysis in the determination of subtle fault locations (Hussein et al., 2021). Additionally, they suggest a machine learning process that could improve fault interpretation in the midcontinent.

As much of the granitic basement which was being analyzed in the study lacked coherent and continuous internal reflectors, there was limited opportunity for basement structure interpretation. Therefore, the only reliable means of structural interpretation is predicated on horizon interpretation. It was found that the three of primary importance are the top-basement, top-Arbuckle Group, and the most coherent intra-basement reflectors observed. Once these horizons were identified and interpreted, an initial interpretation can be made via an exaggerated TWT map of each reflector.

Following this, attribute generation and extraction were performed along these surfaces. While a variety of attributes were trialed, dip and its derivatives were found to be the most useful. In particular, the principal curvatures and the total magnitude of aberrancy. These attributes highlight regions of high dip change, which, while not significant enough to clearly show on the similarity attributes, appear when further extrema are examined. Additionally, the sedimentary units directly overlying the basement can provide hints as to the structure below. These horizons are generally of higher frequency, have high structural similarity to the basement, and at times show more significant offset than the same fault at the basement-sediment interface.

SUMMARY

Interpretation of the Harper Creek 3D seismic data using a combination of seismic attributes revealed 31 faults at the top of the basement. These results show that regions of and suggest promise in the combination of 3D seismic data and earthquake data where applicable. The faults identified range in length from 0.56 to 8.8 km in the survey and trend mostly northeast-southwest and northwest-southeast. Of these faults, nearly half are either highly or moderately likely to slip in the present stress field, one of which has hosted recent seismic rupture. These earthquakes were analyzed and showed strong coincidence with curvature and aberrancy anomalies in the seismic data. When converted to the time domain, the seismic sequence appears centered on the deep intra-basement reflector within the volume. This and a secondary clustering of near-horizontal earthquakes suggest a link between seismicity and what are interpreted to be intra-basement mafic sills and sheets.

ACKNOWLEDGEMENTS

We would like to thank Chesapeake Energy Corporation for providing the 3D seismic data which was presented in this chapter. Their data provided valuable insight into the basement structure and gave a unique opportunity to place seismic events in 3D seismic data.

CHAPTER 4: CONCLUSIONS AND FUTURE WORK

The primary purpose of the work presented was to ascertain a reliable means for which seismic data might be used to delineate significant faults and intra-basement deformation at the top of the crystalline basement within the midcontinent, and more specifically, the Southern Granite Rhyolite Province. Given these interpretations, it was investigated whether the observations that could be made on the faults revealed anything on their slip history and, therefore, the history of deformation in the midcontinent over geologic time. Additionally, the overlying sedimentary units were examined to determine what impact the basement structures had on the overlying sedimentary units.

The basement zone showed that numerous anomalous reflectors suggest zones of high impedance within the granitic basement. These intra-basement reflectors are interpreted to be mafic sills and sheets given their geometry and data from prior workers. While the precise characteristics of these sills vary between surveys, there are a few commonalities. The sills are all relatively thin (~30 m), shallowly dipping (<10°), and terminate at or before the basement sediment interface. They are also commonly faulted, though the nature of the transecting faults is varied. Some appear coincident with faults interpreted at the top basement.

The results showed 146 faults (115 in chapter 2 and 31 in chapter 3) identified via seismic attribute extraction at the top of the basement. This amounts to approximately 0.2 faults per km^2 and an average of 16 basement-rooted faults per survey. Of these, only 4 (~2.7%) were present within the publicly available fault catalog. Such a discrepancy suggests that the basement is more pervasively faulted than previously thought, with a significant number of faults likely unidentified across the state and greater midcontinent. Additionally, this method only identifies those faults which either intersect or have a discernable deformation field at the top basement. There is likely

a plethora of faults whose slip and associated deformation are contained entirely within the basement and may not be identified via this technique. A subset of 115 faults along which vertical separation data were measured show strain localization along large structures and suggest a series of successive events have contributed to the basement and sedimentary deformation observed in the region.

The work presented in the preceding chapters shows that using structural seismic attributes, subtle faults within the basement can be identified. It also reveals that the basement is pervasively faulted, and these faults and their associated fields of deformation have considerable interaction with the overlying sedimentary units. In Chapter 2, methods are shown which employ the co-rendering of energy ratio similarity, most positive curvature, and most negative curvature. This method reveals pervasive linear to curvilinear curvature couplets which are interpreted as fault traces. While this method appears to effectively capture fault associated deformation at the top of the basment, there remained ambiguity in the placement and extents of the interpreted fault traces. In Chapter 3, in addition to those attributes co-rendered in Chapter 2, total aberrancy azimuth and magnitude were co-rendered at the top-basment surface. The inclusion of these attributes aided in the placement of fault traces as aberrancy illuminates the region of greatest change in curvature.

This work can be expanded upon to include additional 3D seismic data sets within the region of interest interpreted using a similar workflow to those outlined in the above chapters. While many are interpreted here, they still fall incredibly short of providing a comprehensive and detailed characterization of the crystalline basement in the midcontinent. Adding more coverage and interpretation of the basement via 3D seismic data will add increased insight into the distribution of faults within Oklahoma and contribute to the continuing effort to mitigate seismic hazards. Furthermore, there are opportunities for more detailed analyses of the interaction and

potential control on different stratigraphic intervals properties and the structures identified via the proposed methods. Another avenue of continued investigation is the expansion of the methodology for basement-rooted fault interpretation. While there was an attempt to utilize various seismic attributes within this work, there are still those that remain untested in this region for basement interpretation. This includes another look at frequency-based or texture attributes and potentially reparameterization of attribute computation. Additionally, there is potential in the utilization of machine learning methods for structural characterization. This would include the combination of pertinent attributes via principal component analysis followed by self-organized mapping.

APPENDIX A

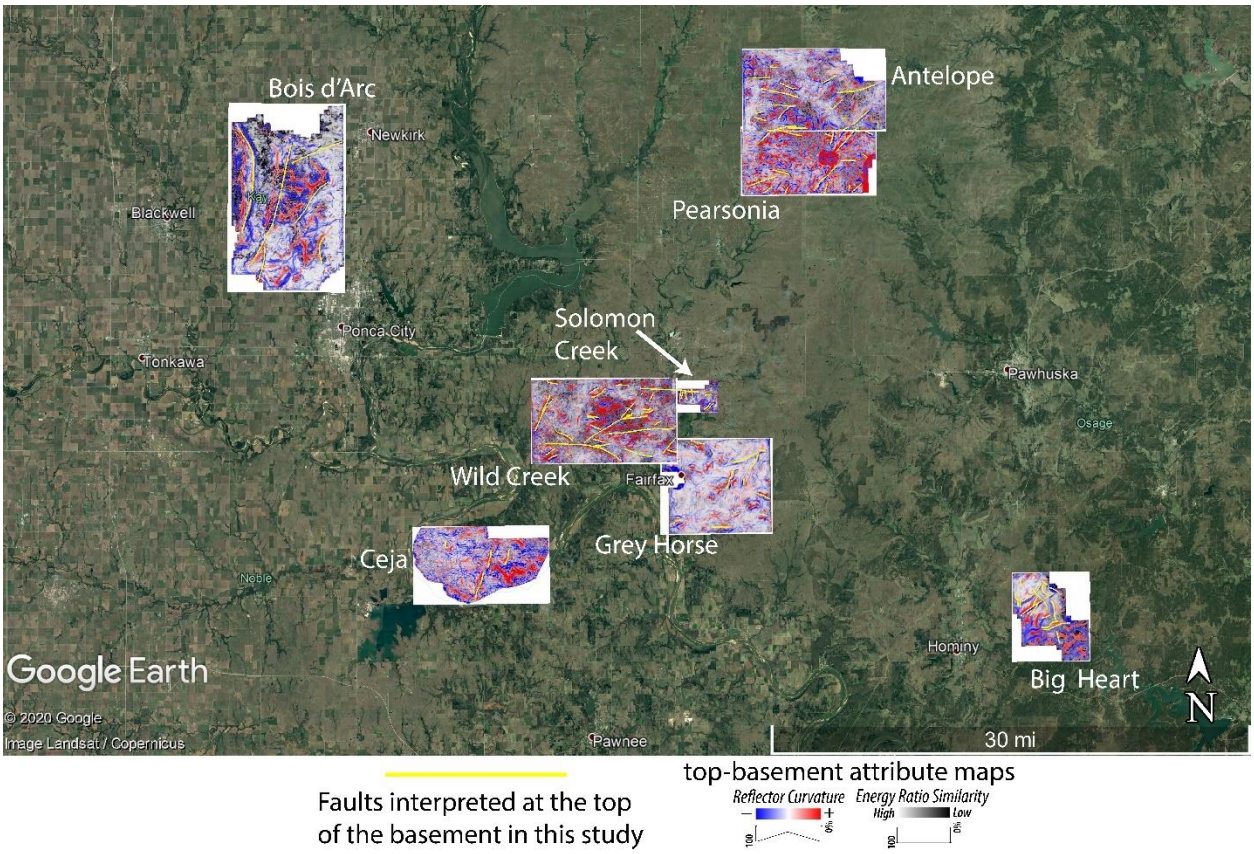

Figure 20: Regional views of all co-rendered top-basement attribute maps with the interpreted fault traces displayed in yellow.

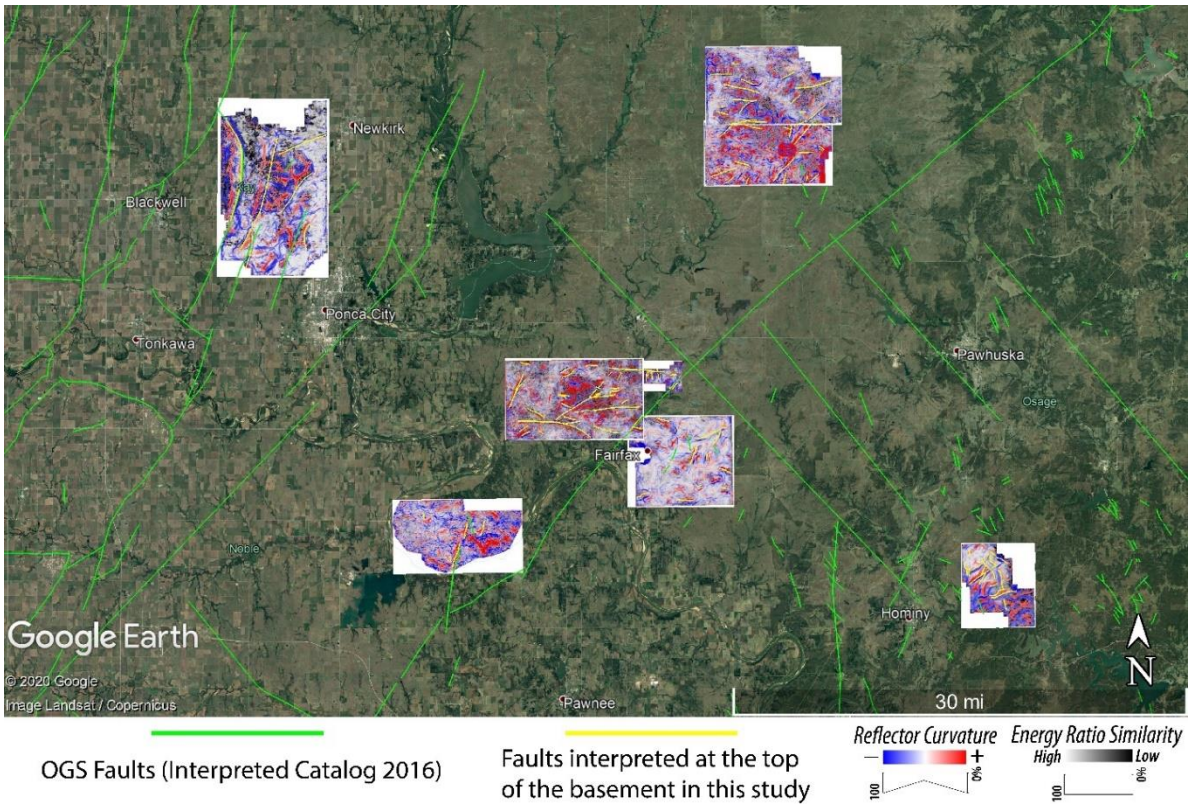

Figure 21: Regional views of all co-rendered top-basement attribute maps with the interpreted fault traces displayed in yellow and OGS faults shown in light green.

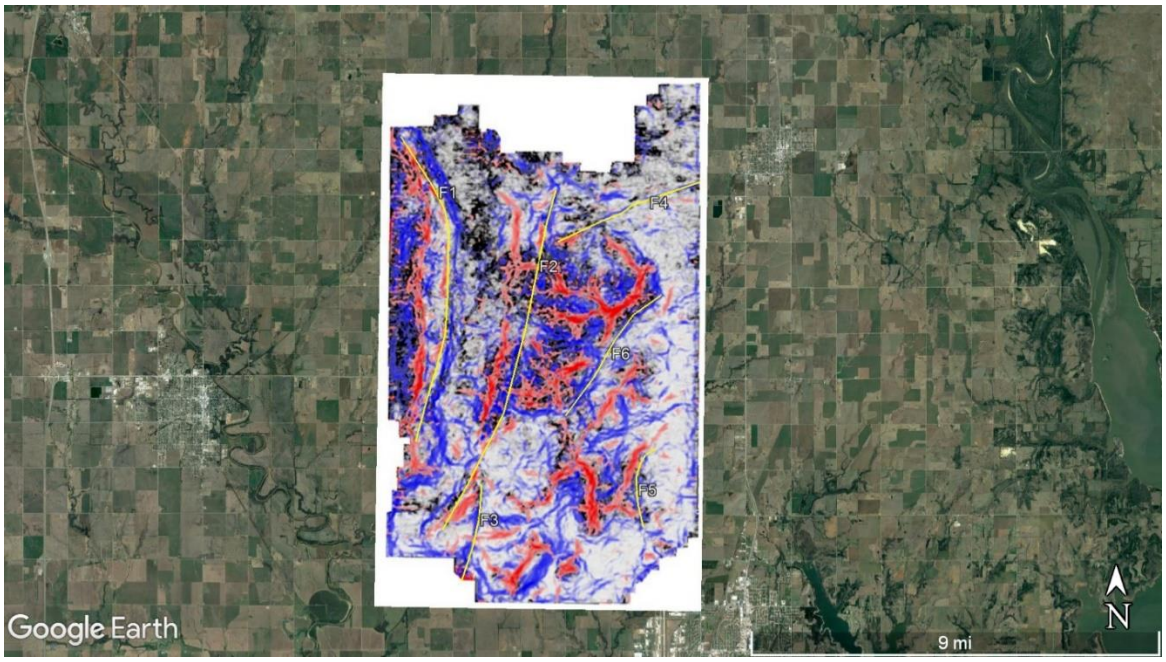

Figure 22: Bois d'Arc top-basement surface with co-rendered energy ratio similarity, most-positive, and most-negative curvature (see color scales in Figure 20). Yellow lines are the faults that were interpreted at the top-basement surface. Each fault has an associated number which was used for cataloging of azimuth, length, and vertical separation data.

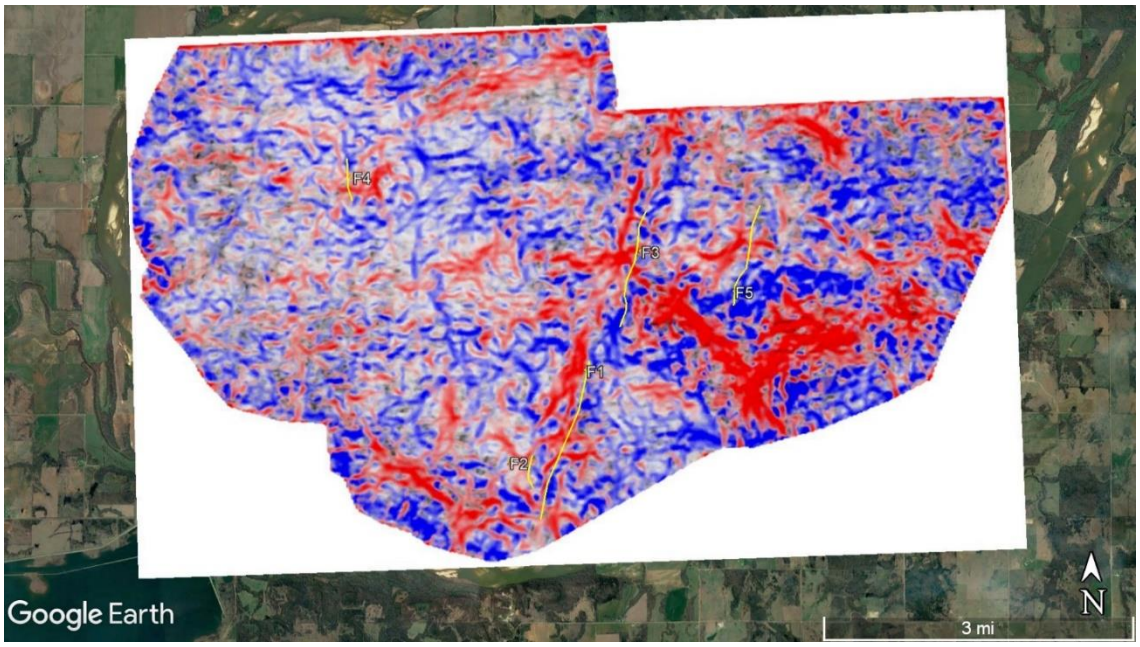

Figure 23: Ceja top-basement surface with co-rendered energy ratio similarity, most-positive, and most-negative curvature (see color scales in Figure 20). Yellow lines are the faults that were interpreted at the top-basement surface. Each fault has an associated number which was used for cataloging of azimuth, length, and vertical separation data.

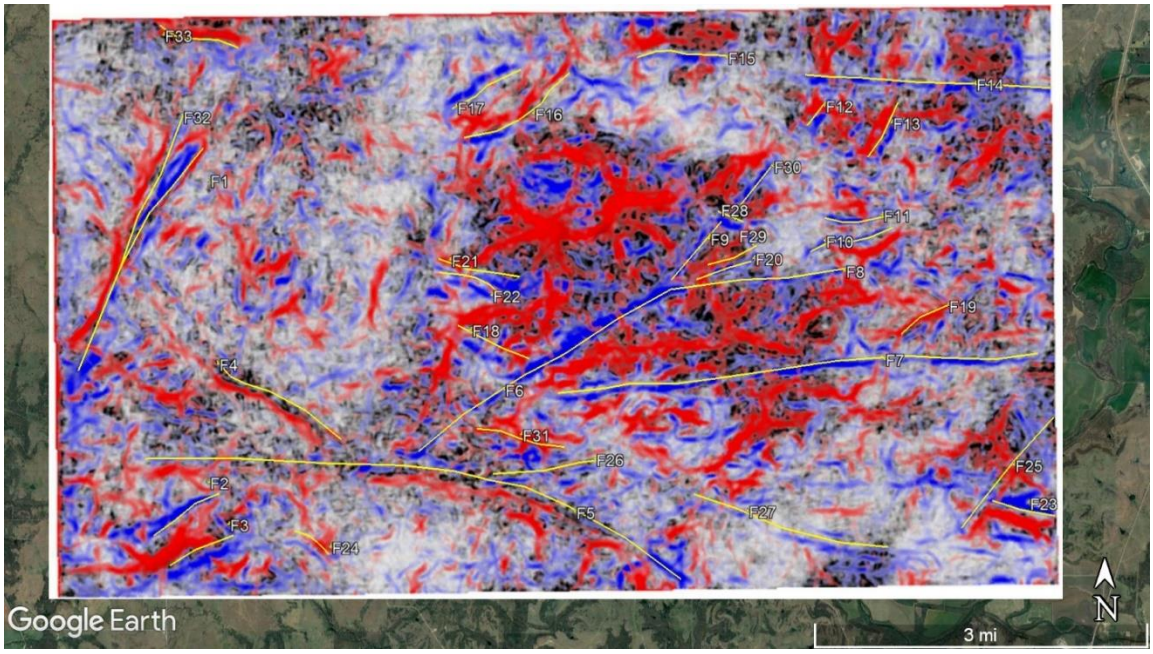

Figure 24: Wild Creek top-basement surface with co-rendered energy ratio similarity, most-positive, and most-negative curvature (see color scales in Figure 20). Yellow lines are the faults that were interpreted at the top-basement surface. Each fault has an associated number which was used for cataloging of azimuth, length, and vertical separation data.

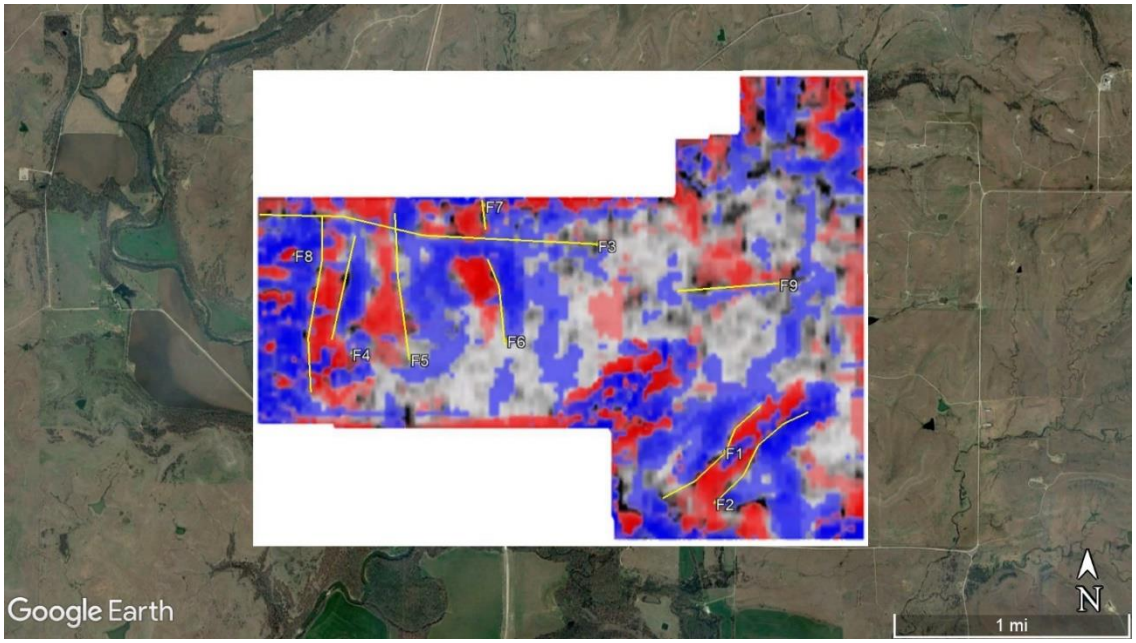

Figure 25: Solomon Creek top-basement surface with co-rendered energy ratio similarity, most-positive, and most-negative curvature (see color scales in Figure 20). Yellow lines are the faults that were interpreted at the top-basement surface. Each fault has an associated number which was used for cataloging of azimuth, length, and vertical separation data.

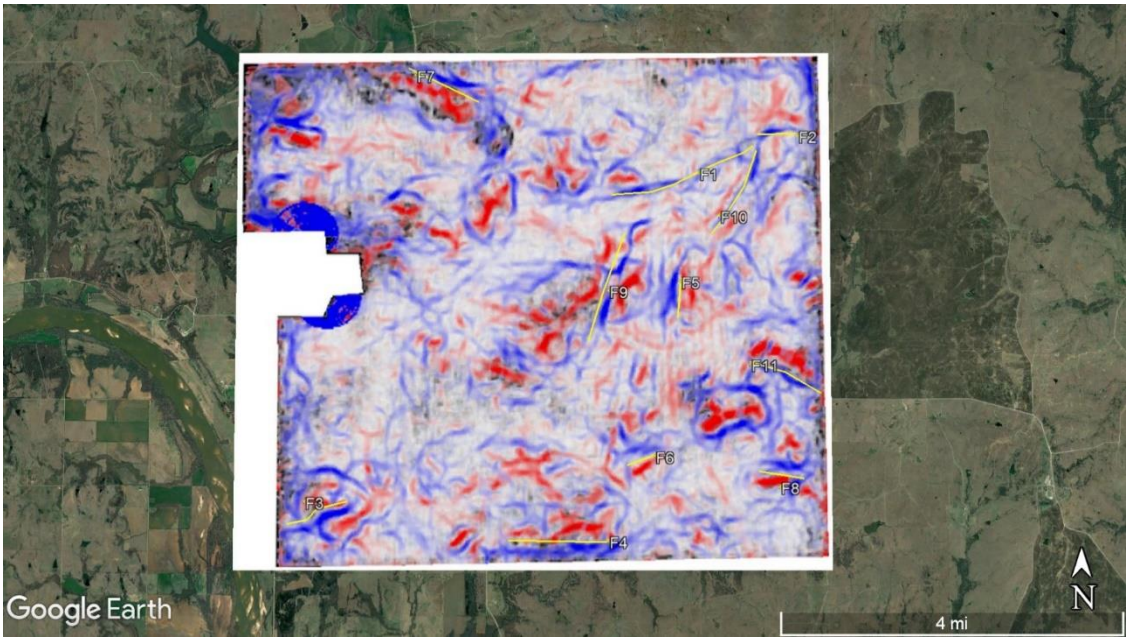

Figure 26: Grey Horse top-basement surface with co-rendered energy ratio similarity, most-positive, and most-negative curvature (see color scales in Figure 20). Yellow lines are the faults that were interpreted at the top-basement surface. Each fault has an associated number which was used for cataloging of azimuth, length, and vertical separation data.

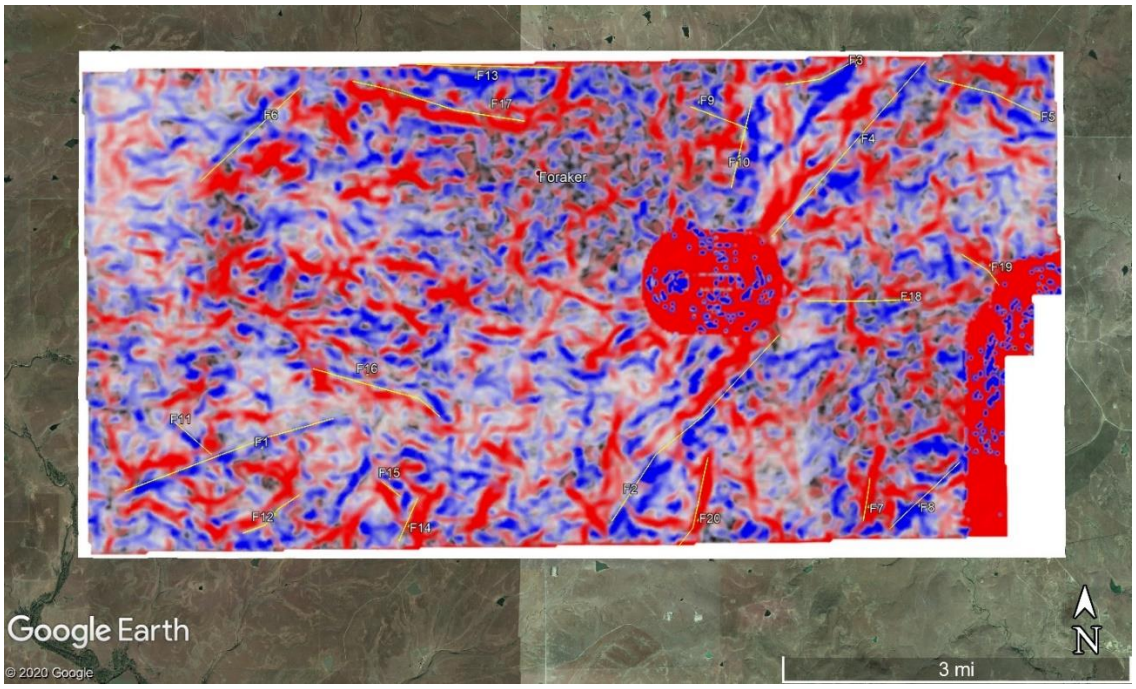

Figure 27: Antelope top-basement surface with co-rendered energy ratio similarity, most-positive, and most-negative curvature (see color scales in Figure 20). Yellow lines are the faults that were interpreted at the top-basement surface. Each fault has an associated number which was used for cataloging of azimuth, length, and vertical separation data.

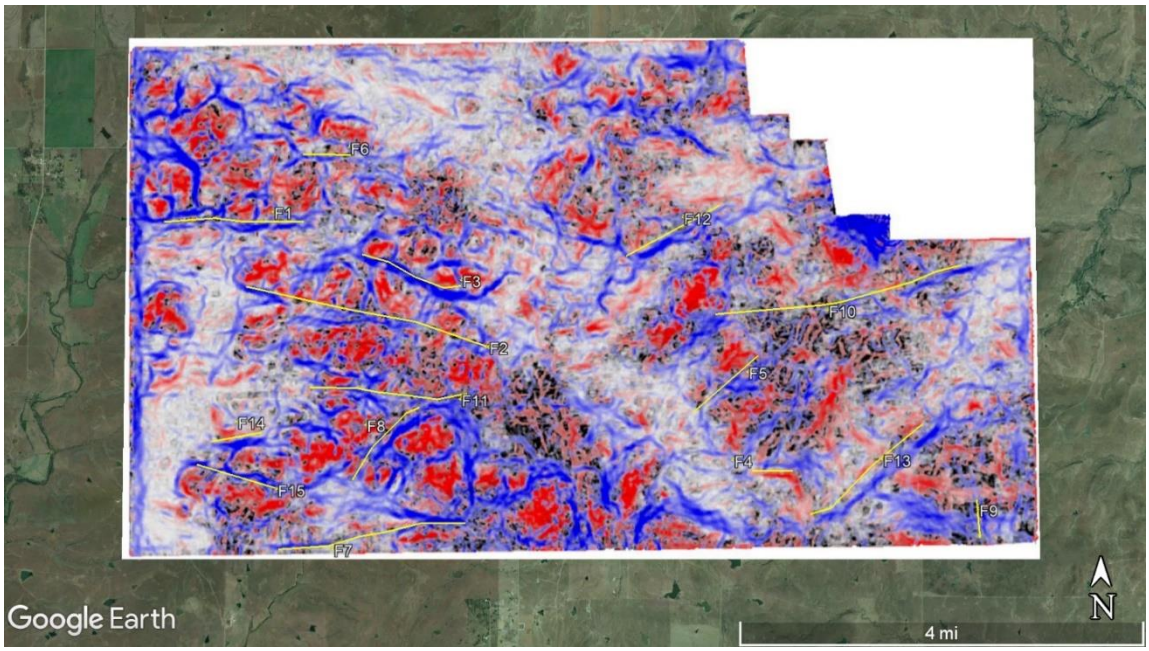

Figure 28: Pearsonia top-basement surface with co-rendered energy ratio similarity, most-positive, and most-negative curvature (see color scales in Figure 20). Yellow lines are the faults that were interpreted at the top-basement surface. Each fault has an associated number which was used for cataloging of azimuth, length, and vertical separation data.

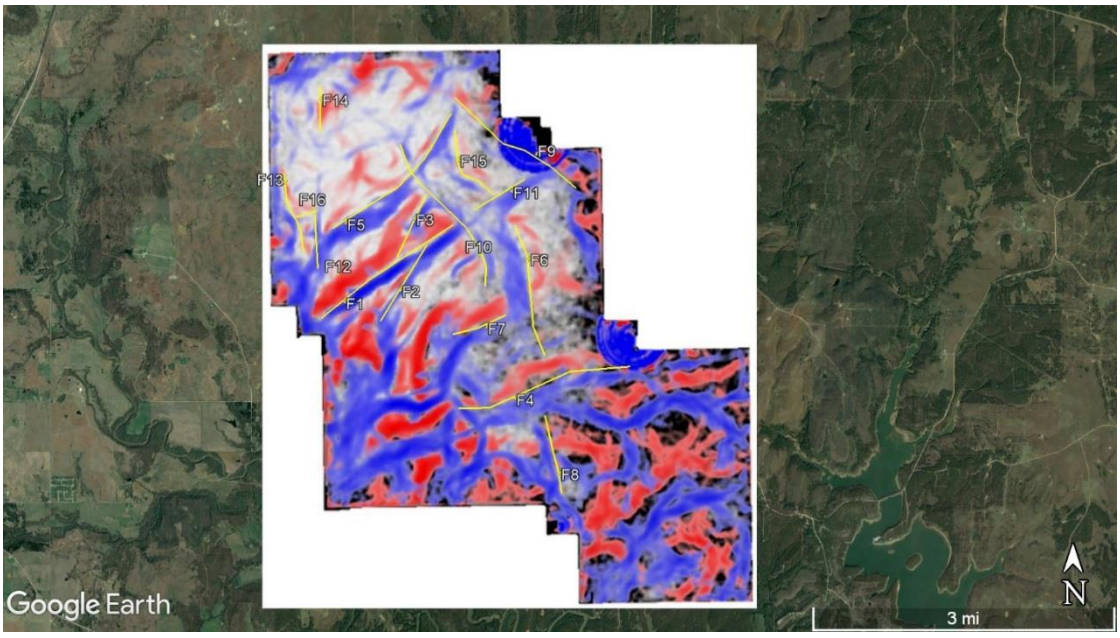

Figure 29: Big Heart top-basement surface with co-rendered energy ratio similarity, most-positive, and most-negative curvature (see color scales in Figure 20). Yellow lines are the faults that were interpreted at the top-basement surface. Each fault has an associated number which was used for cataloging of azimuth, length, and vertical separation data.

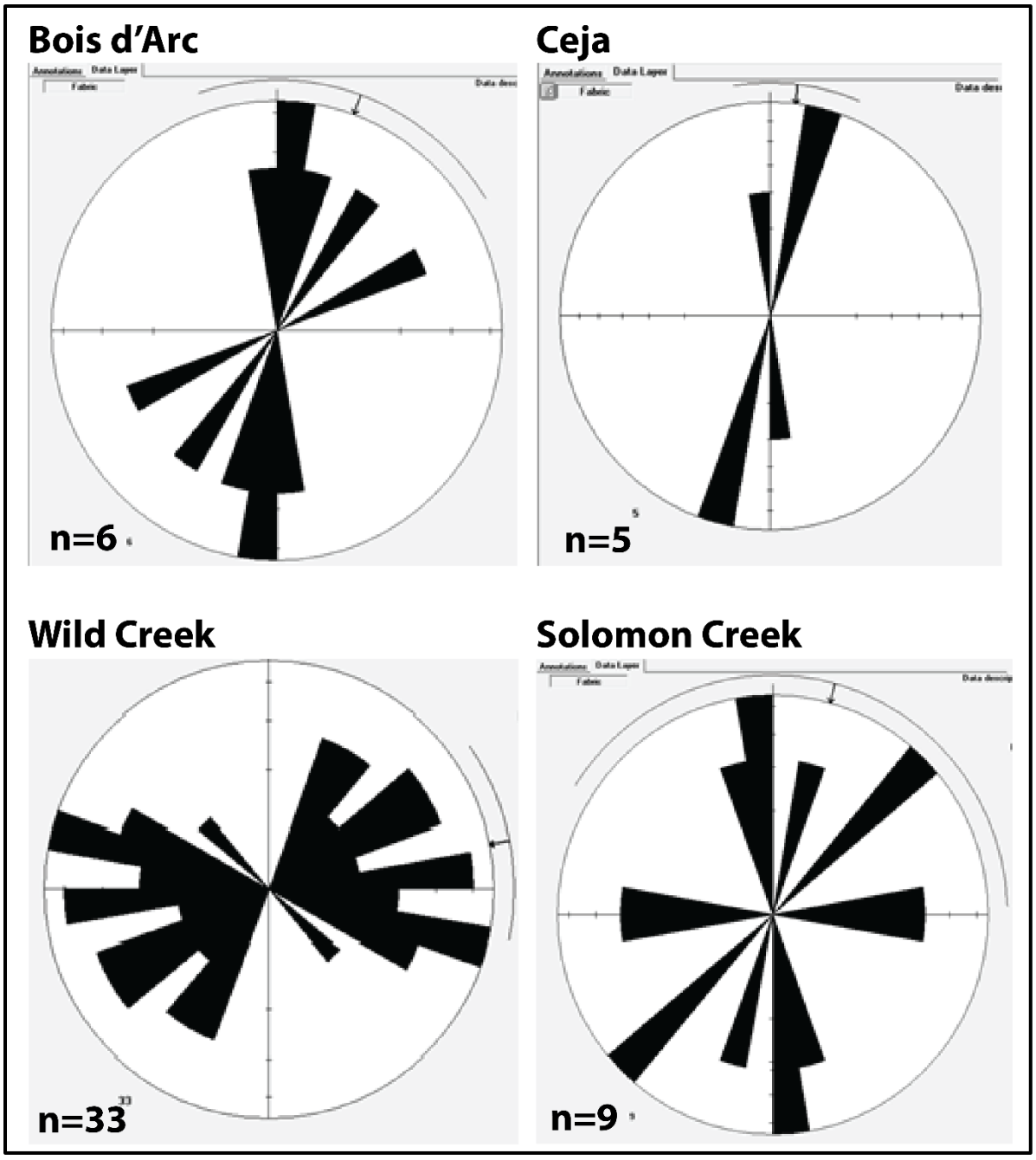

Figure 30: Rose diagrams showing the frequency-azimuth distribution of the faults identified in each survey (Shown in Figures 21-28).

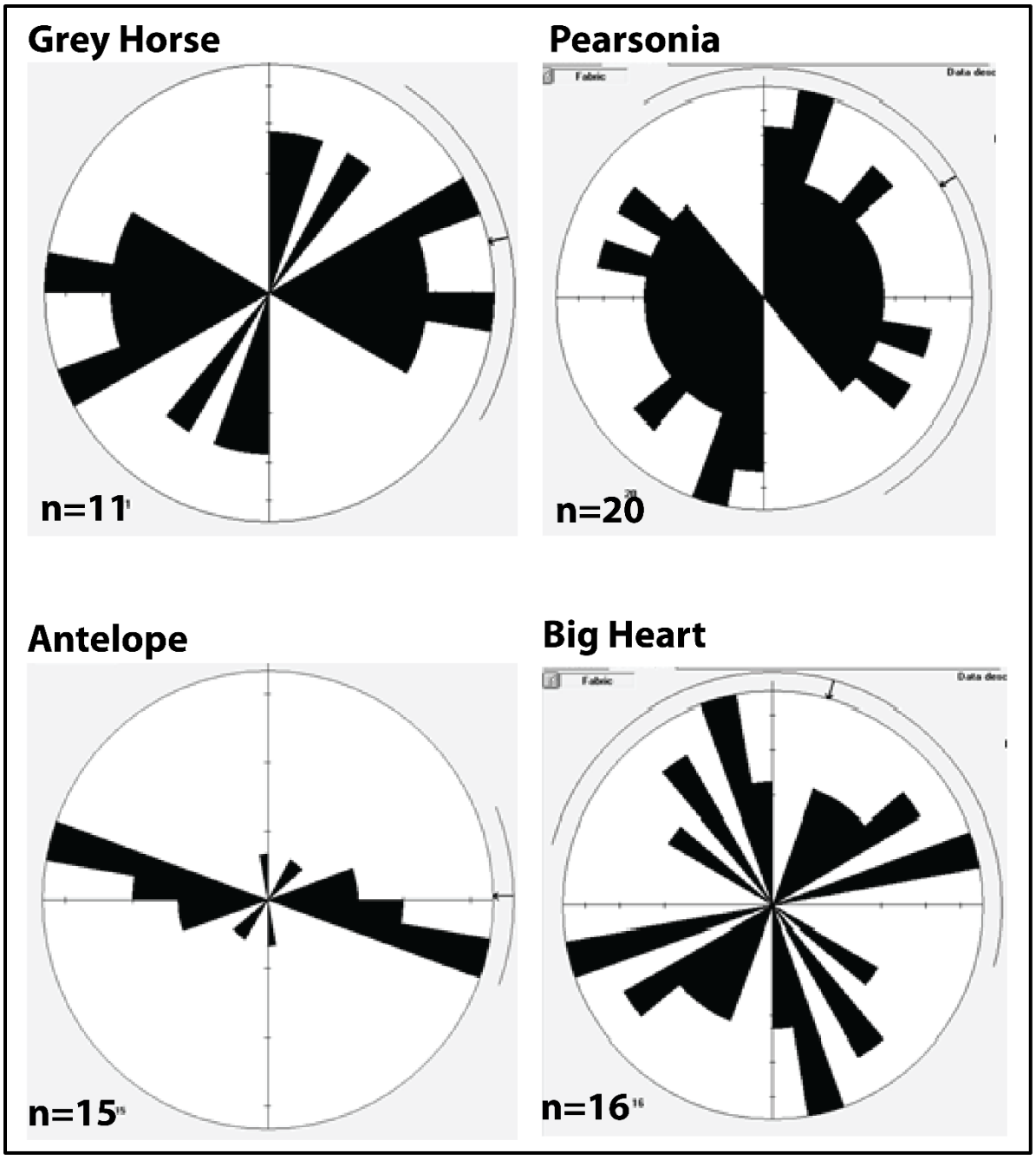

Figure 31: Rose diagrams showing the frequency-azimuth distribution of the faults identified in each survey (Shown in Figures 21-28).

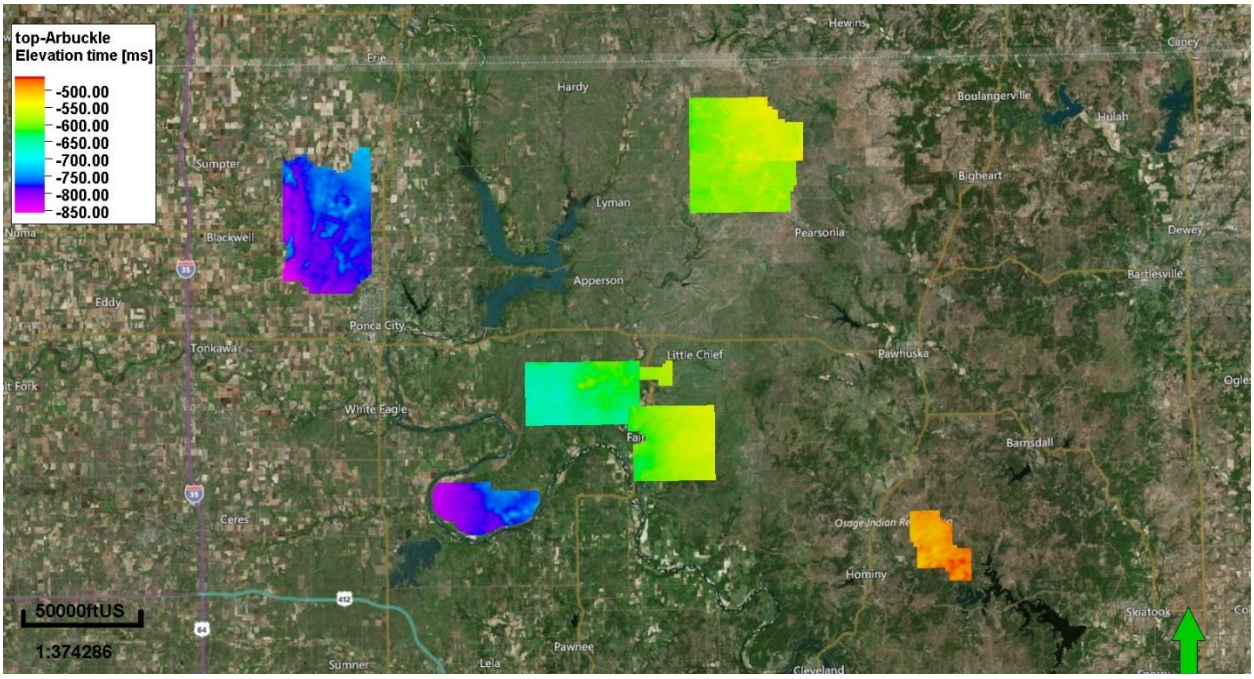

Figure 32: A regional view of the top-Arbuckle TWT interpreted horizons for all 3D seismic surveys. The surfaces share a color bar and color bar limits.

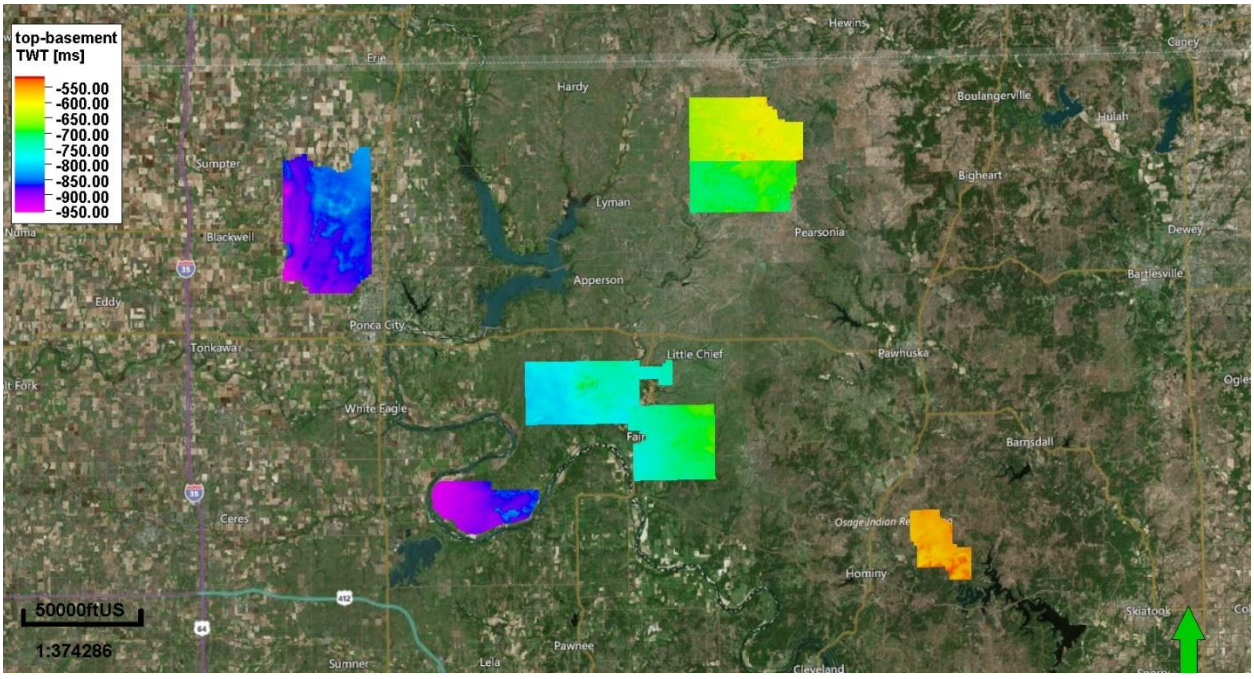

Figure 33: A regional view of the top-basement TWT interpreted horizons for all 3D seismic surveys. The surfaces share a color bar and color bar limits.

Fault Number	Fault Strike (degrees)	Fault Length (km)
F1	358.7	11.345
F2	17.4	12.75
F3	10.5	3.489
F4	69.2	5.503
F5	4.3	3.082
F6	39.5	5.502

Table 2: Fault strike and fault length for the Bois d'Arc seismic survey.

Fault Number	Fault Strike (degrees)	Fault Length (km)
F1	13.5	2.588
F2	1	0.532
F3	11	1.898
F4	353.2	0.676
F5	16.2	1.653

Table 3: Fault strike and fault length for the Ceja seismic survey.

Fault Number	Fault Strike (degrees)	Fault Length (km)
F1	28.8	3.73
F2	58.1	1.146
F3	64.3	1.023
F4	298.7	2.166
F5	95.7	8.165
F6	58	4.373
F7	86.6	7.004
F8	83	2.65
F9	41.6	1.115
F10	79.7	1.273
F11	89.5	0.903
F12	38.5	0.449
F13	27.1	0.895
F14	93.2	3.57
F15	87.4	1.349
F16	66.1	1.856
F17	60.5	1.152
F18	293.8	1.145
F19	56.5	0.795
F20	70.3	0.845
F21	282.8	1.209
F22	290.3	0.938
F23	281.8	0.933
F24	310.8	0.627
F25	39.1	2.081
F26	82	1.523
F27	286	2.934
F28	292.1	0.404
F29	70.5	0.768
F30	38.1	0.925
F31	285.4	1.308
F32	22.5	2.34
F33	285.4	1.21

Table 4: Fault strike and fault length for the Wild Creek seismic survey.

Fault Number	Fault Strike (degrees)	Fault Length (km)
F1	47	0.945
F2	46.3	0.909
F3	93.4	2.338
F4	12.1	0.722
F5	353.5	1
F6	350.2	0.598
F7	352.5	0.205
F8	1	1.211
F9	85.8	0.722

Table 5: Fault strike and fault length for the Solomon Creek seismic survey.

Fault Number	Fault Strike (degrees)	Fault Length (km)
F1	69	2.902
F2	88.5	0.737
F3	72	1.26
F4	271	1.869
F5	7	0.755
F6	67.9	0.552
F7	285.4	1.491
F8	279	0.864
F9	18.2	2.158
F10	30.8	1.841
F11	292	1.476

Table 6: Fault strike and fault length for the Grey Horse seismic survey.

Fault Number	Fault Strike (degrees)	Fault Length (km)
F1	55	2.583
F2	31	1.434
F3	24.5	1.113
F4	80.5	2.871
F5	46.9	2.687
F6	350	2.148
F7	72.7	0.912
F8	347	1.26
F9	308	2.448
F10	328	2.742
F11	60	0.965
F12	356.5	0.863
F13	347	1.323
F14	1	0.719
F15	326.5	1.321
F16	73.1	0.353

Table 7: Fault strike and fault length for the Big Heart seismic survey.

Fault Number	Fault Strike (degrees)	Fault Length (km)
F1	68.5	2.373
F2	40	3.469
F3	73	1.09
F4	40.9	3.242
F5	108.2	1.5
F6	46.9	1.901
F7	6.4	0.598
F8	8.9	1.35
F9	14.4	0.854
F10	13.2	1.195
F11	310.7	0.686
F12	60.1	0.969
F13	91.3	2.048
F14	25	0.649
F15	310	0.337
F16	291	1.907
F17	283	2.455
F18	89.2	1.454
F19	310.5	0.681
F20	11.5	1.317

Table 8: Fault strike and fault length for the Pearsonia seismic survey.

Fault Number	Fault Strike (degrees)	Fault Length (km)
F1	89	2.258
F2	283.9	3.992
F3	289.3	1.706
F4	90.8	0.644
F5	49	1.372
F6	90.7	0.778
F7	83.6	3.033
F8	37.2	1.598
F9	355.6	0.606
F10	77.7	4.063
F11	91.6	2.544
F12	104.5	1.708
F13	100.9	2.361
F14	78.5	0.832
F15	104.8	1.368

Table 9: Fault strike and fault length for the Antelope seismic survey.

Seismic Survey	BdA	Ceja	WC	SC	Grey Horse	Pear.	Ant.	Big Heart
Sedimentary Dominant Frequency (Hz)	54.16	55.35	58.75	61.22	59.21	65.58	50.58	51.78
Sedimentary Velocity (m/s)	5300	5300	5300	5300	5300	5300	5300	5300
Period (s)	0.01846	0.01806	0.01702	0.01633	0.01688	0.01524	0.0197	0.01931
Wavelength (m)	97.8581	95.7542	90.2127	86.5730	89.5119	80.8173	104.784	102.356
Sedimentary Limit of Vertical Resolution (m)	24.4645	23.9385	22.5531	21.6432	22.3779	20.2043	26.1961	25.5890
Basement Dominant Frequency (Hz)	42.38	46.36	53.43	52.23	53.95	51.64	49.35	50.55
Basement Velocity (m/s)	6000	6000	6000	6000	6000	6000	6000	6000
Period (s)	0.02359	0.02157	0.01871	0.01914	0.01853	0.01936	0.02026	0.01978
Wavelength (m)	141.576	129.421	112.296	114.876	111.214	116.189	121.580	118.694
Basement Limit of Vertical Resolution (m)	35.3940	32.3554	28.0741	28.7191	27.8035	29.0472	30.3951	29.6735

Table 10: The table combines resolution limits for all eight 3D seismic surveys. The dominant frequencies shown were calculated first as a volumetric attribute. Then, an interval average was extracted for the deep sedimentary section (approximate Woodford-Hunton reflector to the top-basement horizon) and the basement (top-basement horizon to the end of record length). Once the dominant frequencies were extracted, the limit of resolution was estimated following standard techniques. A constant velocity of 5300 m/s is used for the sedimentary section (after Kolawole et al.,2020) and 6000 m/s for the basement (after Kibikas et al., 2020). We then calculate the period by inverting the dominant frequency and the wavelength by multiplying the period and velocity. Finally, we divide this wavelength by 4 to approximate the limit of vertical resolution for the given interval. BdA=Bois d'Arc; WC=Wild Creek; SC=Solomon Creek; Pear.=Pearsonia; Ant.=Antelope

Seismic Survey	BdA	Ceja	WC	SC	Grey Horse	Pear.	Ant.	Big Heart
Area (km^2)	176.42	65.53	115.46	9	97.54	87.27	103.32	45.31
IL x CL (m)	25.1 x 25.1	16.8 x 33.5	20.1 x 20.1	16.8 x 33.5	33.5 x 33.5	33.5 x 33.5	20.1 x 20.1	33.5 x 33.5
Record Length (s)	2	2	2	2	2	2	2	2
Sample Rate (ms)	2	2	2	2	2	2	2	2
Effective Bandwidth (Hz)	16 – 90	20 – 88	17 – 98	18 – 104	16 – 115	16 – 102	17 – 87	25 – 83

Table 11: The above table provides some common seismic parameters for each survey (area, bin size, record length, sample rate, effective bandwidth). The map view area was calculated for only the live traces of each survey. The bin size, record length, and sample rate were all found in the segy header. The effective bandwidth was estimated using the frequency spectrum for each survey. We chose to measure at -10 dB as this was an amplitude power near which a generally flat spectrum was observed in each survey. BdA=Bois d'Arc; WC=Wild Creek; SC=Solomon Creek; Pear.=Pearsonia; Ant.=Antelope

Seismic Survey	BdA	Ceja	WC	SC	Grey Horse	Pear.	Ant.	Big Heart
λ1 (Distance in m)	36631	44441	47586	13530	35861	21780	47071	25191
λ4 (Distance in m)	933	983	746	983	1244	1244	746	1244
λ3 (Distance in m)	466	491	373	491	622	622	373	622
λ4 (Distance in m)	233	245	186	245	311	311	186	311
r_max operator radius	1650	2200	1320	2200	2200	2200	1320	2200

Table 12: The tables provide the five key parameters (λ1-λ4) and the maximum operator radius that controls the computation of the principal curvature attributes (K1 and K2). BdA=Bois d'Arc; WC=Wild Creek; SC=Solomon Creek; Pear.=Pearsonia; Ant.=Antelope

APPENDIX B

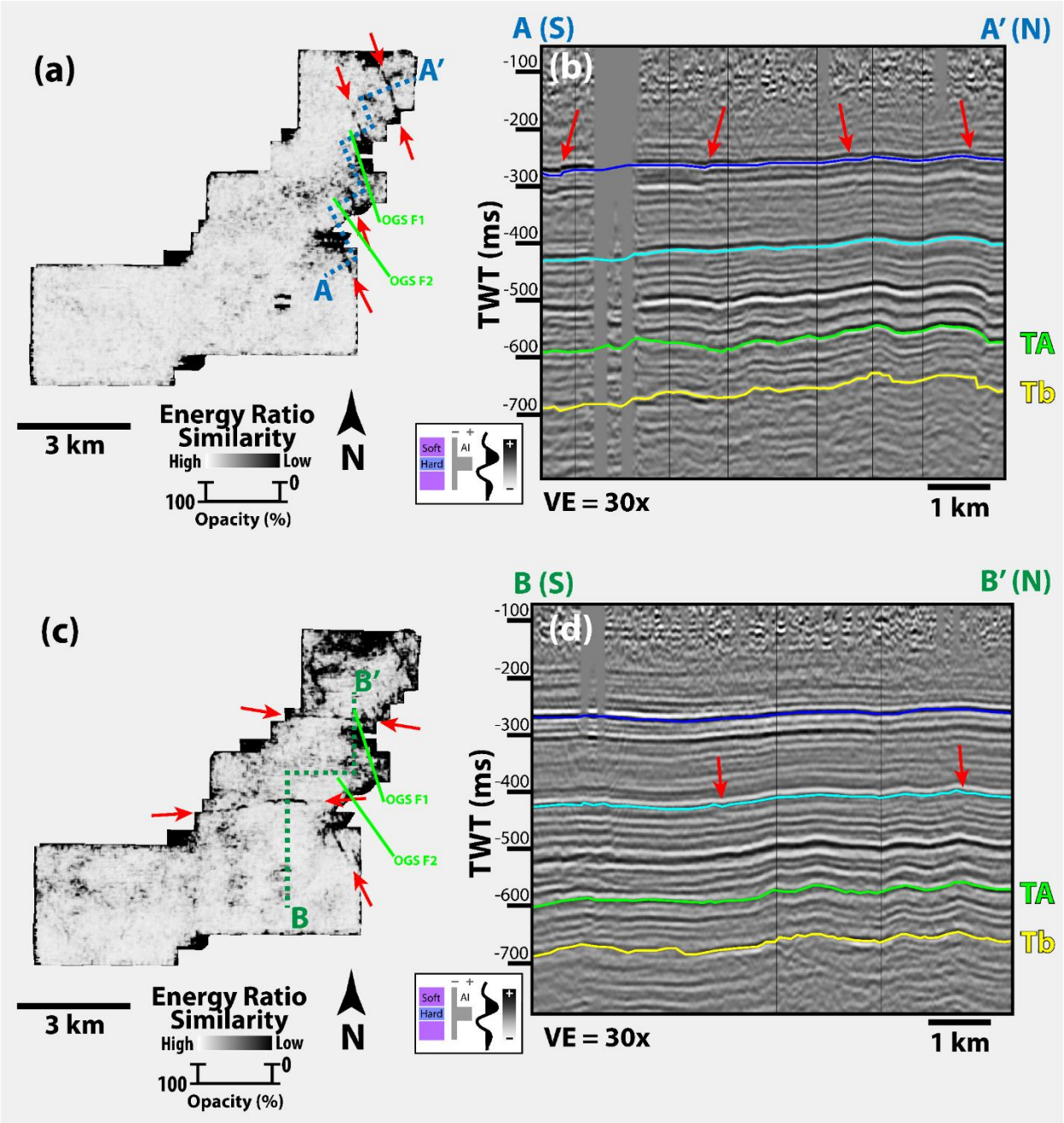

Figure 34: Shallow Faults. (a) Energy ratio similarity extracted at the blue horizon traced in blue on the seismic cross-section to the right. (b) Seismic cross-section through the Harper Creek 3D seismic data, the location of which is shown in panel (a). The black vertical lines represent the position of cross-section azimuth deviation. OGS Faults are shown in light green.

	Interval Dominant Frequency (Hz)	Velocity (m/s)	Period (s)	Wavelength [λ] (m)	Limit of Vertical Resolution [λ/4] (m)
Deep Sediment	54.12	5300	0.018477	97.93	24.48
Crystalline Basement	51.48	6000	0.019425	116.55	29.13

Table 13: An estimation of the limit of vertical resolution for the Harper Creek 3D Seismic Data.

Fault Number	Fault Strike (degrees)	Fault Length (km)
F1	152	1.3526
F2	102	1.0786
F3	149	1.0890
F4	102	0.8851
F5	102	1.2733
F6	57	3.0308
F7	99	3.8396
F8	151	1.4930
F9	63	3.6130
F10	127	1.3548
F11	28	5.6056
F12	132	0.5626
F13	135	0.7630
F14	69	1.5265
F15	42	0.7930
F16	128	1.1517
F17	137	2.4469
F18	123	0.9114
F19	40	2.2131
F20	61	0.9031
F21	23	8.8188
F22	49	1.8257
F23	45	1.2441
F24	59	1.3432
F25	6	2.3280
F26	66	0.8696
F27	90	1.6890
F28	75	1.3494
F29	70	2.0816
F30	70	1.6231
F31	15	2.0854

Table 14: Fault strike in degrees and fault length in kilometers of all faults identified at the top of the basement within the Harper Creek survey.

REFERENCES CITED

Anderson, J. Lawford, 1983, Proterozoic Anorogenic Granite Plutonism of North America. Geological Society of America Memoirs Proterozoic Geology: Selected Papers from an International Proterozoic Symposium, 133–54, doi: 10.1130/mem161-p133.

Bahorich, Mike, and Steve Farmer, 1995, 3-D Seismic Discontinuity for Faults and Stratigraphic Features: The Coherence Cube. The Leading Edge, **14**, no. 10, 1053–58. doi: 10.1190/1.1437077.

Barbour, Andrew J., Jack H. Norbeck, and Justin L. Rubinstein, 2017, The Effects of Varying Injection Rates in Osage County, Oklahoma, on the 2016Mw 5.8 Pawnee Earthquake. Seismological Research Letters **88**, no. 4, 1040–53, doi: 10.1785/0220170003.

Bickford, M. E., K. L. Harrower, W. J. Hoppe, B. K. Nelson, R. L. Nusbaum, and John J. Thomas, 1981, Rb-Sr and U-Pb Geochronology and Distribution of Rock Types in the Precambrian Basement of Missouri and Kansas. Geological Society of America Bulletin, **92**, no. 6, 323, doi: 10.1130/0016-7606(1981)92<323:raugad>2.0.co;2.

Bickford, M.e., W.r. Van Schmus, K.e. Karlstrom, P.a. Mueller, and G.d. Kamenov, 2015, Mesoproterozoic-Trans-Laurentian Magmatism: A Synthesis of Continent-Wide Age Distributions, New SIMS U–Pb Ages, Zircon Saturation Temperatures, and Hf and Nd Isotopic Compositions. Precambrian Research, **265**, 286–312, doi: 10.1016/j.precamres.2014.11.024.

Burke, Kevin, and J. F. Dewey, 1973, Plume-Generated Triple Junctions: Key Indicators in Applying Plate Tectonics to Old Rocks. The Journal of Geology, **81**, no. 4, 406–33, https://doi.org/10.1086/627882.

Cartwright, Joseph, and Dorthe Møller Hansen, 2006, Magma Transport through the Crust via Interconnected Sill Complexes. Geology, **34**, no. 11, 929, doi: 10.1130/g22758a.1.

Carroll, Herbert B., K.c. Chen, Genliang Guo, W.i. Johnson, T.k. Reeves, and Bijon Sharma. 1999. Exploration 3-D Seismic Field Test/Native Tribes Initiative, 1–64, doi: 10.2172/6056.

Chang, K. W., and P. Segall, 2016, Injection-Induced Seismicity on Basement Faults Including Poroelastic Stressing. Journal of Geophysical Research, Solid Earth, **121**, no. 4, 2708–26, doi: 10.1002/2015jb012561.

Chen, Chen, 2016, Comprehensive Analysis of Oklahoma Earthquakes: from Earthquake Monitoring to 3D Tomography and Relocation

Chopra, Satinder J., Lennon J. Infante-Paez, and Kurt J. Marfurt, 2018, Intra-Basement Intrusions in the STACK Area of Oklahoma. Search and Discovery 42229, http://mcee.ou.edu/aaspi/publications/2018/Chopra_et_al_2018-Intra-basement_intrusions_in_the_STACK_area_of_Oklahoma.pdf, accessed April 2019

Chopra, Satinder, and Kurt J. Marfurt, 2007, 4. Volumetric Curvature and Reflector Shape. Seismic Attributes for Prospect Identification and Reservoir Characterization, 73–98, doi: 10.1190/1.9781560801900.ch4.

Crain, K. D., & Chang, J. C., 2018, January. Elevation Map of the Top of the Crystalline Basement in Oklahoma and Surrounding States. Retrieved from http://ogs.ou.edu/docs/openfile/OF1-2018.pdf.

Crone, Anthony J., and Kenneth V. Luza, 1990, Style and Timing of Holocene Surface Faulting on the Meers Fault, Southwestern Oklahoma. Geological Society of America Bulletin **102**, no. 1, 1–17, doi: 10.1130/0016-7606(1990)102<0001:satohs>2.3.co;2.

Denison, R. E., 1966, Basement Rocks in Adjoining Parts of Oklahoma, Kansas, Missouri, and Arkansas: Ph.D. dissertation, University of Texas

Denison, R. E., 1981, Basement Rocks in Northeastern Oklahoma, Oklahoma Geological Survey, 84, http://www.ogs.ou.edu/pubsscanned/Circulars/circular84mm.pdf, accessed November 2019.

Earthquake Top Ten and Yearly Summaries, 2018, https://www.ou.edu/ogs/research/earthquakes/Information, accessed August 2019.

Elebiju, Olubunmi O., Shane Matson, G. Randy Keller, and Kurt J. Marfurt, 2011, Integrated Geophysical Studies of the Basement Structures, the Mississippi Chert, and the Arbuckle Group of Osage County Region, Oklahoma, AAPG Bulletin, **95**, no. 3, 371–93, doi: 10.1306/08241009154.

Ellsworth, W. L., 2013, Injection-Induced Earthquakes, Science, **341**, 122592, doi: 10.1126/science.1225942.

Elmore, R. Douglas, Patrick K. Sutherland, and Perry B. White, 1990, Middle Pennsylvanian Recurrent Uplift of the Ouachita Fold Belt and Basin Subsidence in the Arkoma Basin, Oklahoma, Geology, **18**, no. 9, 906, doi: 10.1130/0091-7613(1990)018<0906:mpruot>2.3.co;2.

Emslie, R. F. (1980). Geology and petrology of the Harp Lake complex, central Labrador, an example of elsonian magmatism. Geological Survey of Canada Bulletin, 293. doi:10.4095/102158

Firkins, Max, Folarin Kolawole, Kurt J. Marfurt, and Brett M. Carpenter, 2020, Attribute-Assisted Characterization of Basement Faulting and the Associated Sedimentary Sequence Deformation in North-Central Oklahoma. Interpretation **8**, no. 4, https://doi.org/10.1190/int-2020-0053.1.

Frost, C. D., Frost, B. R., Chamberlain, K. R., & Edwards, B. R. (1999). Petrogenesis of the 1.43 Ga Sherman Batholith, SE Wyoming, USA: a Reduced, Rapakivi-type Anorogenic Granite. Journal of Petrology, 40(12), 1771–1802. doi: 10.1093/petroj/40.12.1771

Gay, S., 2003, The Nemaha Trend-A System of Compressional Thrust-Fold, Strike-Slip Structural Features in Kansas and Oklahoma, Part 1. Shale Shaker **51**, 9–17, doi: 10.1306/e4fd318f-1732-11d7-8645000102c1865d.

Guo, Genliang, and S.a. And George, 1999, An Analysis of Surface and Subsurface Lineaments and Fractures for Oil and Gas Exploration in the Mid-Continent Region. Fossil Disclaimer, 1–48, doi: 10.2172/5611.

Hamilton, M., B. Carpenter, C. Johnston, F. Kolawole, S. Evans, and R.D. Elmore, 2021, Fractured, Altered, and Faulted Basement in Northeastern Oklahoma: Implications for Induced Seismicity, Journal of Structural Geology **147**, https://doi.org/10.1016/j.jsg.2021.104330.

Hatcher, R. D., Jr., 2010, The Appalachian orogen: A brief summary in Tollo, R. P., Batholomew, M.j., Hibbard, J. P., and Karabinos, PM., eds. From Rodinia to Pangea: The lithotectonic Record of the Appalachian Region: Geological Society of America Memoir, **206**, 1-19, doi: 10.1130/2010.1206(01).

Hinze, W. J., David J. Allen, Lawrence W. Braile, and John Mariano, 1997, The Midcontinent Rift System: A Major Proterozoic Continental Rift. Middle Proterozoic to Cambrian rifting, central North America, https://doi.org/10.1130/0-8137-2312-4.7.

Holland, A. A., 2013, Optimal Fault Orientations within Oklahoma., Seismological Research Letters 84, no. **5**, 876–90. https://doi.org/10.1785/0220120153.

Hussein, Marwa, Robert R. Stewart, and Jonny Wu. "Which Seismic Attributes Are Best for Subtle Fault Detection?" Interpretation 9, no. 2 (2021). https://doi.org/10.1190/int-2020-0068.1.

Ireland, H.A., 1955. Pre-Cambrian surface in northeastern Oklahoma and parts of adjacent states. AAPG (Am. Assoc. Pet. Geol.) Bull. **39** (4), 468–483. https://doi.org/ 10.1306/5CEAE163-16BB-11D7-8645000102C1865D.

Jacobs, T., 2016, Seismic shifts in Oklahoma lead to stricter regulations: Journal of Petroleum Technology, **68**, 44-48, doi: 10.2118/0516-0044-JPT

Johnson, K., 2008, Geologic history of Oklahoma: Educational Publication, **9**, 3–8.

Keller, G. Randy, and Randell A. Stephenson, 2007, The Southern Oklahoma and Dniepr-Donets Aulacogens: A Comparative Analysis: Geological Society of America Memoirs 4-D Framework of Continental Crust, 127–43, doi: 10.1130/2007.1200(08).

Keranen, K. M., M. Weingarten, G. A. Abers, B. A. Bekins, and S. Ge, 2014, Sharp Increase in Central Oklahoma Seismicity since 2008 Induced by Massive Wastewater Injection: Science **345**, 6195, 448–51, doi: 10.1126/science.1255802.

Kibikas, William M., Brett M. Carpenter, and Ahmad Ghassemi., 2020, Mechanical Strength and Physical Properties of Oklahoma's Igneous Basement., Tectonophysics 777, https://doi.org/10.1016/j.tecto.2020.228336.

Kluth, C. F., 1986, Plate Tectonics of the Ancestral Rocky Mountains: American Association of Petroleum Geologists Memoir, **41**, doi: 10.1306/m41456c17.

Kolawole, F., C. S. Johnston, C. B. Morgan, J. C. Chang, K. J. Marfurt, D. A. Lockner, Z. Reches, and B. M. Carpenter, 2019, The Susceptibility of Oklahoma's Basement to Seismic Reactivation: Nature Geoscience, **12**, no. 10, 839–844, doi: 10.1038/s41561-019-0440-5.

Kolawole, F., M. Simpson Turko, and B.M. Carpenter, 2020, Basement-Controlled Deformation of Sedimentary Sequences, Anadarko Shelf, Oklahoma: Basin Research, doi: 10.1111/bre.12433.

Kroll, Kayla A., Elizabeth S. Cochran, and Kyle E. Murray, 2107, Poroelastic Properties of the Arbuckle Group in Oklahoma Derived from Well Fluid Level Response to the 3 September

2016Mw 5.8 Pawnee and 7 November 2016 Mw 5.0 Cushing Earthquakes: Seismological Research Letters, **88**, no. 4, 963–70, doi: 10.1785/0220160228.

Lidiak, Edward G., 1996, Geochemistry of Subsurface Proterozoic Rocks in the Eastern Midcontinent of the United States: Further Evidence for a within-Plate Tectonic Setting: Basement and Basins of Eastern North America, **308**, 45–66, doi: 10.1130/0-8137-2308-6.45.

Liner, Kevin Matthew, 2015, An Investigation of 3D Seismic Deep Basement Events in Osage County, Oklahoma: M.S. thesis, University of Arkansas.

Luza, K.V., and Lawson, J.E. Jr. Tue, 1983, Seismicity and tectonic relationships of the Nemaha Uplift in Oklahoma. Part V. Final report: Technical Report, NUREG/CR-3109 ON: DE83901537, https://www.osti.gov/biblio/6372925-seismicity-tectonic-relationships-nemaha-uplift-oklahoma-part-final-report, accessed August 2019

Magee, Craig, James D. Muirhead, Alex Karvelas, Simon P. Holford, Christopher A.l. Jackson, Ian D. Bastow, Nick Schofield, et al., 2016, Lateral Magma Flow in Mafic Sill Complexes: Geosphere, **12**, no. 3, 809–841, doi: 10.1130/ges01256.1.

Mai, Ha T., Olubunmi O. Elebiju, and Kurt J. Marfurt, 2014, Attribute Illumination of Basement Faults, Examples from Cuu Long Basin Basement, Vietnam and the Midcontinent, USA: Interpretation, **2**, no. 1, doi: 10.1190/int-2013-0091.1.

Marsh, S., and A. Holland, 2016, Comprehensive Fault Database and Interpretive Fault Map of Oklahoma, Oklahoma Geological Survey Open-File Report 2. https://www.ou.edu/ogs/data/fault.

McBee, W., 2003, The Nemaha and Other Strike-Slip Faults in the Midcontinent U.S.A.: Midcontinent Section Meeting (Tulsa), http://archives.datapages.com/data/tgs/tgs-sp/data/051/051001/59_tgs-sp0510059.htm, accessed March 2019

OGS, Earthquake Top Ten and Yearly Summaries. 2020. Retrieved from https://www.ou.edu/ogs/research/earthquakes/Information.

Patel, Swetal, Folarin Kolawole, Jacob I. Walter, Xiaowei Chen, and Kurt J. Marfurt, 2021, Seismic Illumination of Small-Throw Seismogenic Faults, Anadarko Basin, Oklahoma. Interpretation **9**, no. 2, https://doi.org/10.1190/int-2020-0135.1.

Perry, William J., 1989, Tectonic Evolution of the Anadarko Basin Region, Oklahoma, U.S. Geological Survey Bulletin, 1866-A, https://doi.org/10.3133/b1866a.

Sahar, Mohammadi, Jay M. Gregg, Kevin L. Shelton, Martin S. Appold, and James O. Puckette, 2019, Influence of Late Diagenetic Fluids on Mississippian Carbonate Rocks on the Cherokee–Ozark Platform, Northeast Oklahoma, Northwest Arkansas, Southwest Missouri, and Southeast Kansas: Mississippian Reservoirs of the Midcontinent, 323–52, doi: 10.1306/13632154m1163791.

Moores, E. M., 1991, Southwest U.S.-East Antarctic (SWEAT) Connection: A Hypothesis: Geology **19**, no. 5, 425, doi: 10.1130/0091-7613(1991)019<0425:suseas>2.3.co;2.

Nelson, R., T. Patton, and C. Morley, 1992, Rift-Segment Interaction and Its Relation to Hydrocarbon Exploration in Continental Rift Systems: AAPG Bulletin, **76**, doi: 10.1306/bdff898e-1718-11d7-8645000102c1865d.

Northcutt, R. A., and J. A. Campbell, 1995, Geologic Provinces of Oklahoma: Oklahoma Geological Survey Open File Report 5. http://ogs.ou.edu/docs/openfile/OF5-95.pdf, accessed March 2019

Pollyea, Ryan M., Martin C. Chapman, Richard S. Jayne, and Hao Wu, 2019, High Density Oilfield Wastewater Disposal Causes Deeper, Stronger, and More Persistent Earthquakes: Nature Communications, **10**, no. 1, doi: 10.1038/s41467-019-11029-8.

Qi, X. and K. J. Marfurt, 2018, Volumetric aberrancy to map subtle faults and flexures: Interpretation, 6(2), T349-T365. https://doi.org/10.1190/INT-2017-0114.1

Qin, Yan, Xiaowei Chen, Jacob I. Walter, Jackson Haffener, Daniel T. Trugman, Brett M. Carpenter, Matthew Weingarten, and Folarin Kolawole, 2019, Deciphering the Stress State of Seismogenic Faults in Oklahoma and Southern Kansas Based on an Improved Stress Map: Journal of Geophysical Research: Solid Earth, **124**, no. 12, 12920–12934, doi: 10.1029/2019jb018377.

Rivers, T., & Corrigan, D., 2000, Convergent margin on southeastern Laurentia during the Mesoproterozoic: tectonic implications. Canadian Journal of Earth Sciences, **37**(2-3), 359–383. doi: 10.1139/e99-067

Schoenball, Martin, and William L. Ellsworth, 2017, Waveform-Relocated Earthquake Catalog for Oklahoma and Southern Kansas Illuminates the Regional Fault Network., Seismological Research Letters **88**, no. 5, 1252–58. https://doi.org/10.1785/0220170083.

Schwab, Drew R., Tandis S. Bidgoli, and Michael H. Taylor, 2017, Characterizing the Potential for Injection-Induced Fault Reactivation Through Subsurface Structural Mapping and

Stress Field Analysis, Wellington Field, Sumner County, Kansas: Journal of Geophysical Research: Solid Earth, **122**, no. 12, 10132 – 10154, doi:10.1002/2017jb014071.

Sears, J. W., George, G. M. S., & Winne, J. C. (2005). Continental rift systems and anorogenic magmatism. Lithos, 80(1-4), 147–154. doi: 10.1016/j.lithos.2004.05.009

Segall, P., and S. Lu, 2015, "Injection-Induced Seismicity: Poroelastic and Earthquake Nucleation Effects: Journal of Geophysical Research: Solid Earth, **120**, no. 7, 5082–5103, doi: 10.1002/2015jb012060.

Shah, Anjana K., and G. Randy Keller, 2017, Geologic Influence on Induced Seismicity: Constraints from Potential Field Data in Oklahoma: Geophysical Research Letters, **44**, no. 1: 152–161, doi: 10.1002/2016gl071808.

Slagstad, T., N. G. Culshaw, J. S. Daly, and R. A. Jamieson, 2009, Western Grenville Province Holds Key to Midcontinental Granite-Rhyolite Province Enigma: Terra Nova, **21**, no. 3, 181–187, doi: 10.1111/j.1365-3121.2009.00871.x.

SLU. Moment tensor solutions, June 1, 2021. http://www.eas.slu.edu/eqc/eqc_mt/MECH.NA/MECHFIG/mech.html.

Stein, Carol A., Seth Stein, Miguel Merino, G. Randy Keller, Lucy M. Flesch, and Donna M. Jurdy, 2014, Was the Midcontinent Rift Part of a Successful Seafloor-Spreading Episode?: Geophysical Research Letters, **41**, no. 5, 1465–1470, doi: 10.1002/2013gl059176.

Thomas, J. J., R. D. Shuster, and M. E. Bickford, 1984, A Terrane of 1,350- to 1,400-M.y.-Old Silicic Volcanic and Plutonic Rocks in the Buried Proterozoic of the Mid-Continent and in the

Wet Mountains, Colorado: Geological Society of America Bulletin, **95**, no. 10, 1150, doi: 10.1130/0016-7606(1984)95<1150:atotms>2.0.co;2.

Waldhauser, F. "A Double-Difference Earthquake Location Algorithm: Method and Application to the Northern Hayward Fault, California." Bulletin of the Seismological Society of America 90, no. 6 (2000): 1353–68. https://doi.org/10.1785/0120000006.

Walsh, F. Rall, and Mark D. Zoback, 2016, Probabilistic Assessment of Potential Fault Slip Related to Injection-Induced Earthquakes: Application to North-Central Oklahoma, USA: Geology, **44**, no. 12, 991–994, https://doi.org/10.1130/g38275.1.

Van Schmus, W.R., Bickford, M.E., Sims, P.K., Anderson, R.R., Shearer, C.K., Treves, S.B., 1993. Proterozoic geology of the western midcontinent basement. In: Reed, J.C., Jr, et al. (Eds.), Precambrian: Conterminous US Boulder, Colorado, Geological Society of America, vols. C-2. Geology of North America, pp. 239/259.

Yeck, W. L., G. P. Hayes, D. E. Mcnamara, J. L. Rubinstein, W. D. Barnhart, P. S. Earle, and H. M. Benz, 2017, Oklahoma Experiences Largest Earthquake during Ongoing Regional Wastewater Injection Hazard Mitigation Efforts: Geophysical Research Letters, **44**, no. 2, 711–717, https://doi.org/10.1002/2016gl071685.

Zhai, Guang, Manoochehr Shirzaei, Michael Manga, and Xiaowei Chen, 2019, Pore-Pressure Diffusion, Enhanced by Poroelastic Stresses, Controls Induced Seismicity in Oklahoma: Proceedings of the National Academy of Sciences, **116**, no. 33, 16228–16233, doi: 10.1073/pnas.1819225116.